Exploring Quantum Field Theories using Qubit Lattice Models

by

Hershdeep Singh

Department of Physics
Duke University

Approved:

Roxanne Springer, Advisor

Shailesh Chandrasekharan, Co-advisor

Ayana Arce

Harold Baranger

Phillip Barbeau

Dissertation submitted in partial fulfillment of the
requirements for the degree of Doctor of Philosophy
in the Department of Physics
in the Graduate School of
Duke University

2020

Abstract

Exploring Quantum Field Theories using Qubit Lattice Models

by

Hershdeep Singh

Department of Physics
Duke University

Approved:

Roxanne Springer, Advisor

Shailesh Chandrasekharan, Co-advisor

Ayana Arce

Harold Baranger

Phillip Barbeau

An abstract of a dissertation submitted in partial fulfillment of the requirements for the degree of Doctor of Philosophy in the Department of Physics in the Graduate School of Duke University

2020

Abstract

The framework of quantum field theory (QFT) underlies our modern understanding of both particle physics and condensed matter physics. Despite its importance, precise quantitative calculations in strongly-coupled theories in QFTs have generally only been possible through non-perturbative lattice Monte Carlo (MC) methods. Traditionally, such lattice MC methods proceed by starting from a lattice regularization of the continuum QFT of interest, which has the same (possibly infinite dimensional) local Hilbert space at each lattice site as the continuum QFT. In this thesis, we explore an alternative regularization where the local Hilbert space is also replaced by a smaller finite dimensional Hilbert space. Motivated by the appeal of such models for near-term quantum computers, we dub this approach *qubit regularization*. Using this approach, in this thesis, we present three main results. First, we develop a qubit-regularization for the $O(N)$ nonlinear sigma model (NLSM) in $D \geq 3$ spacetime dimensions. We show using numerical lattice calculations that the $O(N)$ qubit model lies in the correct universality class for $N = 2, 4, 6, 8$, and reproduces the universal physics of the $O(N)$ Wilson-Fisher (WF) fixed point in $D = 3$ spacetime dimensions by computing some well-known critical exponents. Next, we explore sectors of large global charges of the $O(N)$ WF conformal field theory (CFT) using the $O(N)$ qubit model. This allows us to test the predictions of a recently proposed large-charge effective field theory (EFT) and extract the two leading low-energy constants (LECs) in the EFT. Performing computations for $N = 2, 4, 6, 8$, we are also able to quantitatively test predictions of a recent large-N analysis in the large-charge sectors. Finally, we show that our qubit approach can also be used to study the few-body physics of non-relativistic particles. In particular, we consider a system of two species of mass-imbalanced fermions in $1 + 1$ dimensions. We compute the ground state energies for a range of mass-imbalances and interaction strengths, and uncover

some problems with recent results obtained from the Complex Langevin (CL) method for the same system.

Dedicated to my father.

Contents

List of Tables

List of Figures

List of Abbreviations

AFQMC	auxiliary field quantum Monte Carlo
CFT	conformal field theory
CL	Complex Langevin
CSA	Cartan subalgebra
EFT	effective field theory
IHMC	imaginary-mass Hybrid Monte Carlo
IR	infrared
LEC	low-energy constant
LFT	lattice field theory
MC	Monte Carlo
MCMC	Markov Chain Monte Carlo
NLSM	nonlinear sigma model
QCD	quantum chromodynamics
QFT	quantum field theory
RG	renormalization group
SNR	signal-to-noise ratio

SSB spontaneous symmetry breaking

WF Wilson-Fisher

Acknowledgements

I have been extremely fortunate in graduate school, and in life, to have had so many wonderful and interesting people around me to motivate me, support me, and challenge me.

In particular, I would like to sincerely thank my advisors, Roxanne Springer and Shailesh Chandrasekharan. I would also like to thank members of my PhD committee Ayana Arce, Harold Baranger, and Phil Barbeau for their feedback.

I would like to thank Hanqing Liu, Arman Margaryan and Mendel Nguyen for the constant physics adventures over the last six years. I have also benefited immensely from conversations with, and would like to thank, Shreya Arya, Paul Aspinwall, Moritz Binder, Lin Dai, Suresh Govindarajan, Austin Hulse, Abhishek Khetan. Xincheng Lin, Iman Marvian, Thomas Mehen, Abhishek Mohapatra, Son Nguyen, Ronen Plesser, Arya Roy, Xiaojun Yao, and Shiv Akshar Yadavalli. I would also like to thank Tanmoy Bhattacharya, Alex Buser, Joaquín Drut, Andrew Gasbarro, Rajan Gupta, Domenico Orlando, Lukas Rammelmüller, Susanne Reffert, Rolando Somma and Uwe-Jens Weise for useful conversations on parts of this work.

The material presented here is funded in part by the U.S. Department of Energy, Office of Science, Nuclear Physics program under award No. DE-FG02-05ER41368, and in part by the J. Horst Meyer Endowment fellowship from Duke Physics.

Chapter 1

Introduction

The sprawling framework of quantum field theory (QFT) is a fundamentally important aspect of modern physics. It is our best attempt yet for a fundamental description of nature, as evidenced by the success of the standard model of particle physics [1]. It quantitatively describes universal features of condensed matter systems close to criticality, and often provides a qualitative description elsewhere. It touches aspects of pure mathematics, and has given rise to ideas such as the renormalization group (RG), which have spawned areas of research in other fields such the study of classical dynamical systems.

Fundamental developments in our understanding of QFT have often paralleled the invention of new computational techniques. This is true of Feynman's diagrammatic methods during the beginnings of QFT [2], which not only gave a *perturbative definition* of QFT, but also enabled an algorithmic way to perform controlled quantitative computations in QFT, especially in weakly-coupled theories. This is also true for Wilson's formulation of lattice gauge theory [3] and the renormalization group [4, 5], which provided a concrete *non-perturbative* definition of QFT, and, at the same time, paved the way for the precision numerical studies of strongly coupled QFTs using Monte Carlo (MC) methods, such as the ongoing worldwide efforts in lattice quantum chromodynamics (QCD) .

Despite a long history of computational developments in QFT, lattice field theory (LFT) with MC methods remains the method general and powerful enough to make quantitative predictions in strongly coupled QFTs in arbitrary spacetime dimensions. Although there exist efficient numerical algorithms in low dimensions [6], and exact solutions in some rare cases [7, 8, 9], lattice MC methods

are undoubtedly the most widely-applicable technique, being applicable to one-dimensional spin systems, as well as four-dimensionsal nonabelian gauge theories. However, questions about nonequilibrium physics such as realtime dynamics are still out of reach for lattice MC methods due to a severe complex action problem.

However, with the advent of quantum computing, we might have new a way to approach such questions. There is a significant effort in the scientific community being devoted to develop techniques for simulating QFTs on quantum computers [10, 11, 12]. However, a successful real-world QFT calculation on a quantum computer will not only require significant advances in quantum algorithms and quantum hardware, but might also require us to find new formulations of lattice QFTs.

Traditionally, a lattice regularization of a continuum QFT involves mapping the QFT onto discrete spacetime in such a way that the local Hilbert space at each lattice site is preserved. In several cases, such as field theories with bosonic matter or gauge degrees of freedom, the local Hilbert space is infinite dimensional. However, this is a problem for the prospect of quantum simulation of QFTs, since near-term quantum computers are likely to be severely limited by the number of logical qubits available to represent the local Hilbert space at each site.

However, it is well-known that in several cases this requirement for the local Hilbert space to be preserved to regulate a QFT can be lifted, while still ensuring that all the symmetries of the quantum theory are intact. Indeed, the ideas of Wilson's RG demonstrate, with no regard for the dimensionality of the local Hilbert space, how lattice systems can give rise to continuum QFTs near second-order critical points. Therefore, a lattice model with a finite-dimensional Hilbert space can be used to study a desired continuum QFT, provided that the appropriate second-order critical point can be located. This idea is quite common in

condensed matter physics, but is often not considered from a particle physics point of view. However, such a regularization is very natural for quantum computers. Since the idea of quantum simulation make this kind of a regularization very appealing, we dub this approach *qubit regularization*.

It should be noted that such qubit regularizations for several QFTs have been achieved from a different perspective. For example, in the *D-theory* formulation [13, 14, 15], one can obtain the continuum limit of the asymptotically free $2d$ $O(3)$ nonlinear sigma model (NLSM) by the dimensional reduction of a $3d$ quantum spin system. The applicability of efficient cluster algorithms in this formulation has also enabled numerical work with $\mathrm{CP}(N-1)$ models [16, 17]. This approach has been extended to gauge theories such as QCD as well [14, 15], which are known as *quantum link* models. Such models can be considered as qubit regularizations as well. However, the dimensionsonal reduction of D-theory might not be a necessary ingredient in the construction of qubit regularizations.

In this thesis, we explore the program of qubit regularization and apply it to study strongly coupled QFTs.

$O(N)$ nonlinear sigma models

We first apply these ideas to a class of relativistic QFTs known as $O(N)$ NLSMs. The $O(N)$ NLSMs, for various N and spacetime dimensions, have a rich phenomenology. In spacetime dimensions $D \geq 3$, they find applications in describing magnetism , the superfluid transition in Helium-4 [18], and are believed to describe the spontaneous breakdown of chiral symmetry in two-flavor QCD with light quarks [19, 20, 21, 22, 23]. In $D = 2$ spacetime dimensions, the $O(N)$ NLSM are very special owing to their integrability [24], and offer an excellent toy model for QCD, displaying features such as asymptotic freedom, dynamical mass generation and dimensional transmutation.

Therefore, in Chapter 4, we develop a qubit regularization for the $O(N)$ NLSM.

In particular, we reformulate the traditional lattice $O(N)$ NLSM as a qubit model with an $N+1$ dimensional Hilbert space at each lattice site. Using an efficient worm algorithm in the worldline formulation, we demonstrate that the model has a quantum critical point in $(2+1)$ dimensions, and compute some critical exponents for $N = 2, 4, 6, 8$. By comparing the critical exponents with results from large-N and ϵ-expansions, we demonstrate that these quantum critical points lie in the $O(N)$ Wilson-Fisher (WF) universality class, and thus can be used to study the continuum physics of the $O(N)$ NLSM in three spacetime dimensions.

$O(N)$ NLSM in the large-charge sector

Next, in Chapter 5, we apply the $O(N)$ qubit models to complement the recent work on the large-charge expansion in conformal field theories (CFTs), as developed in Refs. [25, 26]. In these works, the authors showed that in a sector of fixed global charge Q for the $O(N)$ WF CFT, we can write down an effective field theory (EFT) with Q^{-1} as the expansion parameter. This is important because CFTs generically do not have a small parameter to enable perturbative control.

The large-charge EFT was used to compute anomalous dimensions of large-charge operators in the $O(N)$ WF CFT in terms of unknown low-energy constants (LECs). While these constants can in principle be determined from lattice MC computations of the traditional $O(N)$ lattice model, in practice such calculations suffer from a severe signal-to-noise ratio (SNR) problem.

Fortunately, an efficient MC algorithm can be developed in a qubit formulation, which can then be used to fix the unknown couplings in the EFT, as was done in Refs. [27, 28] for $O(2)$ and $O(4)$ WF CFTs. In this thesis, we extend these works to arbitrary $O(N)$ [29, 30] and compute the conformal dimensions for $N = 2, 4, 6, 8$ for charges up to $Q = 20$. This has allowed for a quantitative test of some new predictions for the $O(N)$ NLSM from a combined large-charge and large-N approach [31]. We find that the lattice computations agree well with the

large-N analytic predictions for the two leading couplings in the large-charge EFT.

Few-body physics of nonrelativistic fermions

Finally, we show that our qubit approach can also be used to study the few-body physics of non-relativistic particles. In particular, we study the physics of two-species of non-relativistic fermions in $1+1$ spatial dimensions. We develop a worldline formulation of this model. Using a worm algorithm, we perform computations of ground state energies for various mass-imbalances, coupling strengths, and particle numbers. We find that the worm algorithm performs very well across the entire parameter regime. Interestingly, we discover limitations of the recently proposed Complex Langevin (CL) method [32] for the same system for strong couplings.

Chapter 2

Renormalization group, continuum QFTs, and qubit models

We review the framework of Wilson's renormalization group. In particular, we emphasize how continuum quantum field theories emerge at second-order phase transitions, and how renormalization can be understood non-perturbatively within this framework. This is an essential ingredient in the construction of a qubit regularization.

Since the purpose of this thesis is to study quantum field theories (QFTs) from lattice models with finite dimensional local Hilbert spaces, we must understand how QFTs arise from such lattice models. The conceptual framework which explains this is called the renormalization group (RG).

We would like to emphasize that this chapter is merely expository in nature and nothing here is original. RG is a vast subject with many avatars. Therefore the choice of topics in this chapter are motivated in part by what we feel is relevant for this thesis, and in part by what used to greatly confuse the author. The presentation here is heavily inspired by the excellent discussions of Refs. [33, 34, 35], and we strongly recommend these original resources.

2.1 Fixed points and universality

We would like to study the long distance physics of a given lattice Hamiltonian H_0. We represent this Hamiltonian as a point $\vec{g}_0$ in an infinite dimensional coupling constant space. Let us assume that we have an RG transformation $\mathcal{R}_s$ corresponding to the scale factor $s > 1$. The transformations $\mathcal{R}_s$ can be thought of as inducing a transformation in the coupling constant space. Under repeated

applications of the transformation $\mathcal{R}_s$, the coupling constants $\vec{g}_0$ flow in this coupling constant space,

$$\{\vec{g}_0\} \xrightarrow{\mathcal{R}_s} \{\vec{g}_1\} \xrightarrow{\mathcal{R}_s} \cdots \xrightarrow{\mathcal{R}_s} \{\vec{g}_N\} \xrightarrow{\mathcal{R}_s} \cdots \ , \tag{2.1}$$

which corresponds to the sequence of lattice Hamiltonians

$$H_0 \xrightarrow{\mathcal{R}_s} H_1 \xrightarrow{\mathcal{R}_s} \cdots \xrightarrow{\mathcal{R}_s} H_N \xrightarrow{\mathcal{R}_s} \cdots \ , \tag{2.2}$$

which in general become more and more long ranged (in lattice units) and complicated to write down. The transformation $\mathcal{R}_s$ is constructed in such a way that the correlation functions are the same up to terms that decay faster than any power of s,

$$\langle \phi(x_1)\phi(x_2)\cdots\phi(x_k)\rangle_{N+1} = Z(s)^{k/2}\langle \phi(sx_1)\phi(sx_2)\cdots\phi(sx_k)\rangle_N + \cdots \tag{2.3}$$

where Z is an overall factor.

In an infinite volume, we can perform this transformation infinitely many times, and we shall assume that this is the case for the remainder of this section. We will come back to finite volume effects in Section 2.3. As we repeated apply $\mathcal{R}_s$ starting from $\vec{g}_0$, there are several types of qualitatively different RG flows that can emerge. We can imagine that the transformation $\mathcal{R}_s$ has a fixed point, for some initial starting point $\vec{g}_0$, such that

$$\lim_{N\to\infty} \mathcal{R}_s^N[\vec{g}_0] = \mathcal{R}_s[\vec{g}_*] = \vec{g}_* \tag{2.4}$$

Let us denote the Hamiltonian at $\vec{g}_*$ as H^*. As we will see, it is this simple assumption that leads to an elegant explanation of the phenomenon of universality, and the definition of continuum QFTs. Let us proceed.

We know how $\mathcal{R}_s$ acts on $\vec{g}_*$ from Eq. (2.4), but what happens if we start the

RG flow in the vicinity of $\vec{g}_*$? Let us linearize $\mathcal{R}_s$ around $\vec{g}_*$:

$$\mathcal{R}_s[\vec{g}_* + \Delta\vec{g}] = \mathcal{R}_s[\vec{g}_*] + T_s \cdot \Delta\vec{g} + O(\Delta\vec{g}^2) \tag{2.5}$$

where T_s is an infinite-dimensional matrix in the coupling constant space and the deviation $\Delta\vec{g}$ is a vector that lives in the tangent space at $\vec{g}_*$. Since the RG transformations $\mathcal{R}_s$ implement scaling by a continuous parameter s, the T_s operator must obey

$$T_s T_{s'} = T_{ss'} \tag{2.6}$$

for all $s, s' > 0$, which implies that the eigenvalues of T_s must be of the form s^λ. Assume that the operator T_s has a complete set of eigenvectors $\{\vec{e}_\lambda\}$ with eigenvalues s^λ, with real λ,

$$T_s \cdot \vec{e}_\lambda = s^\lambda \vec{e}_\lambda. \tag{2.7}$$

(In principle, λ could be complex suggesting the possibility of RG limit cycles, but we will assume that is not the case.) Then we may expand $\Delta\vec{g}$ in this basis as $\Delta\vec{g} = \sum_\lambda u_{\lambda,0}\vec{e}_\lambda$, where the coefficients $u_{\lambda,0}$ are called *scaling variables*. Under the action of T_s

$$\begin{aligned} T_s \cdot \Delta\vec{g} &= T_s \cdot \sum_\lambda u_{\lambda,0}\vec{e}_\lambda = \sum_\lambda u_{\lambda,0} T_s \cdot \vec{e}_\lambda \\ &= \sum_\lambda (u_{\lambda,0} s^\lambda)\vec{e}_\lambda = \sum_\lambda u_\lambda(s)\ \vec{e}_\lambda \end{aligned} \tag{2.8}$$

Therefore, we see that the $u_{\lambda,0}$ scale in a well-defined way under RG transformations,

$$u_\lambda(s) \equiv u_{\lambda,0} s^\lambda. \tag{2.9}$$

Now we can classify the RG flow around a fixed point $\vec{g}_*$. Close to an RG fixed point, the coupling is called *relevant*, *irrelevant* or *marginal* depending on the sign of the exponent λ in the eigenvalue s^λ:

$$T_s \cdot \vec{e}_\lambda = s^\lambda \vec{e}_\lambda \quad \text{with} \quad \begin{cases} \lambda > 0 & \text{relevant} \\ \lambda = 0 & \text{marginal} \\ \lambda < 0 & \text{irrelevant.} \end{cases} . \tag{2.10}$$

The eigenvectors $\vec{e}_\lambda$ are directions in the coupling constant space. The RG trajectories around the fixed point either flow out of the fixed point (for relevant directions), flow into the fixed point (for irrelevant directions), or form a line of RG fixed points (for marginal couplings). We can imagine following the RG flow backwards for each of the irrelevant directions, beyond the tangent space. The (infinite-dimensional) surface formed by the these RG trajectories is called the *critical surface*.

This is illustrated in Fig. 2.1, where we show the critical surface embedded in an infinite-dimensional space of all microscopic lattice Hamiltonians. Schematically, we show the critical surface as a two-dimensional surface. Each point on the critical surface is a lattice Hamiltonian which flows to the fixed point Hamiltonian H^* under RG transformations. Therefore, we get an infinite set of Hamiltonians which have the same long-distance physics as H^*. This is the explanation of *universality*. On the other hand, the RG flow in the relevant direction shown in Fig. 2.1 takes us out of the critical surface. We will discuss relevant directions in the next section.

But what does this have to do with criticality of lattice Hamiltonians? In fact, as the name suggests, all points on the critical surface are Hamiltonians tuned to a second-order critical point. This can be seen as follows. Let us say we start with a Hamiltonian H_0 that lies on the critical surface of H^*, and let the correlation length for H_0 be ξ_0 in lattice units. After each RG step $\mathcal{R}_s$, the

dimensionless correlation length diminishes by a factor of s

$$\xi_N \to \xi_{N+1} = \frac{\xi_N}{s}. \tag{2.11}$$

The correlation length at the fixed point must satisfy $\xi^* = \xi^*/s$, which implies $\xi^* = 0$ or $\xi^* = \infty$. The case of vanishing correlation length is trivial – it simply means that all the local degrees of freedom fluctuate independently, and therefore this is called a *trivial* fixed point. On the other hand, if the correlation length at the fixed point is infinite, $\xi^* = \infty$, then Eq. (2.11) implies that all points on the critical surface also have infinite correlation length. Therefore, each point on the critical surface is in fact a lattice Hamiltonian which has been tuned to a second-order phase transition. We say that that all these critical Hamiltonians lie in the *universality class* of the fixed point H^*.

The fixed points of RG describe scale invariant theories. This can be seen from Eq. (2.3), which implies that the correlation functions of a fixed point Hamiltonain H^* satisfy

$$\langle \phi(x_1)\phi(x_2)\cdots\phi(x_k)\rangle_* \sim \langle \phi(sx_1)\phi(sx_2)\cdots\phi(sx_k)\rangle_*. \tag{2.12}$$

Under certain assumptions, it can be shown that global scale invariance implies the much larger conformal symmetry [36, 37, 38, 39]. Therefore, in such cases, RG fixed points correspond to conformal field theories (CFTs).

It is then clear how to study CFTs from qubit models. To study the CFT given by H^*, we can study the long-distance physics of any lattice Hamiltonian on the critical surface of H^*. Physically, an arbitrary critical Hamiltonian lying on the critical surface of H^* has several short-distance scales (short compared to the correlation length). As we perform RG transformations, these short distance scales diminish. As the number of RG steps N becomes large, eventually all the finite length-scales disappear, and we are left only with the scale-invariant

physics of the longest distances. We will use this idea later extensively in Chapters 4 and 5 to study the CFT associated with the $O(N)$ Wilson-Fisher (WF) fixed point, which controls the continuum physics of the $O(N)$ nonlinear sigma model (NLSM).

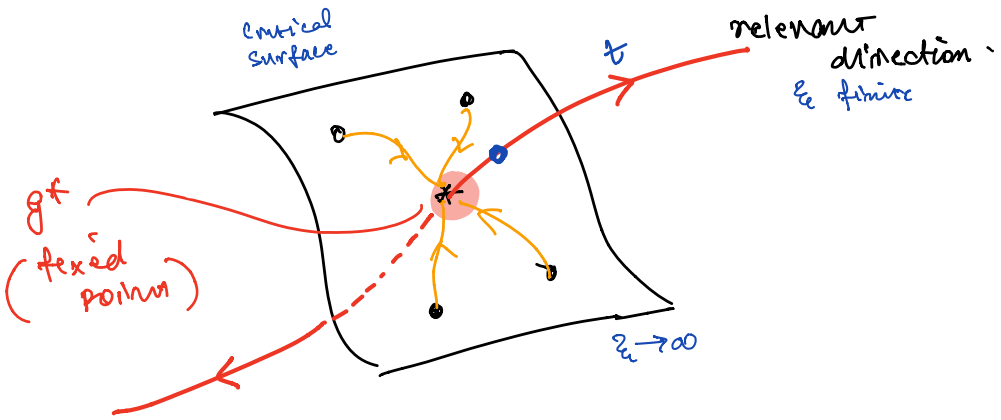

Figure 2.1: In the vicinity of an RG fixed point. Critical surface.

2.2 Continuum quantum field theories

In the latter part of the previous section, we considered irrelevant perturbations about the fixed point. The long distance physics of such Hamiltonians is described by scale-invariant, and in many cases even conformally invariant, theories. Even though it is generically impossible to write down an explicit form for the fixed point Hamiltonian, we can study these scale invariant theories by starting from a lattice Hamiltonian and studying its long distance physics.

However, our fundamental theories of elementary particles are not scale invariant. For example, quantum chromodynamics (QCD) has a characteristic scale of $\Lambda_{\text{QCD}} \sim 300\,\text{MeV}$. To define such QFTs with infrared (IR) scales, we have to move away from the fixed point in a relevant direction. By carefully looking at how the theory changes as we flow under RG, we can define a continuum limit of such a theory and understand the traditional notion of renormalization in

particle physics, non-perturbatively.

Let there be a fixed point Hamiltonian H^*. If we start at H^*, and turn on a *small* relevant coupling $u_{t,0}\vec{e}_t$ with RG eigenvalue s^{λ_t}, the RG flow will take us out of the critical surface,

$$\vec{g}(s) = \vec{g}_* + u_t(s)\vec{e}_t \quad \text{with} \quad u_t(s) = u_{t,0}s^{\lambda_t}, \tag{2.13}$$

which is true for infinitesimal perturbations. Strictly speaking, as we repeat the RG transformations, the relevant perturbation grows and the linear approximation in Eq. (2.13) breaks down. However, we can imagine following the trajectory beyond the linear approximation.

The curve traced by the RG flow of a purely relevant direction (that is, a perturbation about the fixed point that only has a single relevant component, and no irrelevant components) is called a *renormalized trajectory* [33]. In Fig. 2.1, it is schematically shown as a red line coming out of the critical surface. We will see that continuum QFTs are defined on such renormalized trajectories.

However, we typically never know H^* explicitly. It is usually much easier to find a lattice Hamiltonian that can be tuned to a critical point in the universality class of H^*. Let $H(\lambda)$ be such a Hamiltonian, where λ is a parameter that can be tuned to a critical point $\lambda = \lambda_c$. We call the Hamiltonian $H(\lambda)$ the "bare" Hamlitonian, and λ the bare coupling. At the critical point, the RG flow takes $H(\lambda_c)$ to the fixed point Hamiltonian H^*. In other words, $H(\lambda_c)$ and H^* differ only by irrelevant operators.

If we start the RG transformations with the coupling λ tuned slightly away from the critical point $\lambda = \lambda_c + \Delta\lambda$, then the corresponding RG trajectory will not flow into the fixed point. Instead, if λ is sufficiently close to the critical point, then the RG trajectory will eventually become very close to the renormalized trajectory after a sufficiently large number of RG steps. This is because, by taking λ slightly away from the critical point, we have introduced a small relevant

coupling. This makes the correlation length $\xi(\lambda)$ finite, although still very large in lattice units, which introduces an additional length scale in the system, apart from the short distance scales in the system. Since $H(\lambda)$ has other irrelevant operators, there are several other short distance scales that are much smaller than $\xi(\lambda)$. Let us call the largest of these scales $l'(\lambda)$. So we have a hierarchy of length scales,

$$a = 1 \ll l'(\lambda) \ll \xi(\lambda), \tag{2.14}$$

where the lattice spacing a is unity since we measure everything in units of the lattice spacing. The scale hierarchy is shown in Fig. 2.2.

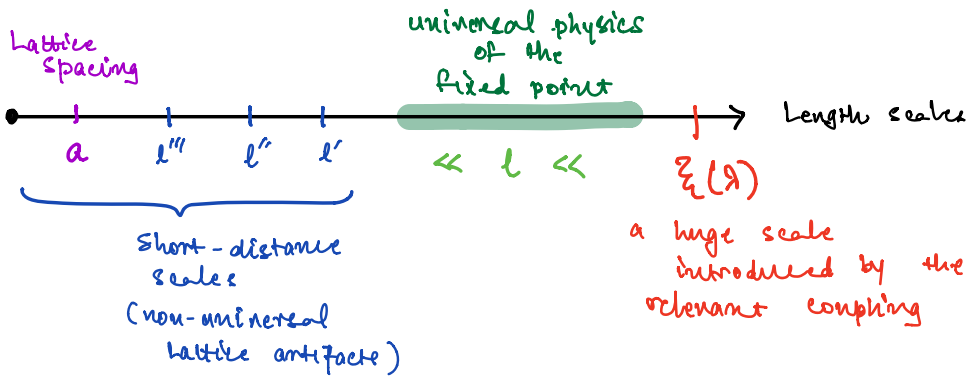

Figure 2.2: A generic picture of the length scales in a Hamiltonian tuned close to a second-order critical point.

As we perform RG transformations $\mathcal{R}_s$, these length scales diminish by a scale factor s at each step: $l \to l/s$. Let $N_1(\lambda)$ be the number of RG steps it takes to bring down l' to unity, and let $N_2(\lambda)$ be the number of steps needed to bring $\xi(\lambda)$ down to unity,

$$l'(\lambda) s^{-N_1(\lambda)} = 1 \tag{2.15}$$

$$\xi(\lambda) s^{-N_2(\lambda)} = 1. \tag{2.16}$$

The hierarchy in length scales (2.14) can equivalently be written as a hierarchy in the number of RG steps,

$$N_2(\lambda) \gg N_1(\lambda) \gg 1. \tag{2.17}$$

After N_1 RG steps, we land in the vicinity of the fixed point H^*. At this point on the RG trajectory, the effects of the irrelevant operators have washed away but the correlation length is still extremely large. We start seeing the universal physics of the fixed point H^*. If we continue the RG flow beyond N_1 steps, the relevant perturbation grows larger and takes us away from the fixed point. However, if λ is sufficiently close to λ_c, the RG flow stays close to the renormalized trajectory as it flows away from the fixed point. We show this procedure schematically in Fig. 2.3. We use the notation that after N RG steps, the Hamiltonian is $H_N(\lambda)$, the correlation length (in lattice units) is ξ_N, and the various short distance scales become l'_N. We get a series of Hamiltonians and length scales

$$\text{Hamiltonian} \quad H_0 \to \quad H_1 \to \quad \cdots \to \quad H_{N_1} \to \qquad \cdots \to \quad H_{N_2} \tag{2.18}$$

$$\text{Correlation length} \quad \xi_0 \to \quad \xi_1 \to \quad \cdots \to \quad \xi_{N_1} \to \qquad \cdots \to \quad \xi_{N_2} = 1 \tag{2.19}$$

$$\text{Short-distance scales} \quad l'_0 \to \quad l'_1 \to \quad \cdots \to \quad l'_{N_1} = 1 \to \quad \cdots \to \quad l'_{N_2} \approx 0. \tag{2.20}$$

So far, everything was measured in lattice units since the lattice Hamiltonian $H(\lambda)$ does not know about the physical ("lab") units. To introduce lab units, we fix a physical length scale for the Hamlitonian at N_2. For example, we can declare that the mass of the lightest particle in the theory is known to be m_{phys} in lab units, say, $m_{\text{phys}} = 1\,\text{MeV}$. But the correlation length ξ (in lattice units) and the physical mass m_{phys} can be related to each other if we know the value of

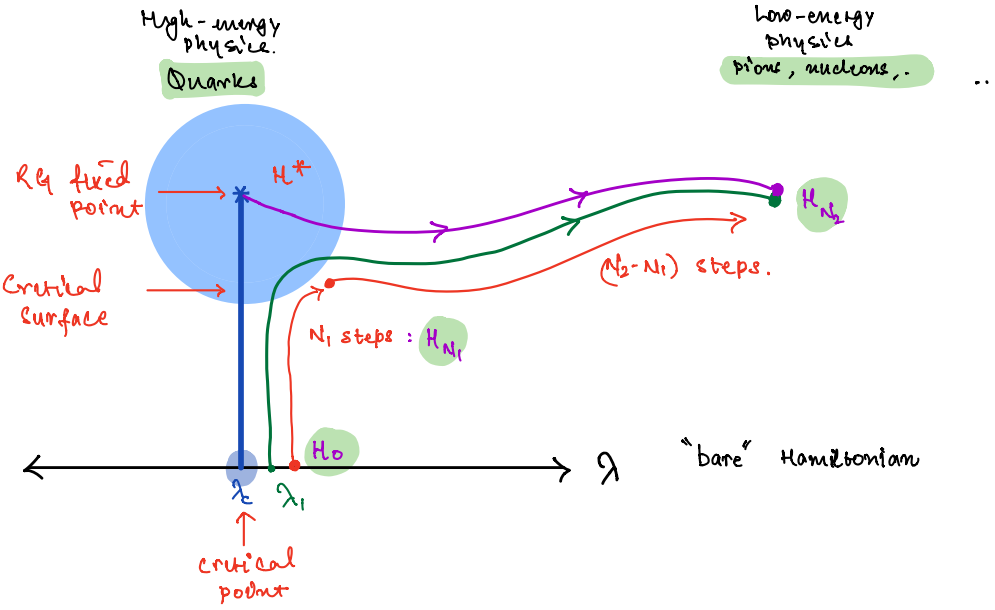

Figure 2.3: Non-perturbative renormalization. We have a lattice Hamiltonian with λ as the "bare" coupling. The coupling can be tuned to a second-order critical point $\lambda = \lambda_c$. An RG flow starting from λ_c will end up at the RG fixed point H^*. Starting from $\lambda = \lambda_1$, we can perform $N_1(\lambda_1)$ steps to land in the vicinity of H^*, but after that we flow away from H^*. We define the low-energy physics by performing a total of $N_2(\lambda_1)$ steps, which brings the correlation length $\xi(\lambda_1)$ down to $\xi_{N_2}(\lambda_1) = 1$.

the lattice spacing a (or momentum cutoff Λ) *in physical units*,

$$m_{\text{phys}} = \frac{1}{a_{N_2}\xi_{N_2}} = \frac{\Lambda_{N_2}}{\xi_{N_2}} \tag{2.21}$$

which gives a cutoff of $\Lambda_{N_2} = m_{\text{phys}}\xi_{N_2} = 1\,\text{MeV}$. This defines the value of the cutoff (or lattice spacing) in physical units for the Hamiltonian $H_{N_2}(\lambda)$.

At N_2, we have a theory given by H_{N_2} with a cutoff $\Lambda_{N_2} = 1\,\text{MeV}$, and a mass of $m_{\text{phys}} = 1\,\text{MeV}$. Taking the continuum limit corresponds to pushing the cutoff to infinity. This can be done now, by simply retracing our RG trajectory backwards from N_2 to 0.

At each backward step, we keep the physical mass fixed to m_{phys}, but the correlation length increases by a scale factor s, Therefore the cutoff in physical

units

$$\Lambda_N = m_{\text{phys}} \xi_N \tag{2.22}$$

must also increase by the same factor. We therefore get a series of Hamiltonians each with a larger and larger cutoff in physical units as we retrace the RG trajectory backwards,

$$\begin{array}{lccccc} \text{Hamiltonian} & H_0 & \leftarrow H_1 & \leftarrow \cdots & \leftarrow H_{N_2-1} & \leftarrow H_{N_2} \end{array} \tag{2.23}$$

$$\begin{array}{lccccc} \text{Cutoff} \\ \text{(physical units)} & \Lambda_0 = s^{N_2}\Lambda_{N_2} & \leftarrow s^{N_2-1}\Lambda_{N_2} & \leftarrow \cdots & \leftarrow s\Lambda_{N_2} & \leftarrow \Lambda_{N_2} \end{array} \tag{2.24}$$

In physical units, the cutoff at the lattice scale is thus $\Lambda_0 = s^{N_2}\Lambda_{N_2}$, and the cutoff corresponding to the short distance scales l' is $\Lambda_{N_1} = s^{N_2-N_1}\Lambda_{N_2}$. The various length scales (in lattice units) in Eq. (2.14) translate to the following hierarchy for the cutoffs in physical units:

$$1 \ll l'(\lambda) \ll \xi(\lambda) \tag{2.25}$$

$$\Lambda_0 \gg \Lambda_{N_1} \equiv \Lambda_{\text{UV}} \gg \Lambda_{N_2} \equiv \Lambda_{\text{IR}} \tag{2.26}$$

The maximum cutoff occurs for the Hamiltonian H_0 at the lattice scale,

$$\Lambda_0 = \xi_0(\lambda) m_{\text{phys}}. \tag{2.27}$$

But we know that as we tune λ to the critical point λ_c, the correlation length will diverge. Therefore, the cutoff in physical units will diverge as well. This is the essence of *non-perturbative renormalization*. Given any "bare" lattice Hamiltonian

tuned close to criticality with correlation length $\xi_0(\lambda)$, we can invert Eq. (2.27) to define the bare coupling λ as a function of the cutoff, $\lambda(\Lambda_0)$. This tells us how we must change the bare coupling as the cutoff is taken to be larger and larger, such that the low-energy physics at H_{N_2} remains fixed. In other words, as we take the bare coupling closer to the critical point

$$\lambda \to \lambda_c \tag{2.28}$$

$$H_{N_2} \to H_{\text{IR}} \qquad \text{“Low-energy” physics} \tag{2.29}$$

$$H_{N_2-N_1} \to H^* \qquad \text{“High-energy” physics} \tag{2.30}$$

$$H_0 = H(\lambda) \to H(\lambda_c) \tag{2.31}$$

Note that H_{IR} lies exactly on the renormalized trajectory. In fact, the entire trajectory between N_1 and N_2 steps will tend towards the renormalized trajectory as we approach the critical point. In the $\lambda \to \lambda_c$ limit, we define a *continuum* QFT as the series of Hamiltonians lying on the renormalized trajectory, which are all carefully constructed to have higher and higher cutoffs, but the same low-energy physics. The universal physics of the quantum field theory emerges in the regime $\Lambda_{\text{UV}} \gg p \gg \Lambda_{\text{IR}}$, where p is a scale where we probe the system. Above Λ_{UV}, we start seeing the non-universal effects of the irrelevant terms.

We note that in order to truly take the cutoff to infinity, we must be able to come arbitrarily close to the critical point. This can be of importance practically. For example, if the bare Hamiltonian $H(\lambda)$ does not contain a critical point in its parameter space, it might still be that the RG trajectory passes by very close to the fixed point for some λ_1. In that case, Λ_{UV} will become very large but will eventually saturate since we cannot take $\lambda \to \lambda_c$. We will not be able to take the continuum limit completely, but the low-energy physics up to the scale Λ_{UV} will match with the continuum theory. We have an effective field theory with a finite cutoff, but not a continuum QFT.

2.2.1 Asymptotically free QFTs

In the above construction, if the fixed point H^* is a Gaussian fixed point, then the continuum QFT so defined is called *asymptotically free*. The most well-known, and arguably the most important, example of an asymptotically free theory is QCD.

In asymptotically free QFTs such as QCD, the low-energy regime is non-perturbative. So usually we are interested in studying the physics of H_{N_2}, defined at the scale Λ_{N_2}. As long as we know that the bare Hamiltonian has a second-order critical point, then we can study the physics of H_{N_2} by studying length scales $l \gg l_1(\lambda) \gg 1$, where $l_1(\lambda)$ is the largest of short-distance lattice artifacts.

On the other hand, what if we wanted to show that a particular bare Hamiltonian model defines an asymptotically free QFT? Or what if we do not know whether the critical point exists for a given bare Hamiltonian? Or perhaps, in numerical computations, we can only approximately find the critical point. How can we show that such a Hamiltonian defines an asymptotically free theory?

To study the physics of the fixed point, we have to study the bare Hamiltonian at an intermediate length scale l such that

$$\xi(\lambda) \gg l \gg l' \gg 1, \tag{2.32}$$

where $\xi(\lambda)$ is the correlation length, l' is the largest of the short distance scales (in other words, lattice artifacts). This ensures that we are in the vicinity of the fixed point H^*, far from the low-energy physics of H_0, as well as far from the non-universal physics at the lattice scale. Clearly, unless we can find the critical point exactly, studying the physics numerically at such intermediate scales can be tricky.

2.3 Finite size scaling

Since all the numerical computations are performed for a finite system, the above RG analysis needs to incorporate that. This means that the universal predictions above cannot be directly used since the finite volume introduces another length scale in the problem. But it turns out that certain finite size effects are universal as well, and we can leverage the finite size scaling to study the fixed point as well. This is a powerful technique and we will use this extensively in the later chapters of the thesis.

Let's start with the scaling of the free energy under RG transformations $\mathcal{R}_s$ in the infinite volume close to the fixed point. Let us assume that there are two relevant perturbations u_t and u_h, with scaling dimensions y_t and y_h respectively,

$$u_t \to u_t' = s^{y_t} u_t, \tag{2.33}$$

$$u_h \to u_h' = s^{y_h} u_h. \tag{2.34}$$

Let $f(u_t, u_h)$ be the free energy density and let $f_{\text{sing}}(u_t, u_h)$ be its singular part. Then the singular part of the free energy density $f_{\text{sing}}(u_t, u_h)$ transforms as

$$f_{\text{sing}}(u_t, u_h) = s^{-d} f_{\text{sing}}(u_t', u_h') \tag{2.35}$$

$$= s^{-d} f_{\text{sing}}(s^{y_t} u_t, s^{y_h} u_h). \tag{2.36}$$

Using just Eq. (2.36), we can derive several universal relations among physical quantities. For example, we can show that the critical exponents are universal by relating them to the scaling dimensions of the relevant perturbations.

Some of simplest critical exponents are defined by the behaviour of specific heat as the system undergoes a phase transition. Let us consider a magnetic system, and let us assume that the Hamiltonian under study has parameters t, h corresponding to the deviation from critical temperature T_c and magnetic field

H_C, respectively,

$$t \sim T - T_C, \quad h \sim H - H_c. \tag{2.37}$$

The specific heat per unit volume is related to the free energy as $c \sim \dfrac{\partial^2 f}{\partial t^2}$ evaluated at $h = 0$.

As $|T - T_C| \sim t \to 0$, the critical behavior of the specific heat is given by

$$c \sim t^{-\alpha} \tag{2.38}$$

where α is a critical exponent. The scaling variables u_t, u_h are in general a complicated function of the Hamiltonian parameters t, h. However, they are analytic functions of t, h at the critical point $(t, h) = (0, 0)$. Therefore, for t, h small enough, we can assume $u_t \propto t$ and $u_h \propto h$ up to irrelevant constants, provided that they are protected by symmetries from mixing with each other at leading order. (For example, we may assume that the system has as Z_2 symmetry that is broken by the magnetic field coupling h.)

To find α we need to find the scaling of the free energy with t for $h = 0$. For this, let us choose the scale factor s such that the transformed relevant variable $s^{y_t} u_t$ is of order one: $s^{y_t} u_t \equiv \tilde{u}_t = O(1)$. This gives

$$f_{\text{sing}}(u_t, u_h) = \left(\frac{u_t}{\tilde{u}_t}\right)^{d/y_t} f\left(\tilde{u}_t, \left(\frac{u_t}{\tilde{u}_t}\right)^{-y_h/y_t} u_h\right) \tag{2.39}$$

Set $h = 0$, and differentiate with respect to t to get

$$\frac{\partial^2 f}{\partial t^2} = c\ t^{d/y_t - 2} f_{\text{sing}}(\tilde{u}_t, 0) \tag{2.40}$$

Therefore we get $\alpha = d/y_t - 2$. Similarly, we can find other critical exponents. The details can be found in standard textbooks, such as the ones mentioned in the beginning of this chapter.

We see that the critical exponents are universal and related to the scaling dimensions of the scaling variables at a fixed point.

But now, we can use this idea to characterize the finite size effects as well. Let us put the system in a box of size L (in lattice units) along one direction, such that the total volume is L^d. The free energy will depend on L now. For simplicity, let's say that there is only one other relevant parameter u_t. Since $L^{-1} \to sL^{-1}$ under RG transformations, we can think of L^{-1} as a relevant parameter with scaling dimension 1:

$$f_{\text{sing}}(u_t, L^{-1}) = s^{-d} f_{\text{sing}}(s^{y_t} u_t, sL^{-1}). \tag{2.41}$$

To find the scaling of physical observables with L, let us choose s such that $sL^{-1} = 1$. We get

$$f_{\text{sing}}(u_t, L^{-1}) = L^{-d} f_{\text{sing}}(L^{y_t} u_t, 1) \tag{2.42}$$

$$= L^{-d} \Phi(L^{y_t} u_t) \tag{2.43}$$

where $\Phi(z)$ is a universal function. This means that if we had data for $f_{\text{sing}}(u_t, L^{-1})$ for a range of t and L, then all the data points for $f_{\text{sing}}(u_t, L^{-1})L^d$ when plotted against $L^{y_t} u_t$ will lie on a *single* curve $\Phi(L^{y_t} u_t)$. This suggests a powerful method for identifying the critical points in a Hamiltonian, and the critical exponents.

For concreteness, let us look at an observable that is typically easy to measure in numerical computations, such as the susceptibility

$$\chi(t, L) = \left. \frac{\partial^2 f}{\partial h^2} \right|_{h=0} \tag{2.44}$$

We can use the same technique to find the scaling behaviour of susceptibility.

$$f_{\text{sing}}(t, h, L^{-1}) = L^{-d}\ \Phi(tL^{y_t}, hL^{y_h}). \tag{2.45}$$

Differentiating with respect to h twice, and taking $h \to 0$, we get

$$\chi(t, L) = L^{2y_h - d} \psi(tL^{y_t}) \tag{2.46}$$

where $\psi(x)$ is a universal function. In terms of the parameters of the Hamiltonian, we may write

$$\chi(T, L) = L^{2y_h - d}\ \psi((T - T_c)L^{y_t}). \tag{2.47}$$

Therefore, by measuring $\chi(T, L)$ for different L for several T close to T_c, we can plot $\chi(T, L)L^{d-2y_h}$ against T. For the right y_h, all the curves will pass through the same point at $T = T_c$, which allows us to very precisely identify the critical point. Furthermore, for $\chi(T, L)L^{d-2y_h}$ plotted as a function of $L^{y_t}(T - T_C)$, all data points for various T, L must collapse to a *single* curve. This phenomenon is known as *scaling collapse*. We will use this technique extensively in the later chapters to determine the critical point and study the properties of the fixed point.

Chapter 3

Worldline formulations and worm algorithms

We review the mapping of the quantum statistical mechanics of a d-dimensional system to the classical statistical mechanics of a $(d+1)$-dimensional system. This leads us to the idea of worldline representations and using Monte Carlo algorithms to study quantum systems. We describe the idea of worm algorithms, which form the basis of all the numerical work in this thesis.

3.1 Quantum-to-classical mapping and Monte Carlo methods

Given a Hamiltonian H in d spatial dimensions, we would like to compute observables in a quantum statistical mechanical system. The expectation value of a quantum observable $\hat{O}$ may be computed as

$$\langle \hat{O} \rangle = Z^{-1} \operatorname{Tr}\left[\hat{O} e^{-\beta H}\right] \tag{3.1}$$

at inverse temperature β, where the normalization factor Z

$$Z = \operatorname{Tr} e^{-\beta H}, \tag{3.2}$$

is called the *partition function* of the system.

It is well-known that the quantum statistical mechanics of a system in d spatial dimensions can be mapped to the classical statistical mechanics of a system in $(d+1)$ Euclidean spacetime dimensions. Since classical statistical mechanics can be studied with Monte Carlo (MC) calculations, we can therefore

study the system given by Eq. (3.2). Moreover, as we will see, there is a freedom in the choice of basis for the classical system. By exploiting this freedom, we can derive several alternative classical representations of the same quantum system. However, not all representations lend themselves to efficient MC algorithms. To study the system, we need to combine a 'sign-problem' free representation with efficient sampling algorithms.

Although the quantum-to-classical mapping is well-known [40], let us review it here for completeness. We imagine β as the total extent in the imaginary time direction. It is convenient to divide β into T time steps of size ε, such that $T\varepsilon = \beta$. We write the partition function as

$$Z = \lim_{\varepsilon \to 0} \mathrm{Tr}\left[e^{-\varepsilon H} \cdots e^{-\varepsilon H}\right]. \tag{3.3}$$

At each time step t_k, we introduce a complete set of states in some basis $\sum_n |n\rangle\langle n| = \mathbb{I}$.

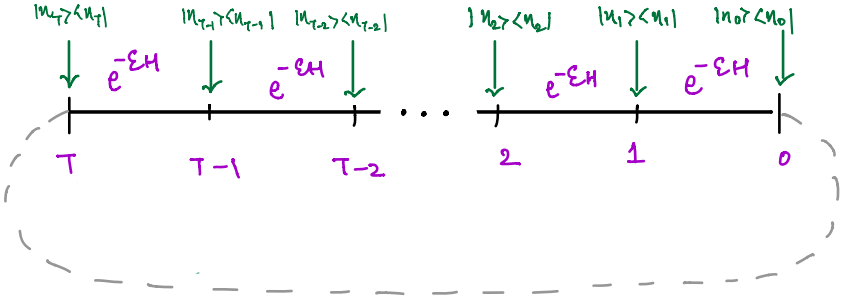

The trace can be written as

$$Z = \sum_{\substack{n_0, n_1, \ldots, n_T \\ n_T = n_0}} \langle n_T | e^{-\varepsilon H} | n_{T-1} \rangle \langle n_{T-1} | \cdots | n_1 \rangle \langle n_1 | e^{-\varepsilon H} | n_0 \rangle \tag{3.4}$$

$$\equiv \sum_{\substack{n(t) \\ n(\beta) = n(0)}} K[n(t)]. \tag{3.5}$$

In the last line, we have defined a *configuration* $n(t)$, where $n(k\varepsilon) \equiv n_k$ label an

orthonormal basis $\{|n_k\rangle\}$ inserted at imaginary time $t = k\varepsilon$. We define a functional $K[n(t)]$ which is just the product of all transfer matrix elements

$$K[n(t)] \equiv \lim_{\varepsilon \to 0} \prod_{i=0}^{T-1} \langle n_{i+1} | e^{-\varepsilon H} | n_i \rangle \tag{3.6}$$

The trace in the definition of the partition function (3.2) translates to summing over configurations $n(t)$ with periodic boundary conditions in imaginary time $n(\beta) = n(0)$.

Now, if the choice of basis $|n\rangle$ was such that the functional $K[n(t)] \geq 0$ for all configurations $n(t)$, then we may interpret it as the weight of a configuration $n(t)$ in expression (3.5). We can define the probability $P[n(t)]$ of a configuration $n(t)$ as

$$P[n(t)] \equiv \frac{K[n(t)]}{\sum_{n(t)} K[n(t)]} = Z^{-1} K[n(t)]. \tag{3.7}$$

Therefore, if we can sample configurations $n(t)$ with the probability distribution (3.7), then we can compute the expectation values for an operator $\hat{O}$

$$\langle \hat{O} \rangle = Z^{-1} \operatorname{Tr} \hat{O} e^{-\beta H} \tag{3.8}$$

$$\equiv \sum_{n(t)} O[n(t)] P[n(t)]. \tag{3.9}$$

where the operator functional $O[n(t)]$ can be derived from the operator $\hat{O}$ by inserting the operator in the derivation given above.

We emphasize that in defining the probability distribution above in Eq. (3.7), we assumed that the functional $K[n(t)]$ was positive semidefinite for all configurations $n(t)$ that contribute to the partition function. However, this is generically not true. Often, it turns out that for a given choice of basis, the positivity of $K[n(t)]$ cannot be guaranteed. If that this is the case, $K[n(t)]$ cannot be interpreted as probabilities. In several cases like these, it can becomes very nontrivial

to develop a sampling algorithm that lets us compute observables with favorable signal-to-noise ratios.

3.2 Worldline representations

Equations (3.7) and (3.9) can be interpreted to define the classical statistical mechanics of a system that can exist in a configuration $n(t)$ with probability $P[n(t)]$. As noted above, the configurations $n(t)$ take values in a set that labels the choice of basis $|n\rangle$ chosen to evaluate the matrix elements in the quantum-to-classical mapping.

In this thesis, we are interested in a class of representations for the classical system which are referred to as *worldline* representations. Generally speaking, worldline representations correspond to choosing the occupation number basis in deriving the quantum-to-classical mapping (see Section 3.1).

Worldline representations are interesting for two main reasons. The first is that they can lead to new insights into the physics of the sign problem [41]. Another very important reason is that there is a class of very efficient sampling algorithms called "worm" algorithms that can be developed for worldline representations. The majority of the numerical work in this thesis is based on the application of worm algorithms to worldline representations.

We will work with two quantum mechanical systems in this thesis. In Chapters 4 and 5, we will study an $O(N)$ symmetric lattice Hamiltonian. We will describe in detail the construction of a worldline representation of the $O(N)$ model in Section 4.4.1, and a worm algorithm for it in Section 4.4.2. We also study a lattice descretization of a system of non-relativistic fermions in Chapter 6, using a worldline representation that we elaborate in Section 6.3.

3.3 Markov Chain Monte Carlo

Let us say that we would like to generate configurations from a set $\mathcal{C} = \{\mathcal{C}_1, \ldots, \mathcal{C}_k\}$ with the weights W_i for $\mathcal{C}_i$. The probability for the configuration $\mathcal{C}_i$ is

$$P_i = \frac{W_i}{\sum_{j=1}^{k} W_j}. \tag{3.10}$$

Let us assume that we have an algorithm which probabilistically generates sequences of the type,

$$X_1 \to X_2 \to \cdots X_N, \tag{3.11}$$

given an initial configuration X_1, such that each $X_i \in \mathcal{C}$ is any of the configurations from $\mathcal{C}$. Let the number of occurences of the configuration $\mathcal{C}_i$ in the above sequence (3.11) be n_i. The goal of a MC sampling algorithm is to generate a sequence such that

$$\lim_{N\to\infty} \frac{n_i}{N} = P_i \quad \text{for} \quad i = 1, \ldots, k. \tag{3.12}$$

If we have an observable defined on each configuration $O(\mathcal{C})$, then we compute the expectation value of the observable by computing

$$\langle O \rangle = \lim_{N\to\infty} \frac{O(\mathcal{C}_i) n_i}{N}. \tag{3.13}$$

The most widespread method to generate such sequences is called a Markov Chain Monte Carlo (MCMC). In such an algorithm, the probability of generating a configuration X_{i+1} from X_i does not depend on the history $\{X_1, \ldots, X_{i-1}\}$. We will see that in such algorithms, coupled with some additional requirements, we can ensure that the probability distribution tends to the desired one as the sequence grows larger.

Let us assume that the transition probability at each step is given by a $k \times k$ matrix T such that the probability of generating the configuration $\mathcal{C}_j$ in the next step, given that the current state of the algorithm is $\mathcal{C}_i$ is T_{ji}.

We would like to impose a condition on the transition matrix that will help us ensure the correct probability distribution. Let $\vec{w} = (W_1, \ldots, W_k)$ be a column vector of all the weights. Then we require that the transition matrix T is such that w is a right-eigenvector of T with eigenvalue one:

$$T \cdot \vec{w} = \vec{w}. \tag{3.14}$$

Even though this is enough to guarantee that the Markov Chain will generate the correct distribution, in practice we impose a stronger condition:

$$W_i T_{ij} = W_j T_{ji} \quad \text{for all } i, j = 1, \ldots, k. \tag{3.15}$$

This is called *detailed balance*. It can be seen by summing over the index j that Eq. (3.15) implies Eq. (3.14). The benefit of requiring this stronger condition is that it is typically much easier to construct algorithms that obey detailed balance. Together with the assumption of *ergodicity*, the convergence of a MC algorithm is guaranteed [35].

Even though a given MC algorithm may converge to the correct distribution, in practice the various configurations generated X_i are not statistically independent. How many steps it takes for an algorithm to generate statistically independent data points for an observable can be characterized by the autocorrelation time. A large autocorrelation time τ effectively reduces the number of statistically independent samples by a factor of $\sim \tau$, therefore the errors become larger as well.

Worm algorithms

In all the numerical work in this thesis, we use a class of algorithms called *worm algorithms* [42]. They are very efficient in the sense that they greatly reduce the autocorrelation times compared to traditional MC algorithms, and yet can be implemented with local updates. Since the details of the worm algorithms are different for each model we study in this thesis, we describe the worm algorithm for each model in their respective Sections 4.4.2, 5.4.3 and 6.4. For a more general introduction to the idea of worm algorithms, we refer the reader to the treatments in Refs. [43, 44].

Chapter 4

$O(N)$ qubit models in $D \geq 3$ spacetime dimensions

We develop a qubit regularization of the $O(N)$ nonlinear sigma model in $D \geq 3$ spacetime dimensions. Using an efficient lattice Monte Carlo method in $D = 3$, we compute several observables close to the critical point. We compare against existing results in the literature for the $O(N)$ Wilson-Fisher universality class. We find excellent agreement, indicating that our model lies in the same universality class.

4.1 Introduction

In this chapter, we develop a qubit regularized $O(N)$ model. This work was published in Ref. [45] for $N = 1, 2, 3$ and the generalization to arbitrary N was published as a preprint in Ref. [29].

The $O(N)$ nonlinear sigma models (NLSMs) are relativistic quantum field theories (QFTs) that have a wide applicability in both particle and condensed matter physics. We begin in Section 4.2 with a brief review of the definitions and physics of the continuum $O(N)$ nonlinear sigma models in various dimensions.

Since the $O(N)$ NLSMs are bosonic field theories, they naturally are defined with an infinite dimensional Hilbert space at each lattice site. In Section 4.3, we construct an $O(N)$ symmetric qubit model, and argue that this model has a second-order critical point in $D \geq 3$ spacetime dimensions. In $D = 3$, this critical point must lie in the Wilson-Fisher (WF) universality class.

The next step is to use numerical techniques to locate the critical point and compute its properties. In such qubit models, it is generally very hard to show analytically that the critical point is in a certain universality class. But we can

use well-established lattice Monte Carlo (MC) methods and finite size scaling techniques to study the critical point, and compute several universal quantities that help us identify the corresponding fixed point.

A major advantage of qubit models is that they can be recast easily in a worldline representation. This enables the use of a highly efficient class of MC methods called worm algorithms. We discuss our numerical techniques in Section 4.4. In particular, using the worm algorithm we can compute some critical exponents, which act as a signature of the universality class.

Since the $O(N)$ NLSM is a well-known and widely-applicable QFT, there is a vast literature on the subject and much is known. For our purposes, this means that we can compare our results for the critical exponents to existing results in the literature for the WF universality class. There are several other methods used in the literature, like large-N, ϵ-expansion, conformal bootstrap, and lattice MC approaches using the traditional model. In Section 4.5, we perform a comparison across these results and confirm that our models agree with existing results for the critical exponents. This provides strong evidence that the model is in the expected universality class.

Having established that our qubit model indeed reproduces the physics of the $O(N)$ NLSM, and armed with an efficient MC algorithm to study it, in the next chapter we will use our qubit model to study the $O(N)$ WF fixed point in sectors of large global charge.

4.2 $O(N)$ nonlinear sigma model

In the continuum, the $O(N)$ NLSM is a QFT of N-component bosonic scalar fields $\vec{\phi} \in \mathbb{R}^N$, described by the following action in d dimensional Euclidean space

$$S = -\frac{1}{g^2} \int d^d x \, \partial_\mu \vec{\phi} \cdot \partial_\mu \vec{\phi} \tag{4.1}$$

with the constraint $|\vec{\phi}|^2 = 1$. The $\vec{\phi}$ field vector thus lives on a $(N-1)$-dimensional sphere S^{N-1}.

Alternatively, we can be more concrete and start with a lattice model and use the ideas of renormalization group (RG) to define the $O(N)$ NLSM more concretely (following the discussion in Chapter 2). Recall that, given an RG fixed point, there are an infinity of lattice models that describe the same universal physics of the fixed point. Traditionally, the $O(N)$ sigma models have been studied using the lattice action

$$S_L = -\frac{1}{g^2} \sum_{\langle ij \rangle} \vec{\phi}_i \cdot \vec{\phi}_j \tag{4.2}$$

defined on a d-dimensional Euclidean lattice and where $\langle ij \rangle$ runs over all bonds $\langle ij \rangle$ between sites i and j. To distinguish it from the "qubit" model we define later, we shall refer to the action in Eq. (4.2) as the *traditional* $O(N)$ model.

In dimensions $d = 2, 3, 4$, this model has a second order critical point. Therefore, we can define the continuum $O(N)$ NLSM using the lattice model (4.2) tuned close to the critical point $g = g_c$. This approach lends itself to non-perturbative lattice field theory techniques. The $O(N)$ model has been the object of extensive studies over the past decades [46], and displays a rich phenomenology.

In $d = 4$ dimensions, it is believed that the critical point is controlled by the Gaussian fixed point, with a marginally irrelevant perturbation. Therefore, the continuum $d = 4$ theory is just the free field theory, and there is no nontrivial continuum limit.

In $d = 3$, however, the critical point is controlled by a non-trivial fixed point, called the WF fixed point [47], which has one relevant perturbation. The scale invariant theory associated with this fixed point is a conformal field theory (CFT) called the Wilson-Fisher CFT. In general, $O(N)$ scalar field theories in $d = 3$ are known to have two fixed points – the Gaussian fixed point, and the WF fixed point. Unlike $d = 4$, where the interaction term is marginally irrelevant around

the Gaussian fixed point, the interaction in $d = 3$ is a relevant perturbation. In perturbation theory, therefore we can see that a generic $O(N)$ lattice model will flow away from the Gaussian fixed point. If the mass of the theory is tuned to zero, then the RG trajectory will flow to the WF fixed point.

The case of the two dimensional $O(N)$ NLSM is arguably the most interesting one, owing to the similarities with quantum chromodynamics (QCD). In two dimensions, the $O(N)$ NLSM is believed to be asymptotically free for $N \geq 3$ and exhibits other features of QCD such as dimensional transmutation and dynamical mass generation. However, in this work, we do not consider the 2-dimensional $O(N)$ NLSM and leave it for a future publication.

4.3 Qubit model

A note on notation

While discussing the $O(N)$ group, there is a slight notational inconvenience to distinguish between the case where N is odd or even. To make it easier to discuss both cases at once, we shall define an integer n such that $N \equiv 2n$ for N even, and $N \equiv 2n+1$ for N odd. We also define the set of integers I_N and K_N,

$$I_N \equiv \begin{cases} \{1, \ldots, 2n\} & \text{for } N = 2n \\ \{0, \ldots, 2n\} & \text{for } N = 2n+1, \end{cases} \tag{4.3}$$

$$K_N \equiv \begin{cases} \{-n, \ldots n\} \backslash \{0\} & \text{for } N = 2n \\ \{-n, \ldots, n\} & \text{for } N = 2n+1. \end{cases} \tag{4.4}$$

4.3.1 Some useful facts from the representation theory of the $O(N)$ group

Let $\{|i\rangle \;\big|\; i \in I_N\}$ be a basis for the fundamental representation of the $O(N)$ group. We take this to be the Cartesian basis, such that a rotation $R \in O(N)$ acts on the basis vector $|i\rangle$ as

$$|i\rangle \to R_{ji}|i\rangle \tag{4.5}$$

where R is an $N \times N$ matrix satisfying $R^T R = \mathbb{I}$. It will be more convenient for us to work in a basis where the states diagonalize a Cartan subalgebra of the $\mathfrak{o}(N)$ Lie algebra. Physically, such a basis consists of states with well-defined $O(N)$ charges.

For both N even and odd, we define h_i ($i = 1, \ldots, n$) as the generator of rotations in the $(2i-1, 2i)$ plane,

$$h_i = i(E_{2i,2i-1} - E_{2i-1,2i}) \quad \text{for} \quad i = 1, \ldots, n, \tag{4.6}$$

where $E_{i,j}$ is an $N \times N$ matrix whose (i, j) element is one, and all other matrix elements are zero. The h_i commute with each other,

$$[h_i, h_j] = 0 \quad \text{for all} \quad i, j = 1, \ldots, n. \tag{4.7}$$

Since this is also the maximal set of mutually commuting generators, the $\{h_i | i \in 1, \ldots, n\}$ form a basis for the Cartan subalgebra (CSA) of the $\mathfrak{o}(2n)$ lie algebra.

Since all the Cartan generators commute with each other, they can be simultaneously diagonalized. We can construct a new basis $|\vec{q}_k\rangle$ ($k = \pm 1, \ldots, \pm n$) labeled by the eigenvalues of the Cartan generators h_i. The eigenbasis of h_i, found by an

explicit diagonlization of Eq. (4.6), can be expressed as

$$|\vec{q}_{\pm k}\rangle = \begin{cases} \frac{1}{\sqrt{2}}\left(|2k-1\rangle \pm i|2k\rangle\right) & \text{for } k = 1,\ldots,n, \\ |0\rangle & \text{for } k = 0 \text{ (if } N \text{ is odd).} \end{cases} \tag{4.8}$$

where the vectors $\vec{q}_k \equiv (q_k^1,\ldots,q_k^n)$ $(k \in K_N)$ label the eigenvalues of the corresponding eigenstate $|\vec{q}_k\rangle$ under the Cartan generators $h_1,\ldots,h_n$,

$$h_j|\vec{q}_k\rangle = q_k^j|\vec{q}_k\rangle, \quad \text{with} \quad (\vec{q}_{\pm k})_j = \begin{cases} \pm\delta_{kj} & \text{for } k = 1,\ldots,n. \\ 0 & \text{for } k = 0. \end{cases} \tag{4.9}$$

Under an $O(N)$ rotation generated by the Cartan generators, parameterized by $\vec{\theta} = (\theta_1,\ldots,\theta_n)$, the state $|\vec{q}_k\rangle$ transforms with just an overall phase

$$|\vec{q}_k\rangle \to e^{i\vec{\theta}\cdot\vec{h}}|\vec{q}_k\rangle = e^{i\vec{\theta}\cdot\vec{q}_k}|\vec{q}_k\rangle. \tag{4.10}$$

In this sense, we say that the state $|\vec{q}_k\rangle$ has the $O(N)$ charge $\vec{q}_k$ $(k \in K_N)$. We note that, if N is odd, then we have a state $|\vec{q}_0\rangle$ which has zero charges,

$$\vec{q}_0 = (0,\ldots,0). \tag{4.11}$$

We shall call the basis given by Eq. (4.8) the *spherical basis*, in analogy with rotations in 3 spatial dimensions, where we often use this basis:

$$|\pm\rangle = |x\rangle \pm i|y\rangle, \quad |0\rangle = |z\rangle, \tag{4.12}$$

where $\{|x\rangle, |y\rangle, |z\rangle\}$ are orthonormal vectors in the Cartesian basis.

Some useful invariants

To write down the $O(N)$ invariant Hamlitonian, let us list a few invariant terms in the spherical basis. The first, trivially invariant, term is

$$\mathbb{I} = \sum_{i \in I_N} |i\rangle\langle i| = \sum_{k \in K_N} |\vec{q}_k\rangle\langle\vec{q}_k|. \tag{4.13}$$

We will also need an invariant in the tensor product of two fundamental representations. The term

$$\sum_{i \in I_N} |ii\rangle = \sum_{k \in K_N} |\vec{q}_k, \vec{q}_{-k}\rangle \tag{4.14}$$

is also invariant, since it transforms as

$$\sum_{i \in I_N} |ii\rangle \to \sum_{i,j,k, \in I_N} R_{ij} R_{ik} |jk\rangle = \sum_{j,k \in I_N} (R^T R)_{jk} |jk\rangle = \sum_{j \in I_N} |jj\rangle, \tag{4.15}$$

where we have used that the matrix R is orthogonal: $R^T R = \mathbb{I}$.

Now, we can define the Hilbert space for our quantum system, and use the above invariants to write down an $O(N)$ invariant "qubit" Hamiltonian.

4.3.2 The Hamiltonian

To construct a qubit model for the $O(N)$ NLSM, let us begin with the definition of the Hilbert space. The full Hilbert space $\mathcal{H}$ is the tensor product of *local* Hilbert spaces $\mathcal{H}_x$ at each lattice site,

$$\mathcal{H} = \otimes_x \mathcal{H}_x, \tag{4.16}$$

where x varies over all lattice sites. We take the local Hilbert space $\mathcal{H}_x$ to be a direct sum of a singlet representation and fundamental representations of the

$O(N)$ group.

$$\mathcal{H}_x = \mathcal{H}_x^{(0)} \oplus \mathcal{H}_x^{(1)}. \tag{4.17}$$

where $\mathcal{H}_x^{(0)}$ is the one-dimensional singlet representation, and $\mathcal{H}_x^{(1)}$ is the N-dimensional fundamental representation.

Let the singlet Hilbert space $\mathcal{H}_x^{(0)}$ be spanned by a normalized vector $|\varnothing\rangle$. It will be convenient to think of this state as the Fock vacuum. For the fundamental representation $\mathcal{H}_x^{(1)}$, we define "single-particle" states using the spherical basis defined in the previous section.

$$\mathcal{H}_x^{(1)} \equiv |\vec{q}_{-n}\rangle_x \oplus |\vec{q}_{-n+1}\rangle_x \oplus \cdots \oplus |\vec{q}_{n-1}\rangle_x \oplus |\vec{q}_n\rangle_x, \tag{4.18}$$

where we omit the state $|\vec{q}_0\rangle$ for N even. We interpret the state $|\vec{q}_k\rangle \in \mathcal{H}_x^{(1)}$ as a particle of charge $\vec{q}_k$.

We can take the identification of $|\vec{q}_k\rangle$ as a single-particle state further and define "creation" and "annihilation" operators at each lattice site x, which can respectively be written as

$$c_{x,k}^\dagger = |\vec{q}_k\rangle_x \langle\varnothing|_x, \quad \text{and} \tag{4.19}$$

$$c_{x,k} = |\varnothing\rangle_x \langle\vec{q}_k|_x, \tag{4.20}$$

where $k \in K_N$. We think of the operators $c_{x,k}^\dagger$ and $c_{x,k}$ as creating and annihilating particles of charge $\vec{q}_k$ at the site x. However, we emphasize that these are not creation/annihilation operators in the usual sense of the word, since they do not satisfy either bosonic or fermionic commutation relations. (In condensed matter literature, such operators are often referred to as Hubbard operators. See, for example, Ref. [48].)

Note that applying a creation operation twice on an empty site gives zero. In

other words, we do not allow more than one particle at a site. So in a sense the particles obey the Pauli exclusion principle and are similar to fermions in that respect. However, these operators are not truly fermionic since they commute at different lattice sites. We call such particles *hard-core* bosons.

Using the $O(N)$ invariants listed in the previous section, we can now write down an $O(N)$ invariant Hamiltonian with nearest-neighbor terms,

$$\begin{aligned} H = J_1 \sum_{\substack{x \\ k \in K_N}} c^\dagger_{x,k} c_{x,k} + J_2' \sum_{\substack{\langle xy \rangle \\ k \in K_N}} \left(c^\dagger_{x,k} c_{y,k} + c^\dagger_{y,k} c_{x,k} \right) \\ + J_2 \sum_{\substack{\langle xy \rangle \\ k \in K_N}} \left(c^\dagger_{x,k} c^\dagger_{y,-k} + c_{x,k} c_{y,-k} \right) \end{aligned} \tag{4.21}$$

where x runs over all lattice sites, and $\langle xy \rangle$ runs over all nearest neighbor sites. We work with periodic boundary conditions in space. Setting $N = 3$, we can see that this is exactly the $O(3)$ qubit model that we constructed in Ref. [45].

4.3.3 Critical point and continuum limit

We can now heuristically argue that the model given in (4.21) has a phase transition in $d \geq 2$ spatial dimensions. In this work, we shall consider only $J_2, J_2' > 0$. For simplicity, we take $J_2 = J_2' > 0$, and let $\lambda \equiv J_1/J_2$.

First we consider the $\lambda \gg 1$ regime. In this limit, the fundamental states are energetically suppressed due to the J_1 term in the Hamiltonian. The ground state of the theory is therefore dominated by the singlets. In the $\lambda \to \infty$ limit, the ground state is just the Fock vacuum $|\Omega\rangle = |\varnothing\varnothing\cdots\varnothing\rangle$, with each site x being in the singlet state $|\varnothing\rangle_x$. Making the λ finite but large and positive will introduce fluctuations in the system due to the creation and annihilation of the single particle states. Since the lowest excited states consist of energetically costly N-tuplet of particles, the system is gapped in this regime. The correlation length is finite.

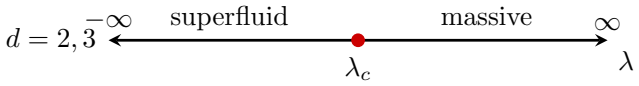

Figure 4.1: The zero temperature phase diagram of our qubit Hamiltonian in $d = 2, 3$.

On the other hand, as we take λ large and *negative*, the fundamental states $|\pm q_i\rangle$ start to dominate the ground state. Since the Hamiltonian is $O(N)$ symmetric, the ground state must be $O(N)$-degenerate. In the thermodynamic limit, this $O(N)$ symmetry must be spontaneously broken in $d \geq 2$, giving rise to gapless Goldstone modes.

Therefore, as we tune λ from large and positive to large and negative, at some critical $\lambda = \lambda_c$, the system must undergo a phase transition associated with the spontaneous breaking of the $O(N)$ symmetry. If the phase transition is second order, then a continuum QFT should emerge at the critical point, according to the ideas of Wilson's RG described in Chapter 2. In $d \geq 2$, we expect the emergent QFT to be precisely the $O(N)$ NLSM, which is controlled by the Wilson-Fisher fixed point in $d = 2$ and the Gaussian (free) fixed point in $d = 3$ (with a marginally irrelevant parameter).

Our aim in this work to is to develop the worldline formulation and worm algorithm to numerically verify this heuristic argument. If the continuum QFT is indeed the $O(N)$ NLSM, then this opens up the possibility of studying the physics of the continuum $O(N)$ NLSM using such qubit models.

4.4 Numerical techniques

4.4.1 $O(N)$ qubit model: worldline representation

In this section, we construct a worldline representation (see Chapter 3) for our $O(N)$ qubit model (4.21). We begin by splitting the Hamiltonian into single-site

and two-site operators,

$$H = H^{(1)} + H^{(2)}. \tag{4.22}$$

Here $H^{(1)}$ is a sum over all the single-site terms, and $H^{(2)}$ is the sum over all nearest neighbor terms,

$$H^{(1)} = \sum_i H_i^{(1)}, \quad H^{(2)} = \sum_{\langle ij \rangle} H_{ij}^{(2)}, \tag{4.23}$$

where i runs over all the spatial lattice sites of the system, and $\langle ij \rangle$ runs over all nearest neighbor spatial bonds in the system. We take the representation of the partition function in Eq. (3.5) as our starting point,

$$Z \equiv \sum_{\substack{n(t) \\ n(\beta)=n(0)}} K[n(t)] \tag{3.5}$$

where the functional $K[n(t)]$ is given by Eq. (3.6),

$$K[n(t)] \equiv \lim_{\varepsilon \to 0} \prod_{i=0}^{T-1} \langle n_{i+1} | e^{-\varepsilon H} | n_i \rangle. \tag{3.6}$$

and $n(t)$ are "configurations" that take values in a set that labels some eigenbasis $\{|n\rangle\}$ at each (imaginary) time t. Worldline representations correspond to choosing the occupation number basis as the eigenbasis $\{|n\rangle\}$, which are eigenstates of the $H^{(1)}$,

$$H^{(1)}|n\rangle = E_1(n)|n\rangle. \tag{4.24}$$

Let us compute the transfer matrix elements

$$T_{i+1,i} \equiv \langle n_{i+1} | e^{-\varepsilon H} | n_i \rangle \tag{4.25}$$

in the occupation number basis. We approximate the matrix exponential as

$$e^{-\varepsilon(H^{(1)}+H^{(2)})} = e^{-\varepsilon H^{(1)}}\left(1-\varepsilon H^{(2)}+O(\varepsilon^2)\right), \tag{4.26}$$

and evaluate the transfer matrix elements in the occupation number basis,

$$\begin{aligned} T_{k+1,k} &= \langle n_{k+1}|e^{-\varepsilon H^{(1)}}\left(1-\varepsilon H^{(2)}+O(\varepsilon^2)\right)|n_k\rangle \\ &= e^{-\varepsilon E_1(n_{k+1})}\left(\delta(n_{k+1},n_k)-\varepsilon\sum_{\langle ij\rangle}\langle n_{k+1}|H^{(2)}_{ij}|n_k\rangle\right)+O(\varepsilon^2). \end{aligned} \tag{4.27}$$

where the sum on the right hand side is over all nearest neighbors $\langle ij\rangle$.

So far everything we did was true for any nearest neighbor Hamiltonian. Now we invoke our knowledge of the Hilbert space and the Hamiltonian. Equation (4.27) suggests that we can diagrammatically represent the action of a single application of the transfer matrix on a state $|n_\tau\rangle$ by considering its action on a pair of neighboring sites at a given (imaginary) time slice, say, $t = \tau\varepsilon$. At time step τ, we represent each site on the lattice by a dot. If the site is in the empty state $|\varnothing\rangle$, then we leave the dot as it is.

$|\varnothing\rangle$

However, if the local state is one of fundamental states $|\vec{q}_i\rangle$, we draw an oriented worldline passing through it, with the direction depending on the sign of the charge $\vec{q}_{\pm i}$. For example, we draw $|\vec{q}_1\rangle$ as an upward arrow, and $|\vec{q}_{-1}\rangle$ as a downward arrow.

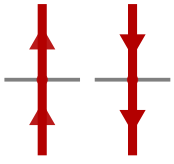

$|\vec{q}_1\rangle \quad |\vec{q}_{-1}\rangle$.

We interpret upward and downward arrows as particles and antiparticles moving forward in time, respectively. To distinguish the various charge states, it helps to associate each charge $\vec{q}_k$ $(k = 1,\ldots,N)$ with a color. So we represent the charges $\vec{q}_{\pm 1}$ by an oriented red worldline, the charge $\vec{q}_{\pm 2}$ by an oriented blue worldline, and so on. If N is odd, then we also have the state $|\vec{q}_0\rangle$. Since the charge $\vec{q}_0$ is zero, and therefore its own antiparticle, it is an unoriented worldline. Therefore, a given site in the occupation number basis $|n_\tau\rangle_x$ can be in any of the following states:

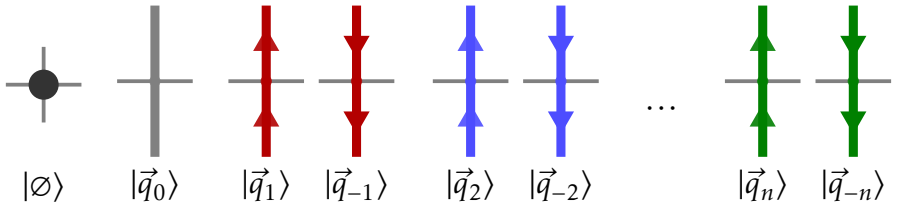

The action of the 2-site operators in this representation has a nice visual interpretation as well. We consider each nearest-neighbor term in the Hamiltonian in turn.

1. A pair creation/annihilation event on neighboring sites x and y:

$$J_2 \sum_{k\in K_N} \left(c^\dagger_{x,k} c^\dagger_{y,-k} + c_{x,k} c_{y,-k}\right) = J_2 \sum_{k\in K_N} \left(|\vec{q}_k,\vec{q}_{-k}\rangle\langle\varnothing\varnothing| + |\varnothing\varnothing\rangle\langle\vec{q}_k,\vec{q}_{-k}|\right) \quad (4.28)$$

   If the neighboring sites x,y are empty $|\varnothing\varnothing\rangle$, then an application of this operator can produce a particle and anti-particle pair $|\vec{q}_k,\vec{q}_{-k}\rangle$ of any color k. Conversely, if there is a particle/anti-particle pair at neighboring sites, this operator will annihilate them into singlets. We therefore represent the action of this term, as well as it's value, diagrammatically as

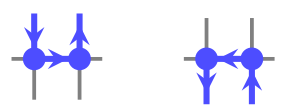

where we define $W_t = e^{-\varepsilon J_1}$, which is just the contribution from the single-site term in the Hamiltonian.

2. A nearest neighbor hop between sites x and y:

$$J_2' \sum_{k \in K_N} \left(c_{x,k}^\dagger c_{y,k} + c_{y,k}^\dagger c_{x,k} \right) = J_2' \sum_{k \in K_N} \left(|\vec{q}_k, \varnothing\rangle\langle \varnothing, \vec{q}_k| + |\varnothing, \vec{q}_k\rangle\langle \vec{q}_k, \varnothing| \right) \tag{4.29}$$

This term in the Hamiltonian will take a pair of neighboring sites where exactly one is filled and the other is empty, and just exchange the two sites. In the worldline language, this looks like a particle hopping from site to another, and can be represented as:

$(\varepsilon J_2')W_t^2$ $(\varepsilon J_2')W_t^2$

Now we can put everything together and see the worldline picture emerge. Starting with any state $|n_0\rangle$ at $t = 0$, we evolve this state with repeated applications of the transfer matrix. In the worldline formulation, this means picking one of the moves listed above, or just going straight through. That is, on each time step, either the particles can go forward, hop by one lattice site in any spatial direction, or pair create/annihilate. For every such move, we pick up a "weight" corresponding to it.

Because of the periodic boundary conditions in imaginary time, the worldlines must close on themselves at $t = \beta$. Therefore, we see that the partition function (3.2) has been rewritten as a sum over closed oriented worldlines of n colors,

$$Z_{\mathrm{WL}} = \sum_{n(t)} W[n(t)] \tag{4.30}$$

where $n(t)$ is a configuration consisting of (possibly disconnected) colored, ori-

Table 4.1: Local weights in the worldline representation of the $O(N)$ qubit model

Move	Weight
Temporal hop	$W_t \equiv e^{-\varepsilon J_1}$
Spatial hop	$W_s \equiv \varepsilon J_2'$
Pair creation/annihilation	$W_p \equiv \varepsilon J_2$

ented spacetime loops and $W[n(t)]$ is weight of the configuration which is just the product of the weights at each bond, as described above. We also list the local weights in Table 4.1 for convenience. In the worldline representation, the $O(N)$ symmetry is manifested in the fact that the weights are identical across all colors.

Finally, we note that the above derivation is strictly correct only in the $\varepsilon \to 0$ limit. But Eq. (4.30) can be studied as a model of colored loops in spacetime in its own right, even with ε finite. For arbitrary local weights (or couplings in the Hamiltonian) and large ε, the physics of the loop model could be qualitatively different from the Hamiltonian (4.21) that we started with. However, if the Hamiltonian has a quantum critical point which is described by a relativistic fixed point, then we can expect Z_{WL} to also have a critical point in the same universality class. If we are interested only in the physics of the fixed point, then we can use Z_{WL} as well, and set the spatial local weights equal to temporal local weights. This gives us a model with manifest symmetry between space and time.

Our task now is to develop a MC method which can efficiently sample the configurations in the partition function Eq. (4.30). We do this in the next section.

4.4.2 Worm algorithm for the $O(N)$ qubit model

As we discussed in Chapter 3, worldline representations have the advantage that there is a class of algorithms, called worm algorithms, which can be used to sample worldline configurations very efficiently. In this section, we describe a worm algorithm for the worldline representation constructed above [45, 28].

For the $O(N)$ model, we have oriented worldlines of n colors, where we recall the definition $n \equiv N/2$ for N even, and $n \equiv (N-1)/2$ for N odd. For N odd, we additionally have an additional type of worldline which is unoriented, corresponding to the zero charge state in the qubit model.

A worm algorithm works by sampling configurations in a "worm sector." We extend the partition function Z to include also configurations with a single source (the worm head) and a sink (the worm tail) of any color We call such a configuration a worm configuration. The full partition function can be written as

$$Z' = Z + Z_w \tag{4.31}$$

where Z is the original partition function in the worldline formulation, and Z_w is the partition function that sums over worm configurations. Note that the overall weights between Z and Z_w do not matter for any observable.

In the next subsections, we first describe the "begin/end" updates that take us back and forth between the default and worm sectors. Then we describe the "move" updates which are used in the worm sector to generate new configurations.

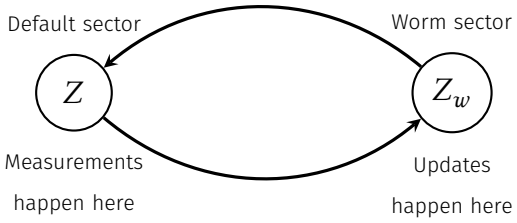

Begin/end updates

Given a configuration in the Z sector, we begin the worm update by picking a spacetime site x at random and proposing to create a worm head and tail at that site, thereby entering the worm sector. The reverse move, from within the worm sector, would be to close the worm if the worm head and tail are on the same site, exiting the worm sector.

During the begin move, there are two local configurations possible at the chosen site, and we perform a different update depending on it. We show these two updates in Fig. 4.2. For each of the two 'begin' moves, there is a corresponding 'end' move, which ends the worm update. We use a simple metropolis update to satisfy detailed balance for each move Section 3.3.

- B1 $\leftrightarrow$ E1: The first possibility is that the site x is empty. This is the B1 configuration in Fig. 4.2. In this case, we select a color c at random, and propose to create a worm head and tail of color c at the site x. The reverse move is that if the worm head and tail are at the same site, then we propose to exit the worm sector.

- B2 $\leftrightarrow$ E2: The second possibility is that the randomly chosen site x is already filled – that is, it has an incoming and an outgoing bond of some color c. Let the neighbor in the direction of the incoming bond be y. In this case, we propose to delete the incoming bond $\langle xy \rangle$, place the worm tail at x, and place the worm head at y. That is, we propose to create the local configuration E2 to enter the worm sector. Conversely, the worm update can end starting at E2, if we propose to move the worm head to a neighboring site which contains the worm tail.

Once we are in the worm sector using one of the two updates above, now the worm head travels through the spacetime lattice, changing the configurations as it moves. We now describe these moves.

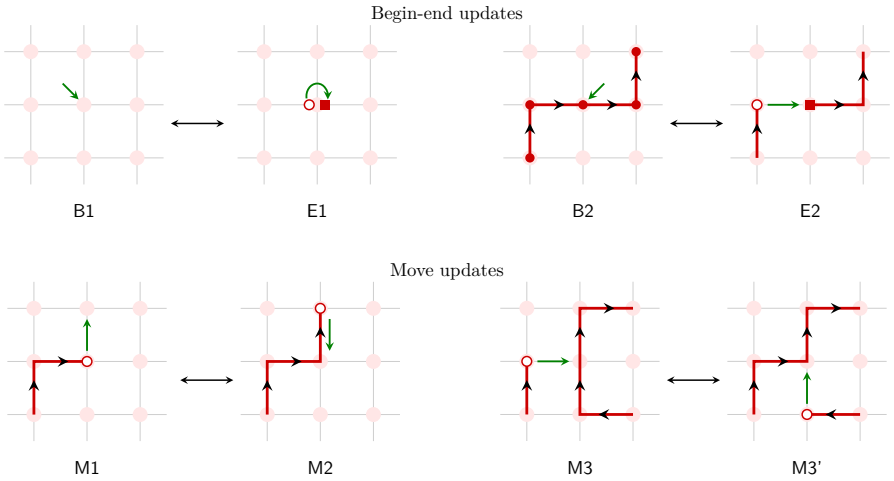

Figure 4.2: Local configurations for the worm head. We show pairs of configurations that can transform into each other during a worm update with probabilities obeying detailed balance. B1 and B2 are not worm configurations, but are the two local configurations where a worm update can begin. All other configurations shown are local configurations around the worm head. E1, E2 are the two ways a worm update can end. The configuration pairs (M1, M2) and (M3,M3′) are local configurations that can transform into each other during the "move" updates.

Move updates

Once we are in the worm sector, the worm head moves according to the 'moves' updates, shown in bottom row of Fig. 4.2.

On each update, we first propose one of $2D$ nearest neighbors for the worm head to hop to (where D is the spacetime dimension). We choose this direction at random. Let the worm head be currently at site x, and the let the nearest neighbor in the proposed direction by y. Which update we use depends on the local configuration at y. As we show in the bottom row of Fig. 4.2, there are only two possibilities

- M1 $\to$ M2: If the site y is empty, then we just propose to move the worm head from x to y. This will take the configuration to M2.

- M2 $\to$ M1: On the other hand, if the proposed direction is itself towards an incoming bond, that is, $\langle xy \rangle$ is the incoming bond, then we propose

to delete the incoming bond $\langle xy \rangle$ and move the worm head to y. This is the reverse of the previous update, and these two satisfy detailed balance among each other.

- M3 $\leftrightarrow$ M3′: It could also be that the site proposed site y is completely filled – that is, it already has incoming and outgoing bonds of some color c' passing through it. If the color c' of the bonds at y does not match the color of the worm, we simply reject this proposal. However, if the colors match, then we do the following. Let the incoming bond at y be $\langle zy \rangle$, where z is a nearest neighbor of y. In this case, we propose to create the bond $\langle xy \rangle$, delete the bond $\langle zy \rangle$, and move the worm head to z. The reverse of this move is an identical move.

- E2 $\rightarrow$ B2: The last possibility is that the proposed site y contains the worm tail. In this case, this is in fact, the second 'end' update discussed in the previous subsection. We propose to move the worm head x to the worm tail y. If accepted, then we exit the worm sector.

Finally, we note that if the loop is unoriented, then there is no distinction between incoming and outgoing bonds. For such worldlines, we need to modify the above updates. This can be done by selecting one of the two bonds at random whenever an incoming bond is needed, while taking care to ensure that the detailed balance equations are satisfied.

Global color/orientation flip

Finally, we add another type of update, one that is not local. In this update, we again begin by picking a site at random. If the site is empty, we do nothing. However, let us assume there is a loop of some given color and orientation passing through the site. In this case, we select a new color and orientation at random, and update the entire loop to have this new color and orientation. Such

global updates make it much easier for the algorithm to explore the configuration space. We find that enabling this update greatly reduces autocorrelation times, especially for larger N.

4.4.3 Observables

Vacuum density

Several observables are easily computable in our approach. The first, and the simplest, is the *vacuum density*, which we define as the average density of vacuum sites

$$v = \frac{1}{Z}\,\mathrm{Tr}\left(\frac{1}{L^d}\sum_x P_x^{\varnothing} e^{-\beta H}\right), \tag{4.32}$$

where $P_x^{\varnothing} = |\varnothing\rangle_x\langle\varnothing|_x$ is the projector onto the singlet state at the site x. For a given worldline configuration, this can be measured simply by computing the expectation value of the total number of vacuum sites on the spacetime lattice.

$O(N)$ charges

The next set of observables are the n types of $O(N)$ charges,

$$\langle Q_k\rangle = \frac{1}{Z}\,\mathrm{Tr}\left(\sum_x \hat{Q}_{x,k} e^{-\beta H}\right) \quad \text{for } k = 1,\ldots,n\,, \tag{4.33}$$

where the operator $\hat{Q}_{x,k}$ measures the local charge $\vec{q}_{\pm k}$ at the site x,

$$\hat{Q}_{k,x} = c^\dagger_{x,k}c_{x,k} - c^\dagger_{x,-k}c_{x,-k} \quad \text{for } k = 1,\ldots,n. \tag{4.34}$$

Since the worldlines in our formulation have well-defined $O(N)$ charges by construction, we can easily measure any of the $O(N)$ charges. For a given worldline configuration, all the $O(N)$ charges are conserved. Therefore, to

measure the charge $\hat{Q}_k$ for a particular k, we pick a time slice (say $t = 0$), and count (with orientation) the number of worldlines of the color k passing through it. Due to the $O(N)$ symmetry, all the $O(N)$ charges are in fact the same. We can use this fact to average over all colors and increase the statistics n-fold.

In the continuum QFT formalism, we typically use the charges as a probe for the spontaneous breakdown of symmetry. In infinite volume, a nonzero expectation value of any of the charges signals spontaneous symmetry breaking (SSB). However, we note that since lattice calculations are always performed in finite volume, there is no SSB. So, if the partition function has an $O(N)$ symmetry, the expectation values of all the charges $\langle \hat{Q}_k \rangle$ must in fact vanish in a lattice calculation.

Even though the charges are zero for the case considered in this work, it is still useful to measure this observable. This is because we can study sectors of fixed (non-zero) global charge by introducing a chemical potential for the charges. Further, this gives an additional check on the correctness of the algorithm when we compare the worm algorithms with exact results on small lattices.

$O(N)$ current-current susceptibility

An important observable is the $O(N)$ current-current susceptibility which can be measured by computing

$$\rho_s^{(k)} = \frac{1}{L^{d-2}\beta} \langle (N_w^{(k)})^2 \rangle, \quad \text{for } k = 1, \ldots, n, \tag{4.35}$$

where d is the number of spatial dimensions, k is a color, $k = 1, \ldots, n$ is a given color, and $N_w^{(k)}$ is the winding number of color-k worldlines in a configuration.

Again, the $O(N)$ symmetry ensures that $\rho_s^{(k)}$ will be identical for all colors k. Therefore, we average over all colors k to improve the statistics. From now on, we drop the color superscript k, and just denote this observable by ρ_s.

Susceptibility of the two-point function

The final observable is the susceptibility of the two-point correlation function of charge $\vec{q}_{\pm k}$ particles,

$$\chi_k = \frac{1}{ZL^d} \sum_{x,y} \int_0^\beta dt \, \mathrm{Tr}\left(e^{-(\beta-t)H} \hat{O}_{y,k} e^{-tH} \hat{O}^\dagger_{x,k} \right), \quad \text{for } k = 0, 1, \ldots, n \tag{4.36}$$

where we omit $k = 0$ (unoriented worldlines) if N is even, and the operator $\hat{O}_{x,k}$ defined as

$$\hat{O}^\dagger_{x,k} = (c^\dagger_{x,k} + c_{x,-k}), \tag{4.37}$$

creates particles and annihilates anti-particles.

Measuring this is particularly nice in worm algorithms, since in the worm sector, we already sample configurations with a creation and annihilation operator at different spacetime sites, with the correct weights. We therefore have to just count the number of configurations generated in the worm sector for a color k, and that gives us χ_k. As before, we average over all colors to improve statistics, and denote the susceptibility as χ.

4.4.4 Fits to the scaling behaviour

As described in Section 2.3, physical observables exhibit scaling behaviour near a critical point. In particular, the two observables current-current susceptibility ρ_s and susceptibility χ, defined above in Section 4.4.3 should behave as

$$\rho_s(J; L) = \frac{1}{L^{D-2}} f(u) \tag{4.38}$$

$$\chi(J; L) = L^{2-\eta} g(u), \tag{4.39}$$

where D is the spacetime dimension, $u = (J - J_c)L^{1/\nu}$ is the scaling variable, $f(u)$ and $g(u)$ are unknown universal scaling functions analytic at $u = 0$, and η and ν are the critical exponents From the data for these observables ρ_s and χ at various box sizes L and couplings J close to the critical value J_c, we can perform a combined fit to Eqs. (4.38) and (4.39). We approximate the functions $f(u)$ and $g(u)$ by a truncated Taylor series expansion up to a given order $n_{\max}$

$$f(u) = \sum_{n=0}^{n_{\max}} f_n u^n, \tag{4.40}$$

$$g(u) = \sum_{n=0}^{n_{\max}} g_n u^n. \tag{4.41}$$

The coefficients f_i, g_i become parameters to be fit. Since u is small close to the critical point, the Taylor series can be truncated to small values such as $n_{\max} = 2, 3, 4$. However, we do need to vary $n_{\max}$ empirically to find an optimal truncation. This procedure allows us to get a fairly accurate first estimate for the critical coupling J_c, the critical exponents ν, η, and the scaling functions $f(u)$ and $g(u)$.

However, this nonlinear fitting procedure (with $2n_{\max} + 5$ parameters) is somewhat opaque given its reliance on the correct range of L and J, good initial guesses for the parameters and optimal polynomial truncations for the functions $f(u)$ and $g(u)$. Hence, we perform a few additional steps to make sure that we are indeed in the scaling regime, and to identify the critical exponents more precisely.

Once we obtain a reasonably precise estimate for the critical point $J = J_c$ from the above fits, we perform another set of computations exactly at $J = J_c$ for various L. First, we look at the current-current susceptibility $\rho_s(0; L)$ at $J = J_c$, which according to Eq. (4.38), must simply behave as

$$\rho_s(0; L) = \frac{f(0)}{L}. \tag{4.42}$$

for $D = 3$ spacetime dimensions. We perform a single powerlaw fit to $\rho_s(0;L)L = f(0)L^{\alpha}$ to find $f(0)$ and the power α. If we are exactly at the critical point, the exponent must be $\alpha = 0$, within errors. So, we repeat this computation over a range of box sizes $L \in [L_{\min}, L_{\max}]$, until α becomes consistent with $\alpha = 0$ within errors. This gives us the scaling window $[L_{\min}, L_{\max}]$. As an example, the top plot in Fig. 4.3 shows this fit for the $O(6)$ qubit model.

Performing the computations at $J = J_c$ also allows for a clean extraction of the critical exponent η. We perform a power-law fit of the susceptibility $\chi(0;L)$ to the form

$$\chi(0;L) = g(0)L^{2-\eta}, \tag{4.43}$$

obtained by setting $u = 0$ in Eq. (4.39). This gives us our final value of the critical exponent η. For the $O(6)$ qubit model, the bottom plot in Fig. 4.3 shows the extraction of η at the critical point.

Now we need to find the critical exponent ν. For this, we go back and perform the combined fits of Eqs. (4.38) and (4.39) again. But this time we use the scaling window $L = [L_{\min}, L_{\max}]$ determined above. We also keep η, $f(0)$, and $g(0)$ fixed to the values obtained from the powerlaw fits at $J = J_c$ in Eqs. (4.42) and (4.43). This allows us to obtain a more controlled fit, and a more precise extraction of the critical exponent ν. This is the value for ν that we finally report. Additionally, we obtain the critical point J_c, again to make sure it is consistent with the value we chose in the previous step. This is an additional check of self-consistency of our fits. For the $O(6)$ qubit model, Fig. 4.4 shows these combined fits in the scaling window and the extraction of the critical exponent ν, the critical point J_c, and the universal scaling functions $f(u)$ and $g(u)$.

We have performed these calculations for the $O(N)$ qubit model with $N = 2, 4, 6, 8$. The complete fitting results for all these models are collected in Figs. 4.6 and 4.7. In the next section, we compare the results for the qubit models with

known results for the Wilson-Fisher fixed point in the literature.

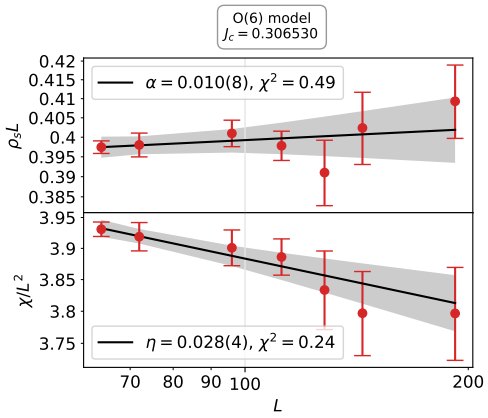

Figure 4.3: Critical scaling for the $O(6)$ qubit model at the critical point $J = J_c$. *Above:* We peform a powerlaw fit for winding-number susceptibility $\rho_s L = f(0)L^{\alpha}$ in a range of box sizes $[L_{\text{min}}, L_{\text{max}}]$ and extract the power α. If the box sizes are large enough, then we must have $\alpha = 0$ at the critical points. By choosing the window $[L_{\text{min}}, L_{\text{max}}]$ such that $\alpha = 0$ within $\sim 1\sigma$, we can make sure our subsequent fits are in the scaling regime. *Below:* We then fit the susceptibility to the form $\chi(0;L) = g(0)L^{2-\eta}$ to extract η. We can now use this value of η, as well as $f(0), g(0)$ as an input during the extraction of ν from the double fits, as demonstrated in Fig. 4.4.

4.5 Wilson-Fisher fixed point

In the previous sections, we computed critical properties of our $O(N)$ qubit model. In this section, we would like to argue that our model indeed lies in the $O(N)$ WF universality class by comparing the critical exponents with the known results for the $O(N)$ NLSM in the literature.

The critical properties of the 3d $O(N)$ NLSM have been studied thoroughly in the literature through several techniques. Numerically, precise results are available from MC and conformal bootstrap techniques. Analytically, even though the 3d $O(N)$ model is non-perturbative, several techniques have been developed to leverage a "hidden" small parameter and enable analytic control, such as the $1/N$ and ϵ expansions. In this section, we compile the best results

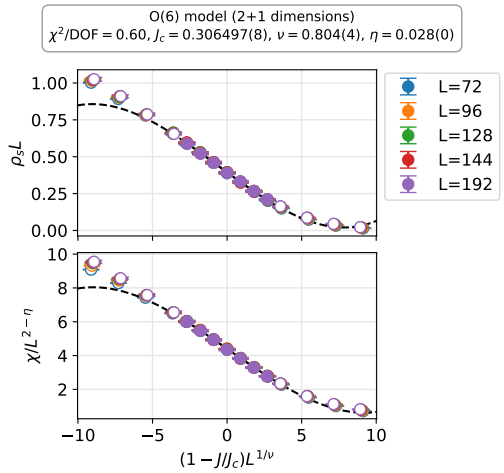

Figure 4.4: Scaling collapse for the $O(6)$ qubit model close to the critical point. The above plot shows the data for winding-number susceptibility ρ_s while the bottom plot shows the two–point function susceptibility χ. The circles show MC data for various L. The black dashed line shows a combined fit to both $\rho_s(J, L)$ and $\chi(J, L)$ for various J, L. The filled circles were used in the fit as the scaling window, while the open circles were not used in the fit. Yet, we find that the open circles all lie on the same curve, within small deviations expected at the edges from corrections to scaling, indicating that the scaling hypothesis is well satisfied in the fitting regime. In the final fits, the values of the critical exponent η as well as the y-intercepts $f(0)$, $g(0)$ were fixed by performing the fits shown in Fig. 4.3. For more details on the fitting procedure, see Section 4.4.4.

known to us from these techniques. We show this comparison in Fig. 4.5, where we perform a comparison across these methods for the critical exponents ν and η.

First, we consider the critical exponents for the $O(N)$ model in a large-N expansion, which is exact in the $N \to \infty$ limit. In the $1/N$ expansion, the critical exponent ν is known up to order N^{-2} and η up to order N^{-3} [49],

$$\nu = 1 - \frac{32}{3\pi^2}\frac{1}{N} + \left(\frac{3584}{27\pi^4} - \frac{32}{\pi^2}\right)\frac{1}{N^2} + O(N^{-3}), \quad \text{and} \tag{4.44}$$

$$\eta = \frac{\eta_1}{N} + \frac{\eta_2}{N^2} + \frac{\eta_3}{N^3} + O(N^{-4}), \tag{4.45}$$

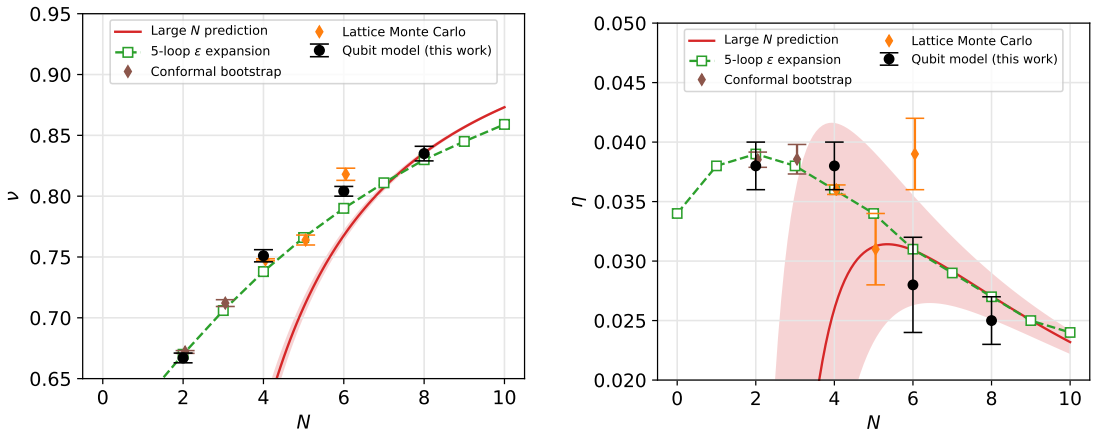

Figure 4.5: Comparison of the qubit $O(N)$ model against existing results in literature for the WF critical exponents ν, η. The black dots labeled "qubit model" are from this work. The green boxes for ε-expansion are from Ref. [50]. The large-N results [49] are shown as a solid red line, with the shaded band showing expected higher order $1/N$ contributions assuming they are of natural size. Finally, we show the best numerical results from lattice MC and conformal bootstrap as filled diamonds. The numbers for the critical exponents, along with the references, are listed in Table 4.2. We find excellent agreement with all the other techniques.

with

$$\eta_1 = \frac{8}{3\pi^2}, \quad \eta_2 = -\frac{8}{3}\eta_1^2, \quad \eta_3 = \eta_1^3\left[-\frac{797}{18} - \frac{61}{24}\pi^2 + \frac{27}{8}\psi''(1/2) + \frac{9}{2}\pi^2 \ln 2\right], \tag{4.46}$$

where $\psi(x) \equiv (d/d\ln x)\Gamma(x)$ is the logarithmic derivative of the Γ function. Ref. [49] gives the large-N expressions for the critical exponents η and γ. The critical exponent ν can be extracted from the scaling relation $\nu = \gamma/(2-\eta)$. We show the large-N results as a solid line in Fig. 4.5.

The next analytic technique we compare with is the ε expansion. The ε expansion is a divergent series, so several resummation methods have been employed in the literature. However, resummation techniques are uncontrolled and do not yield precise error estimates. Hence, the ε expansion results shown in Fig. 4.5 as green boxes do not have error estimates. The values shown are from Ref. [50], where the authors computed the critical exponents from a five-loop ε

Table 4.2: Comparison of the qubit model results with literature

	ν				η			
N	2	4	6	8	2	4	6	8
Qubit model	0.6670(40)	0.7510(50)	0.8040(40)	0.8350(60)	0.0380(20)	0.0380(20)	0.0280(40)	0.0250(20)
ϵ expansion	0.670	0.738	0.790	0.830	0.039	0.036	0.031	0.027
Large N	−0.010	0.612	0.768	0.836	−0.149	0.026	0.031	0.027
Numerical	0.6719(11)[b]	0.747 66(84)[c]	0.8180(50)[d]		0.038 52(64)[b]	0.036 00(40)[c]	0.0390(30)[d]	

[a] Monte Carlo [51]
[b] Conformal bootstrap [52]
[c] Monte Carlo [53]
[d] Monte Carlo [54]
[e] Fixed dimension expansion [55]

expansion and tabulated the results up to $N = 28$.

Finally, we show the numerical results available in the literature for various N [46]. These results are shown as filled diamonds in Fig. 4.5. In most of these cases (especially for $N \geq 4$), our results are almost as precise as the best results in the literature. It is encouraging that we are already able to achieve reasonably good precision with the qubit model and a simple finite-size scaling analysis. This suggests that better precision should be within reach if desired using the qubit model.

We consistently find that the critical exponent ν from the qubit model agrees very well with all the existing results up to $N = 8$. Unfortunately, the critical exponent η, being smaller, has larger error bars on this scale. It is harder to extract η to a high relative precision without a more sophisticated analysis, but we feel that is more suited for a follow-up work. We do find that the results from other techniques for η lie within 1σ of our computations.

Based on these comparisons, we see that the qubit $O(N)$ model seems to have a second-order critical point that lies in the $O(N)$ WF universality class.

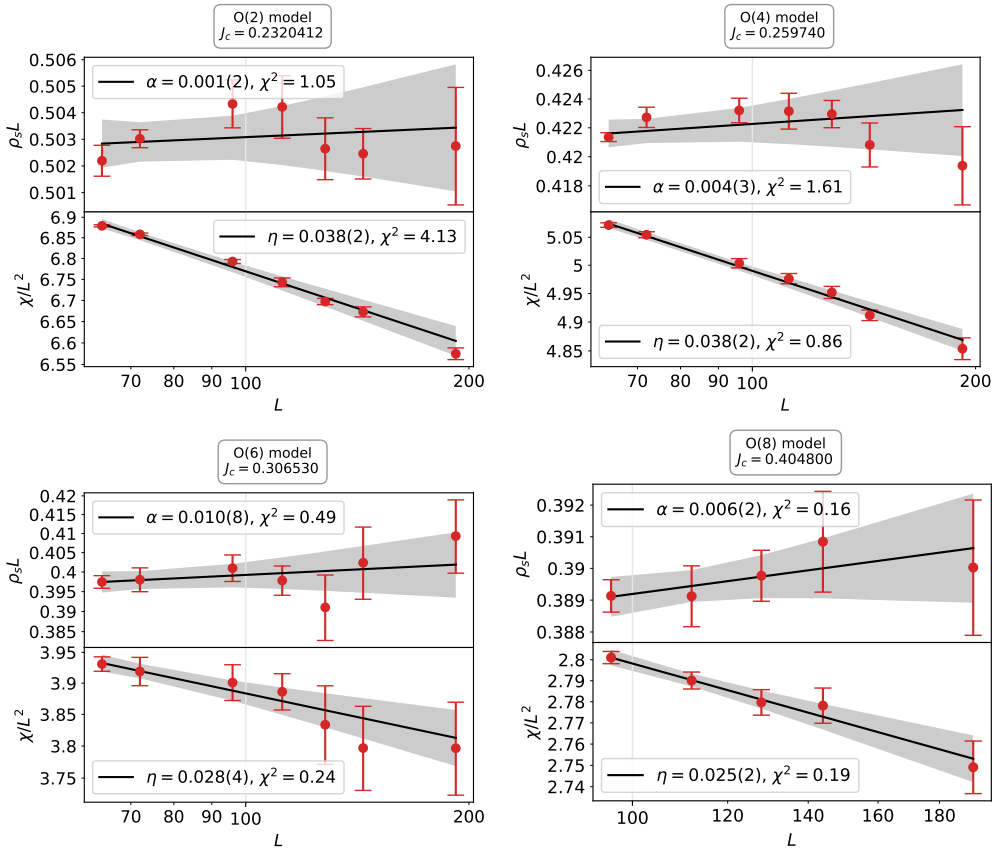

Figure 4.6: Critical scaling for $O(N)$ models with $N = 2, \ldots, 8$. We choose a range of box sizes L such that $\alpha = 0$ within errors. This is shown in the plots on the left for different N. We then fit susceptibility to the form $\chi(0;L) = g(0)L^{2-\eta}$ to extract η, as shown in the right plots. This procedure establishes the scaling window and also gives a clean extraction of η. We can now use this value of η.

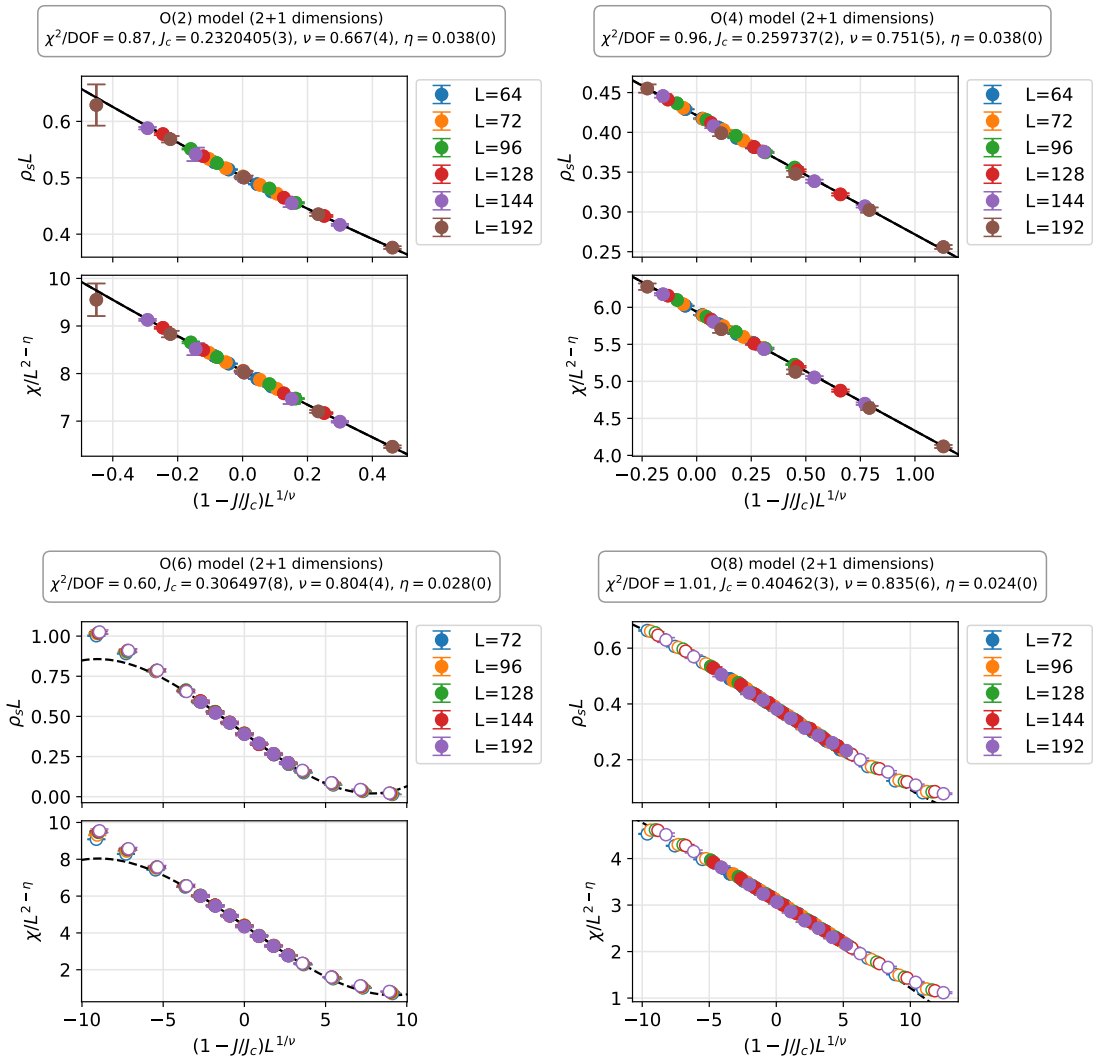

Figure 4.7: Critical scaling for $O(N)$ models with $N = 2, 4, 6, 8$. The results agree with the known Wilson-Fisher critical exponents within errors.

4.6 Discussion and conclusions

In this chapter, we developed a qubit regularization of the $O(N)$ NLSM for $D \geq 3$ spatial dimensions. We provided evidence that this model has a critical point in the $O(N)$ WF universality class. In particular, we computed the critical exponents ν, η for a range of $N = 2, 4, 6, 8$, and compared these with the available results in the literature for the WF fixed point from various other techniques such as the large-N and ϵ-expansion. The $O(N)$ NLSM in three spacetime dimensions is described by the WF fixed point, therefore our qubit model reproduces the physics of the $O(N)$ NLSM.

A major motivation of this work was to develop the idea of qubit regularization of QFTs, proposed in Ref. [45]. There, the authors constructed a qubit model for the $O(3)$ NLSM using two qubits per lattice site. In this work, we demonstrate the two-qubit $O(3)$ model of Ref. [45] can be generalized to an $O(N)$ model for arbitrary N, although with a larger Hilbert space ($N+1$ dimensional) at each lattice site.

A key appeal of such qubit models is their suitability for simulation on quantum computers. If the quantum critical point can be located precisely using classical lattice MC calculations, then it is guaranteed that the continuum QFT exists and can be studied while keeping the number of qubits per lattice site fixed, following Wilson's RG.

At least in the foreseeable NISQ-era, if the ideal of fault-tolerant quantum computers can be achieved, it will be extremely important to construct physically interesting models that use the available qubits parsimoniously, and yet reproduce the physics of a desired QFT. This is a very active program of research, and perhaps the most important ideas are yet to come.

While we had hoped to push our calculations for $N \geq 10$ as well, we encountered a somewhat puzzling phenemomen. We found that the higher N qubit models require larger volumes, which are limited by available computational

resources. This suggests that there may be a new scale in the problem that is controlled by N. It also looks like, up to the lattice sizes considered in this work, the $N = 10$ qubit model is not in the usual superfluid phase for large λ, as it is for large couplings λ in the $N \leq 8$ models. Whether this signals a new kind of phase transition, or is simply an artifact of smaller volumes, is not clear. It would be very interesting to systematically explore higher N qubit models. We leave this for a follow-up work.

An important direction not considered in the present work is an $O(3)$ qubit model in $(1 + 1)$ dimensions. This model is known to be asymptotically free and displays several other similarities with QCD. It would be extremely valuable to construct a qubit model for this case, since it will open up the possibility of constructing such models for other asymptotically free theories such as QCD. Whether this is possible with a finite number of qubits per lattice site seems to be a controversial issue in the literature. This would be very interesting to resolve in a future publication.

Chapter 5

$O(N)$ qubit models in the large charge sector

We use the $O(N)$ qubit model with lattice Monte Carlo methods to numerically compute conformal dimensions of operators in sectors of large $O(N)$ charges for the Wilson-Fisher (WF) conformal field theory (CFT). This allows us to connect with recent literature on an effective field theory approach to $O(N)$ WF CFT in large-charge sectors. In particular, we extract the low-energy constants in the large-charge effective field theory, and quantitatively test recent analytic predictions from a combined large-N and large-charge approach.

5.1 Introduction

In recent years, it has been realized that for some conformal field theories (CFTs) with some global symmetry group G, restricting to sectors of large global charges for G leads to interesting simplifications. In particular, we can exploit the pattern of symmetry breaking in these large-charge sectors, and write down an effective field theory (EFT) description of the fixed point, with the inverse charge density as the small parameter. With this EFT, we can make several predictions about the properties of the CFT as a power-series in inverse charge density.

This technique was recently used in the very interesting works of Refs. [25, 31, 26] to study the $O(N)$ nonlinear sigma model (NLSM) in 3 spacetime dimensions. As we discussed in Section 4.2, from the continuum point of view, the low-energy physics of the $O(N)$ NLSM is described by the Wilson-Fisher (WF) fixed point. The scale invariant theory describing this fixed point is indeed a CFT, and is usually referred to as the WF CFT.

In the above-mentioned works, the authors developed an EFT description of the WF CFT in sectors of large global $O(N)$ charges. They were able to compute several properties, such as the conformal dimensions of various operators, in the large-charge expansion.

However, the large-charge EFTs have unknown low-energy constants (LECs) at each order in the large-charge expansion. This is a limitation of the EFT approach. Typically, we might be able understand the qualitative features of a physical system using an EFT by exploiting the information of the symmetries and scale separation. However, a quantitative computation of physical observables requires the knowledge of the LEC, which cannot be computed from within the EFTs. Therefore, we need an extra ingredient to make quantitative predictions.

In such cases, lattice Monte Carlo (MC) computations can be used to provide the missing pieces for the EFT, provided that signal-to-noise ratio (SNR) problems can be controlled. We note that such an approach is quite general, also being used, for example, to make predictions about few-nucleon physics by combining EFTs of quantum chromodynamics (QCD) such as chiral perturbation theory or pionless EFT with lattice QCD computations.

Such a combined lattice MC and EFT approach was taken by the authors of Ref. [27] to study the $O(2)$ Wilson-Fisher fixed point in sectors of large global charge. They computed the conformal dimensions and extracted the LECs by fitting to the form predicted by the EFT. Surprisingly, they found that the large-charge expansion with just the leading three terms captures the behaviour of the conformal dimensions of charge-Q operators all the way down to $Q = 1$, suggesting that the higher order terms in the large-charge EFT are unnaturally small. However, at the moment the reason for this is not completely understood.

This strategy of combining lattice MC computations to extract the LECs of the large-charge EFT was then extended to the $O(4)$ Wilson-Fisher fixed point in Ref. [28]. The fit of the anomalous dimensions to the EFT prediction from only

the first three terms in the large-charge EFT predictions is again quite striking.

Recently, Ref. [31] combined the large-charge approach with a large-N expansion for the $O(N)$ WF CFT. This enabled them to to compute the LECs analytically in the large-N limit for the $O(N)$ Wilson-Fisher CFT. The authors compared the large-N predictions for the LECs to the available results for $N = 2$ and $N = 4$ and found reasonable agreement. It is natural to ask to whether the agreement with numerical results becomes better for larger N, as is the prediction. This is the main motivation for the present work.

In order for MC methods to be viable, it is important to have the SNR problems under control in the regime of interest. In fact, the traditional $O(4)$ lattice model (4.2) leads to a severe SNR problem in sectors of large global charge. To circumvent this issue, the authors of Ref. [28] used a *qubit* $O(4)$ model. A worm algorithm in the worldline formulation based on this qubit model alleviates the SNR problem in the traditional model, and enabled the computations of the conformal dimensions of the large-charge operators in the $O(4)$ Wilson-Fisher CFT.

In this work, our aim is to extend the strategy to the general case of $O(N)$ nonlinear sigma models. There are two major steps in extracting anomalous dimensions. The first step is to establish that our $O(N)$ qubit model has a quantum critical point that is indeed in the expected $O(N)$ Wilson-Fisher universality class, and to locate the critical coupling precisely. We did this for $N = 2, 4, 6, 8$ in the previous chapter.

Precisely identifying the critical point in the $O(N)$ qubit model, we can then proceed to the second step. To compute the conformal dimensions of the large charge operators in the $O(N)$ Wilson-Fisher CFT, we use the algorithm developed in Ref. [28], which is easily generalized to arbitrary N, to compute correlation functions in the presence of charged sources and sinks.

Since we also perform computations for $N = 2$ and $N = 4$, let us make a few

comments about the relationship of our work to the earlier works of Refs. [27, 28]. For the $O(2)$ Wilson-Fisher fixed point studied in Ref. [27], the authors used a traditional lattice model, which is quite different from the qubit model we use in this work. Our results are in perfect agreement with their results, and so the present work provides a nontrivial independent verification of the existing $O(2)$ results. On the other hand, the techniques and model of the present work are an extension of Ref. [28] for the $O(4)$ model. So in that case, we do expect our results to match it. However, as we will remark later, some details of the model are different, so it is indeed reassuring that our results are consistent with both these earlier works and provide a nontrivial independent check. The $N = 6, 8$ results in the large charge sector are new to the best of our knowledge.

5.2 The large charge expansion for $O(N)$ nonlinear sigma model

In this section, we review the large-charge expansion of $O(N)$ (recall that we use $2n = N$) nonlinear sigma model. We merely point out the aspects of the large-charge literature relevant for our work, and refer the interested reader to the original works [31, 25, 26] for further details.

We can classify fields in a CFT according to their representations under the conformal group. In particular, fields $\phi(x)$ with well-defined conformal transformation properties transform under scaling $x \to \Lambda x$, as

$$\phi(x) \to \phi'(x') = \Lambda^{-D_\phi} \phi(\Lambda x) \tag{5.1}$$

where D_ϕ is a real number called the *conformal dimension* of $\phi(x)$. Within a given representation of the conformal group, fields with the lowest conformal dimension are called *primary*. Invariance under conformal symmetry implies

that the 2-point functions of the primary fields $\phi(x)$ must behave as power-laws,

$$\langle \phi(x)\phi(y)\rangle = \frac{c}{|x-y|^{2D_\phi}}. \tag{5.2}$$

If the CFT has an additional symmetry G, then the fields can further be classified according to representations of G. We take G to be a compact Lie group. Let $h_1,\ldots,h_n$ be a basis for the Cartan subalgebra (CSA) of the Lie algebra of G. If we choose a basis for the fields such that all h_i $(i = 1,\ldots,n)$ act diagonally on the fields, then the set of simultaneous eigenvalues of $h_1,\ldots,h_n$ are called the *charges*:

$$\vec{q} = (q_1,\ldots,q_n). \tag{5.3}$$

In this work, we consider the $O(N)$ WF CFT and take $G = O(N)$ with $N = 2n$. The work of Refs. [25, 31, 26] shows that the conformal dimensions of leading primary operators in a fixed charge sector $\vec{q} = (q_1,\ldots,q_n)$, can be written as an expansion in inverse powers of the total charge $Q = \sum_{i=1}^{n} |q_i|$,

$$D(Q) = c_{3/2}Q^{3/2} + c_{1/2}Q^{1/2} + c_0 + O(Q^{-1/2}). \tag{5.4}$$

In this expression, $c_{3/2}$ and $c_{1/2}$ are unknown constants that depend on N, but c_0 is universal and predicted to be $c_0 = -0.0937\ldots$, independent of N.

Recently, the authors of Ref. [31] studied the $O(N)$ Wilson-Fisher fixed point in a combined large-charge and large-N limit. In this limit, they were able to analytically compute the coefficients $c_{3/2}$ and $c_{1/2}$,

$$c_{3/2} = \frac{2}{3}N^{-1/2}, \quad c_{1/2} = \frac{1}{6}N^{1/2} \tag{5.5}$$

in the regime $N \ll Q \ll N^2$ for large Q, N. The goal of this work is to perform lattice calculations for the $O(N)$ WF CFT and test the validity of Eqs. (5.4)

and (5.5).

5.3 Conformal dimensions from qubit lattice models

We are interested in the conformal dimensions of leading charge-Q primary operators ϕ_Q, which in a CFT can be measured by computing two-point correlators,

$$\langle \phi_Q(x)\phi_{-Q}(y)\rangle = \frac{c}{|x-y|^{2D(Q)}}, \tag{5.6}$$

where $D(Q)$ is the conformal dimension of ϕ_Q, and c is an arbitrary normalization that can be chosen to be $c = 1$.

In the previous chapter, we developed an $O(N)$ qubit model and gave numerical evidence to support that it has a second-order critical point in the $O(N)$ WF universality class. Given any critical lattice Hamiltonian H in the universality class of the $O(N)$ WF fixed point, the arguments of Wilson's renormalization group (RG) (Chapter 2) show that we may access any correlation function in the WF CFT by computing appropriate correlation functions in the lattice model at criticality in the scaling regime. Therefore, we can use the $O(N)$ qubit model to compute correlation functions of charge-Q operators.

However, the qubit models have a finite dimensional Hilbert space at each lattice site. At any given site, the local Hilbert space of the qubit model can only hold one of the states with well-defined charges $\vec{q}_{\pm 1}, \cdots, \vec{q}_{\pm n}$, where

$$\vec{q}_{\pm 1} = (\pm 1, 0, \ldots, 0) \tag{5.7}$$

$$\vec{q}_{\pm 2} = (0, \pm 1, \ldots, 0) \tag{5.8}$$

$$\vdots \tag{5.9}$$

$$\vec{q}_{\pm n} = (0, 0, \ldots, \pm 1). \tag{5.10}$$

(The choice of basis and notation was also described in Section 4.3.) Therefore, the qubit model does not allow arbitrarily high charges at any given lattice site. For example, we cannot create a local state with charge $\vec{Q} = (Q, 0, \ldots, 0)$ with $|Q| > 1$.

However, we can compute the correlators of leading charge-Q operators in a qubit model by spreading the charges in a small region and appealing to scaling. This is because the long distance behaviour of the correlation functions of a product of nearby local lattice operators can be expressed in terms of the scaling operators defined at the fixed point. For example, let us assume that $\phi^L(x)$ is a local lattice operator that creates a state of charge $\vec{q}_1 = (1, 0, \ldots, 0)$. Let $x_1, \ldots, x_Q$ be spacetime points that all lie within a small distance a_Q (of the order of lattice scale) of some point x. We define the product of operators

$$\Phi^L_{\vec{Q}}(x) = \prod_{i=1}^{Q} \phi^L(x_i). \tag{5.11}$$

Since the local operators on the right hand side have well-defined charges $\vec{q}_1$, the operator $\phi^L(x)$ has the charge $\vec{Q} = Q\vec{q}_1 = (Q, 0, \ldots, 0)$.

The ideas of Wilon's RG (see, for example, Ref. [34, Sec. 3.8]) predict that the long-distance behaviour of the 2-point function of $\Phi^L(x)$ can be expressed in terms of the scaling operators in the CFT

$$\langle \Phi^L_{\vec{Q}}(x) \Phi^L_{-\vec{Q}}(y) \rangle = \sum_{ij} A_{ij} \langle \phi_i(x) \phi'_j(y) \rangle \quad \text{for} \quad |x - y| \gg a_Q, \tag{5.12}$$

where the sum on the right hand side is over all scaling operators ϕ_i, ϕ'_j which have the same symmetry properties as the lattice operators $\Phi^L_{\vec{Q}}(x), \Phi^L_{-\vec{Q}}$, respectively, and A_{ij} are some non-universal constants. In particular, the scaling operators that contribute must have charges $\vec{Q}$ and $-\vec{Q}$. Since the scaling operators in a CFT are power-laws with the exponent related to the conformal dimensions, the leading order behaviour of the above equation comes from the

leading (most-relevant) charge-Q operators and is therefore given by

$$\langle \Phi^L_{\vec{Q}}(x)\Phi^L_{-\vec{Q}}(y)\rangle = \frac{c_L}{|x-y|^{2D(Q)}} + \begin{pmatrix}\text{terms that}\\ \text{decay faster}\end{pmatrix} \quad \text{for} \quad |x-y| \gg a_Q, \tag{5.13}$$

where c_L is some non-universal constant that depends on the details of the lattice operators. Therefore, we can measure conformal dimensions $D(Q)$ by computing the correlation function of the type given in Eq. (5.13). We show this schematically in Fig. 5.1. Now, our task is to develop a MC method that can do so efficiently.

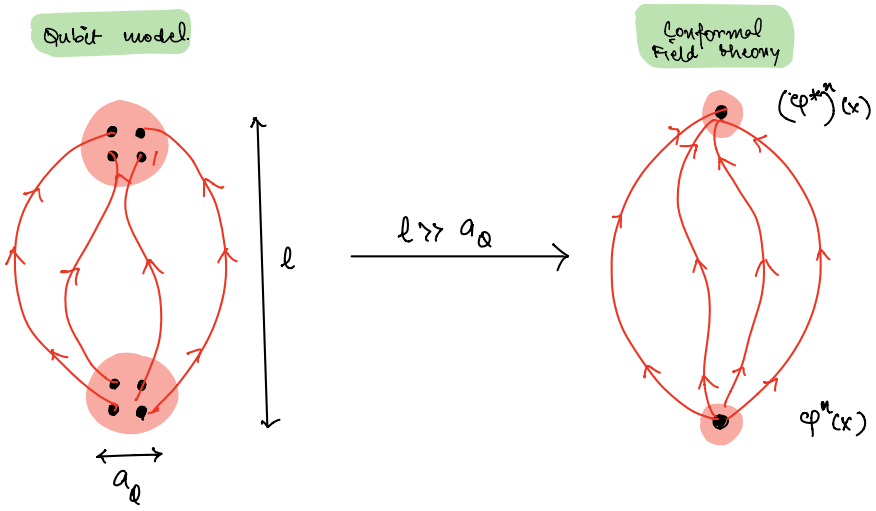

Figure 5.1: Using the qubit model to compute conformal dimensions in the CFT

5.4 Lattice Monte Carlo

One way to numerically measure the conformal dimensions of the leading charge-Q operators is to directly measure the correlator given in Eq. (5.13), and use finite-size scaling arguments. We can put the system in a finite box of linear size L and fix the separation between the sources and sinks to be some fraction $\alpha < 1$ of the box size $|x-y| = \alpha L$. Finite-size scaling arguments show that the

L-dependence of the correlator must be

$$\langle \Phi^L_{-\vec{Q}}(x)\, \Phi^L_{\vec{Q}}(y)\rangle \propto L^{-D(Q)}, \quad \text{for } |x-y| = \alpha L, \text{ and } \alpha L \gg a_Q, \tag{5.14}$$

where L is the linear size of the system, and $D(Q)$ is the conformal dimension of the leading charge-Q operator.

In principle, any lattice model in the $O(N)$ WF universality class can be used to compute the correlators. For example, we might try to use the traditional $O(N)$ lattice model (given by Eq. (4.2)). However, such a direct measurement of this correlator using the traditional $O(N)$ lattice model suffers from a severe SNR problem [28].

To circumvent the SNR problem with the traditional model, the authors of Ref. [28] developed a method to reliably extract the conformal dimensions for the $O(4)$ WF CFT by computing the difference

$$\Delta(Q) = D(Q+1) - D(Q). \tag{5.15}$$

using a qubit $O(4)$ model in the worldline formulation with worm algorithms. In this work, we generalize the model and techniques of Ref. [28] to the $O(N)$ model.

5.4.1 Worldine formulation

We begin by recalling the partition function of the worldline $O(2n)$ qubit model Eq. (4.30),

$$Z_Q = \sum_{\mathcal{C}} W[\mathcal{C}], \tag{5.16}$$

where the sum is over oriented, closed, worldline configurations of n colors. The weights of the configuration $W[\mathcal{C}]$ are given by the product of local weights

of each bonds. We choose the temporal and spatial bonds to have the same weight, which gives a spacetime lattice model with manifest symmetry between space and time. If we denote the weight of each bond by J, then this model has a second-order critical point $J = J_c$ for $N = 2, 4, 6, 8$. This critical point was precisely located in Section 4.5.

To compute the correlators given in Eq. (5.14), we would like to develop a worm algorithm which works in sectors with fixed charge sources and sinks. We define a partition function in the charge-Q sector,

$$Z_Q = \sum_{\mathcal{C}_Q} W[\mathcal{C}_Q], \tag{5.17}$$

where the sum is now over worldline configurations $\mathcal{C}_Q$ that have Q sources at the time slice $t = 0$ in a small region around $\vec{x} = 0$, and Q sinks of the same type at the time slice $t = L/2$ in an identical configuration in space.

As mentioned before, if the linear size of the spatial region occupied by sources and sinks is a_Q, then the long-distance physics of the CFT in the charge-Q sector emerges at length scales $l \gg a_Q$. Therefore, we would like to keep a_Q as small as possible, although the exact placement of the charges inside this region does not matter. We describe our choice of the charge placement in Fig. 5.2, where the numbers show the order in which the charges are placed as we increase the total charge Q. We do not place a charge at the center, since we use that for the 'measurement' update, as described below in Section 5.4.3. An illustration of a configuration that contributes to Z_Q is shown in Fig. 5.3.

To describe an algorithm that can measure $\Delta(Q)$, we also define a partition function in the $(Q+1)$ sector. Let $Z_{Q+1}^{(\vec{x},t)}$ be a partition function with $Q+1$ sources and sinks defined as follows. We take $Z_{Q+1}^{(\vec{x},t)}$ to be the sum over configurations where the first Q sources and sinks are placed exactly as Z_Q, but we have an additional source at the origin $(\vec{x}, t) = (\vec{0}, 0)$, and a sink at an arbitrary spacetime site $(\vec{x}, t)$. Now, we define an observable which is the ratio of partition functions

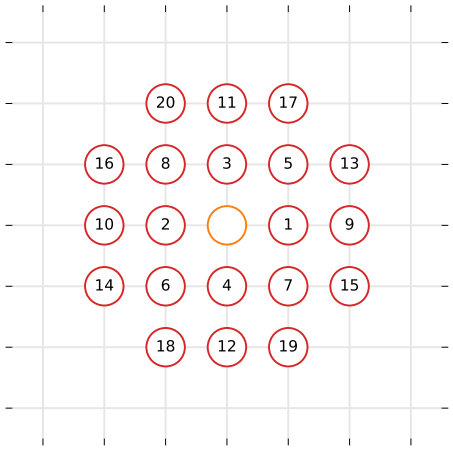

Figure 5.2: Placement of the 'red' sources at the $t = 0$ and $t = L/2$ temporal slices. The numbers show the order in which the sources are placed as we increase the total charge Q. We choose the configuration to ensure that the spread (linear size a_Q) is as small as possible. The central site $\vec{x} = 0$ is kept empty for the *measurement* update, as described in Section 5.4.3.

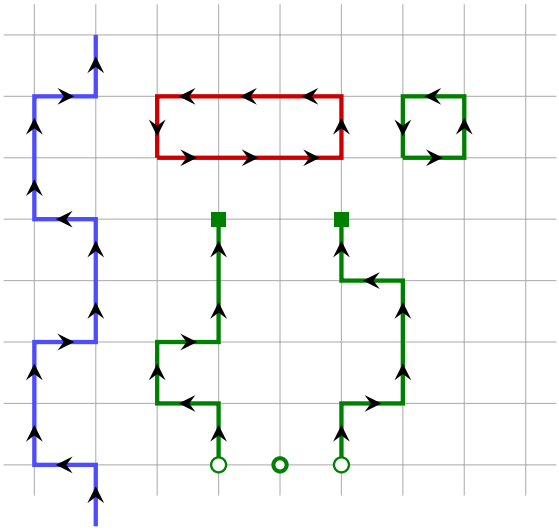

Figure 5.3: A typical worldline configuration for the $O(6)$ model with three colors, and two green sources and sinks. The open circles indicate sources, and the filled squares indicate sinks. The source site at the center (thick open circle) is used in the measurement update, as described in the text.

in the charge-$(Q+1)$ and charge-Q sectors,

$$R_Q(L) \equiv \frac{Z_{Q+1}^{(\vec{0},L/2)}(L)}{Z_Q(L)}. \tag{5.18}$$

The discussion leading up to Eq. (5.14) also implies that

$$\frac{Z_{Q+1}^{(\vec{0},L/2)}}{Z_0} \propto \langle \phi_{Q+1}^\dagger(\vec{0}, L/2)\, \phi_{Q+1}(\vec{0}, 0)\rangle + \cdots, \quad \text{and} \tag{5.19}$$

$$\frac{Z_Q}{Z_0} \propto \langle \phi_Q^\dagger(\vec{0}, L/2)\, \phi_Q(\vec{0}, 0)\rangle + \cdots. \tag{5.20}$$

Therefore, the ratio R_Q must fall off as a powerlaw with the exponent $\Delta(Q) = D(Q+1) - D(Q)$,

$$R_Q(L) = cL^{-2\Delta(Q)} + (\text{higher order terms}), \tag{5.21}$$

where c is a non-universal constant. Now we can develop a worm algorithm to measure the observable $R_Q(L)$. There are two components to the worm algorithm in this work. The first is to generate configurations in Z_Q, and the second is to measure the observable R_Q defined in Eq. (5.18). We show the structure of the algorithm schematically in Fig. 5.4.

Note that, for simplicity, we have fixed the outgoing bonds at sources and the incoming bonds at the sinks. Also, this model does not allow loops to be turn back onto themselves. In this respect, this model is different from the one considered in Ref. [28] for the $O(4)$ model. Such details are not expected to matter at criticality, and indeed we are able to verify and reproduce the results of Ref. [28] for the $O(4)$ model, which is reassuring.

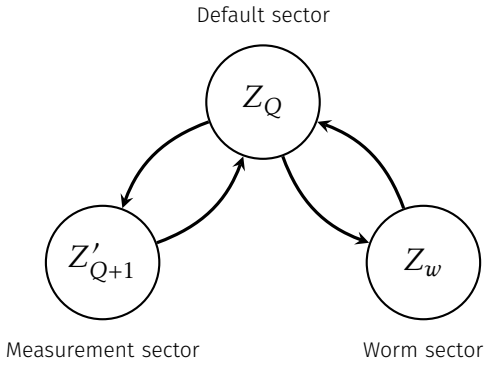

Figure 5.4: Worm algorithm for the extraction of conformal dimensions.

5.4.2 Worm algorithm: sampling Z_Q

Fortunately, configurations in Z_Q can be updated by using a simple extension of the worm algorithm that we described in Section 4.4.2. The only difference from the older worm algorithm is the existence of fixed sources and sinks in the configurations. We can easily accommodate this by slightly modifying the local updates listed Section 4.4.2 such that if the worm head proposes a move that would modify the local configuration corresponding to a fixed source or a sink, then we just reject that proposal. This allows us to update configurations while keeping the source and sink configurations intact. In all other respects, the algorithm in the worm sector behaves identically to Section 4.4.2.

5.4.3 Worm algorithm: measuring the conformal dimensions

To measure the observable $R_Q(L)$, we define a new partition function $\overline{Z}_Q$

$$\overline{Z}_Q = Z_Q + \sum_{(x,t)} Z_{Q+1}^{(x,t)} \tag{5.22}$$

where the sum is over all spacetime sites (x, t) of the lattice.

The advantage of this construction is that again we can use a specialized worm algorithm to sample configurations in the partition function $\overline{Z}_Q$. To do so, we begin the worm update for this sector by introducing a worm head and tail at

the site $(0,0)$, which was left empty for placement of configurations in Z_Q (see Fig. 5.2). Now, as the worm head moves, the algorithm samples configurations in $\sum_x Z^{(x)}_{Q+1}$. Whenever the worm head hits the site $(\vec{x},t)=(0,L/2)$, we count it as a configuration in $Z^{(0,L/2)}_{Q+1}$. Let the number of such configurations encountered within the ith measurement update be given by r_i. Then the average value of the observable r gives us exactly R_Q:

$$\left(\frac{r_1+\cdots+r_{N_Q}}{N_Q}\right)\xrightarrow{N_Q\to\infty}\frac{Z^{(0,L/2)}_{Q+1}}{Z_Q}=R_Q, \tag{5.23}$$

where N_Q is the total number of configurations generated in Z_Q.

5.5 Results

In Fig. 5.5, we show the power law fits for $N=2,4,6,8$ for small charges for illustration. We perform these fits up to $Q=10$. The exponent in each of these fits gives $\Delta(Q)$ and the conformal dimension $D(Q)$ is then computed using

$$D(Q)=\Delta(Q)+\Delta(Q-1)+\cdots+\Delta(0). \tag{5.24}$$

With the sources, there is an independent way of computing the critical exponent η that provides a self-consistency check.

Having extracted the conformal dimensions, we can now extract LECs in the large-charge EFT using the predicted form in Eq. (5.4). We show the fits in Figure 5.6, where we plot $D(Q)/Q^{3/2}$ as a function of Q. For large Q, Eq. (5.4) predicts that this must saturate to the value $c_{3/2}$, which can thus be extracted quite precisely. However, the subleading LEC $c_{1/2}$ is harder to extract.

Finally, in Fig. 5.7, we show the comparison with large-charge and large-N analytic predictions. We find that the analytic large-N prediction for the leading coupling is quite impressive, even at $N=6$. The prediction for the

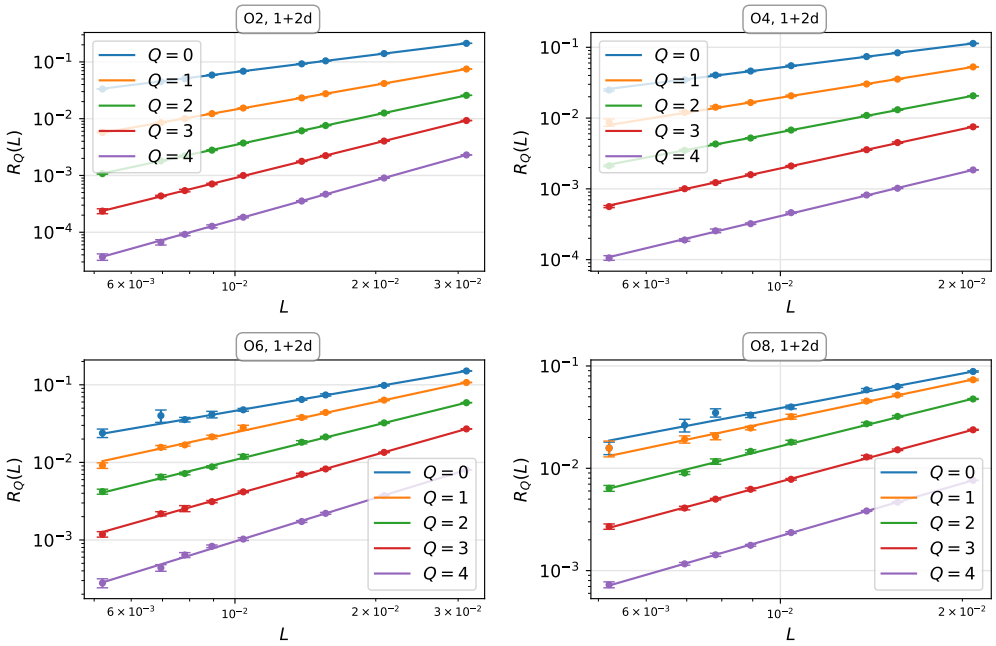

Figure 5.5: Extraction of the conformal dimensions for charged operators for $Q = 0, \cdots, 4$ to illustrate the quality of the fits.

subleading coupling $c_{1/2}$ also is well within the errors for $N = 6, 8$, although the errors are significantly larger as well. Even so, the large-N prediction that the leading coupling $c_{3/2}$ decreases with higher N, while the subleading coupling $c_{1/2}$ increases with N is unmistakably confirmed using the lattice calculations.

5.6 Conclusions

The motivation of this work was to push a combined lattice MC and large-charge EFT approach forward, and develop techniques for the $O(N)$ nonlinear model, extending the previous work in this spirit (for $N = 2, 4$) [27, 28], and to test the recent analytic predictions of Ref. [31], where the authors computed the LECs $c_{3/2}$ and $c_{1/2}$ from a combined large-charge and large-N limit. In this work, by using the qubit $O(N)$ model in the worldline formulation with an efficient worm algorithm, we could compute the conformal dimensions of large-charge operators up to $Q = 10$ for $N = 2, 4, 6, 8$. While we hoped to push this qubit model for $N \geq 10$ as well, we found that higher N qubit models seem to require

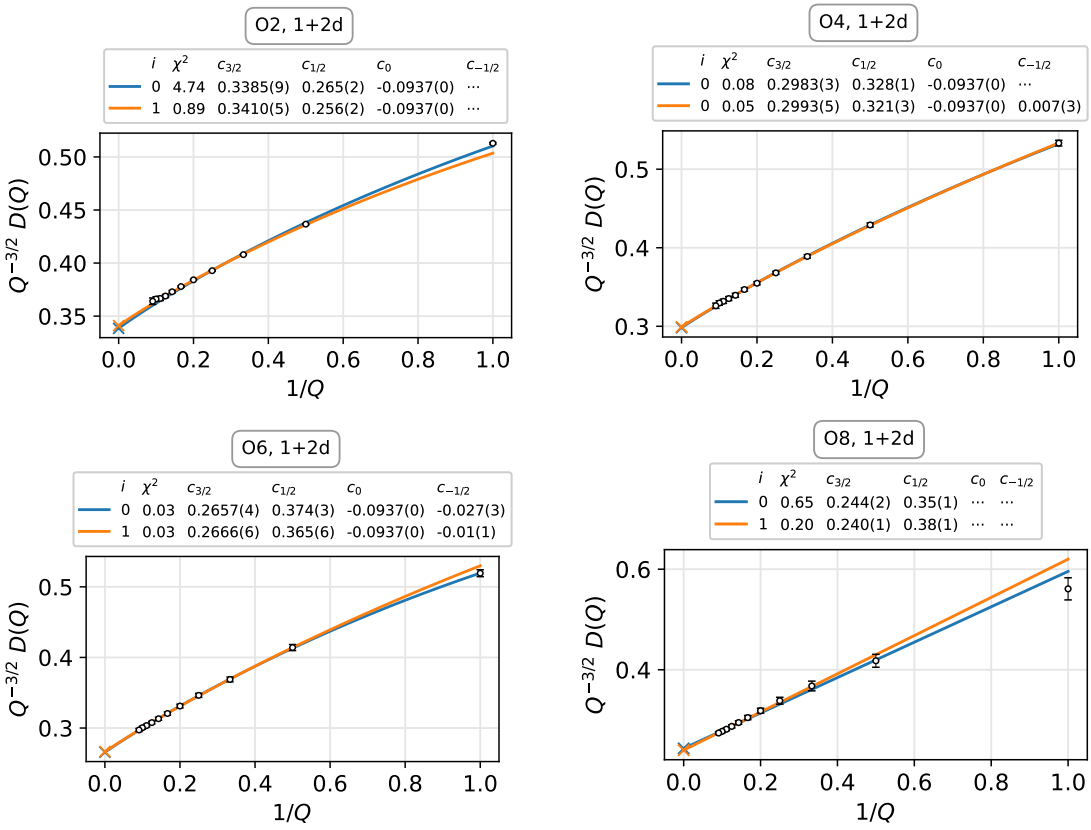

Figure 5.6: Extraction of the large-charge EFT coefficients from $Q = 1, \cdots, 20$.

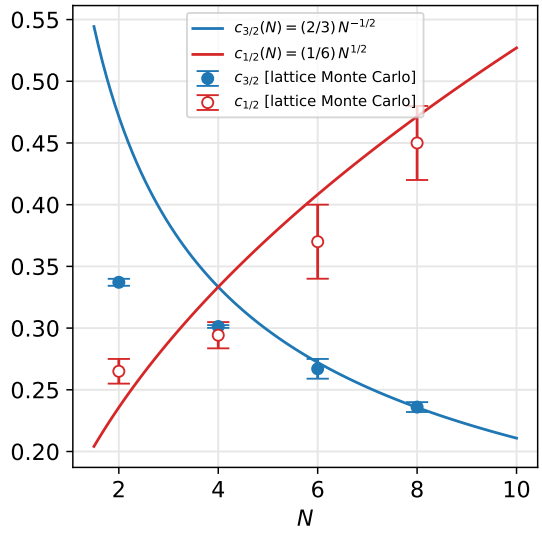

Figure 5.7: Comparison with the combined large-charge and large-N predictions of Ref. [31]. We find that the $c_{3/2}$ prediction is in excellent agreement with MC for $N \geq 6$. However, the subleading coefficient $c_{1/2}$, while within errors, seems to be in slight tension.

larger volumes to achieve criticality, which is limited by computational resources. It would be interesting to systematically explore this.

We fitted the conformal dimensions to the form predicted by the EFT and extracted the LECs directly. We find that the leading coupling $c_{3/2}$ has extremely good agreement with the large-N prediction already at $N = 8$. However, the extraction of the subleading coupling $c_{1/2}$ is less precise. So while it is harder to say how well the large-N predictions work for the subleading coupling, they seem to be consistent within the precision achieved in this study. It is amusing to note that the authors of Ref. [31] note a small "puzzle" about the product of couplings $c_{3/2}c_{1/2}$ that could be resolved with lattice MC computations provided we can reduce the errors on $c_{1/2}$. But it seems this will have to be addressed in a future publication.

Another interesting feature of the large-charge EFT is that the coupling c_0 of the Q^0 term in the large-charge expansion for $D(Q)$ is analytically predicted to be universal with the value $c_0 = -0.0937\ldots$, independent of N. It would be very interesting to extract this coupling directly from a lattice MC computation. However, since this is a next-to-next-to-leading-order coupling, the precision required to extract it confidently seems beyond the reach of the current method. A different way should be devised for this.

In Ref. [27], the authors also provided predictions for the subleading representations for the $O(4)$ model as well. Our approach of using qubit models with worm algorithms can be extended to cover such cases as well, and the results of that will be published elsewhere.

Chapter 6

Few-body physics of contact interactions

We study a system of two species of non-relativistic fermions with delta-function interactions using a worm algorithm in a worldline formulation. In one spatial dimension, we find that the worm algorithm works extremely well across a wide range of mass-imbalances, interaction strengths and particle numbers. The results from the worm algorithm uncover issues with a recent Complex-Langevin approach to such systems. Our technique shows promise for application to the, much harder, case of three-dimensional systems.

6.1 Introduction

Theories of particles interacting with short-ranged contact interactions frequently arise as EFTs of strongly coupled physical systems. In nuclear physics, pionless EFT [56] has been successfully used to study systems in the few-nucleon sector. They are being explored in astroparticle physics to predict universal properties of dark matter candidates such as axions [57] and to look for signatures of bound states of dark matter [58, 59]. In condensed matter physics, the unitary Fermi gas offers an example of a system of theoretical and experimental interest [60]. Such models have also extensively been used to describe electrons in metals [61, 62].

Most of the applications in particle and astroparticle physics of such EFTs focus on the few-body regime. However, even in this regime, analytic calculations become intractable as the number of particles increases, except in cases with extra symmetries [63, 64]. The applicability of perturbation theory is limited in many cases of interest. For example, in nuclear physics, we are interested

in bound states of nuclei, which are inherently non-perturbative systems. We perform analytic computations in the two-body sector (such as the deuteron), and even three-body sectors (such as helium-3, triton) to some degree. Beyond that however, we must supplement the EFT calculations with non-perturbative numerical techniques.

Lattice MC methods offer a powerful nonperturbative method to compute obsvervables in such systems, provided that the sign problem can be controlled. However, most state-of-the-art studies are based on auxiliary field quantum Monte Carlo (AFQMC) methods [65, 66, 67, 68, 69], which suffers from sign problems for repulsive interactions in many cases. It is desirable to look for alternative formulations and algorithms that might solve the sign problem, at least in the few-body sectors.

An excellent testing ground for new techniques is offered by systems in one spatial dimension. Recently, there has been tremendous progress in experimental techniques to confine ultracold gases in optical traps [70], which has made it possible to study one-dimensional systems experimentally.

Motivated by this, we study a system of two species of mass-imbalanced fermions in one spatial dimensions with a delta-function interaction, given by the continuum Hamiltonian

$$H = \int dx \left(- \sum_{\sigma=\uparrow,\downarrow} \frac{1}{2m_\sigma} \psi_\sigma^\dagger \, \partial_x^2 \psi_\sigma + g \; \psi_\uparrow^\dagger \psi_\uparrow \, \psi_\downarrow^\dagger \psi_\downarrow \right). \tag{6.1}$$

This is typically the leading-order Hamiltonian in the contact EFTs mentioned above. Recently, the authors of Ref. [32] used the Complex Langevin (CL) approach for this system to avoid the sign problem for repulsive interactions.

However, in one spatial dimension, the sign problem can also be solved using a worldline formulation [71, 72] under certain conditions. Motivated by this, we construct a general worldline approach to study the physics of hard-core bosons in the few-body sector in arbitrary dimensions. Since in this approach

fermions effectively become hard-core bosons up to boundary effects, we can use this method to study fermions as well.

Interestingly, we find that our worm algorithm results disagree with the CL results of Ref. [32] for stronger repulsive couplings. To resolve this discrepancy, we compare with perturbation theory and exact solutions from Bethe ansatz, when available. We find that the other techniques confirm the results of the worm algorithm, and the 'flattening' of the ground state energy as a function of the coupling observed by Ref. [32] is an artifact of the CL method.

This chapter is organized as follows. In Section 6.2 we discuss the lattice Hamiltonian formulation of two species of hard-core bosons with a contact interaction. In Section 6.3, we construct the worldline formulation of the problem on a space-time lattice and provide details of our worm algorithm in Section 6.4. In Section 6.5, we discuss how we can study fermions by measuring the fermionic permutation sign. In Section 6.6, we present our results for fermions in one spatial dimension and consider two cases: the mass-balanced case and the mass-imbalanced case. In the mass-balanced case, we show that our results are in agreement with the exact results obtained using the Bethe ansatz. We also show that in both cases the flattening of the ground state-energy observed in the CL calculations is absent in our approach.

This chapter is based on work published in Refs. [73, 74].

6.2 The continuum model and a lattice discretization

In this section, we describe a simple continuum four-fermion Hamiltonian and motivate a lattice model from it. Instead of fermions, however, we define our lattice model in terms of *hard-core* bosons, which obey the Pauli exclusion principle at each lattice site, but have bosonic statistics. Such objects are well-

defined on the lattice. Formulating the problem in terms of hard-core bosons will be useful to isolate the sign problem in a worldline formulation. In fact, we will see that in $d = 1$ spatial dimensions, rewriting the original fermionic Hamiltonian in such a way solves the sign problem for many cases of interest.

Let ψ_σ be a non-relativistic fermionic field of 'species' σ, say $\sigma = \uparrow$ (spin up) or $\sigma = \downarrow$ (spin down), and mass m_σ. In the continuum, we write down a Hamiltonian with a two-body delta-function interaction between the two species,

$$H_{\mathrm{c}} = -\sum_{\sigma=\uparrow,\downarrow} \frac{1}{2m_\sigma} \int dx\ \psi_\sigma^\dagger(x)\left(\frac{d^2}{dx^2}\right)\psi_\sigma(x) \tag{6.2}$$

$$H_{\mathrm{int}} = g \int dx\ \psi_\uparrow^\dagger(x)\psi_\uparrow(x)\ \psi_\downarrow^\dagger(x)\psi_\downarrow(x), \tag{6.3}$$

in $\hbar = 1$ units.

We would like to study a lattice discretization of the above Hamiltonian (6.3). To do so, we consider a d-dimensional spatial lattice of extent L (in lattice units) in each direction. We define *bosonic* creation and annihilation operators $c_{i,\sigma}^\dagger, c_{i,\sigma}$ for bosons of species σ at site i. The lattice Hamiltonian is

$$H = -\sum_{i,\hat{\alpha},\sigma} t_\sigma\ (c_{i,\sigma}^\dagger c_{i+\hat{\alpha},\sigma}\ + c_{i+\hat{\alpha},\sigma}^\dagger c_{i,\sigma} - 2c_{i,\sigma}^\dagger c_{i,\sigma}) + \frac{U}{a^d}\ \sum_i N_{i,\uparrow}N_{i,\downarrow}, \tag{6.4}$$

where the index i runs over all sites in the lattice, and $\hat{\alpha}$ unit vectors in each direction. We also define particle number operators at each site as $N_{i,\sigma} = c_{i,\sigma}^\dagger c_{i,\sigma}$.

Since a naive continuum limit of the first term (two-fermion operators) gives the kinetic term in Eq. (6.3), we identify the hopping parameter t_σ as being related to the mass m_σ of the particles,

$$t_\sigma = 1/(2m_\sigma a^2), \tag{6.5}$$

where a is the lattice spacing. The coupling U determines the interaction strength.

Our goal in this work is to compute the ground-state energy $E^0_{N_\uparrow,N_\downarrow}$ of the Hamiltonian in the subspace with particle numbers $N_\uparrow$ and $N_\downarrow$. We will do this by computing the energy

$$\langle E\rangle = \frac{1}{Z_\mu}\ \mathrm{Tr}\Big(\ H\ e^{-\beta H_\mu}\Big) \tag{6.6}$$

at very low temperature ($\beta \to \infty$). In the above, we have defined a modified lattice Hamiltonian,

$$H_\mu = H - \sum_{i,\sigma} \mu_\sigma N_{\sigma,i}, \tag{6.7}$$

with chemical potentials μ_σ for the two particle species, and the partition function

$$Z_\mu = \mathrm{Tr}\Big(e^{-\beta H_\mu}\Big) \tag{6.8}$$

to define the expectation value. We can see that if we compute the trace in a fixed particle-number sector, the chemical potential drops in the expectation value and we get $\langle E\rangle = E^0_{N_\uparrow,N_\downarrow}$ in the $\beta \to \infty$ limit. Therefore, we must develop a technique to compute $\langle E\rangle$ for large β.

6.3 Worldline formulation

The construction of a worldline representation for a general nearest-neighbor Hamiltonian is described in 3.2. We split the Hamiltonian as $H_\mu = H^{(1)} + H^{(2)}$, a sum of a diagonal term (in the occupation number basis)and a hopping term,

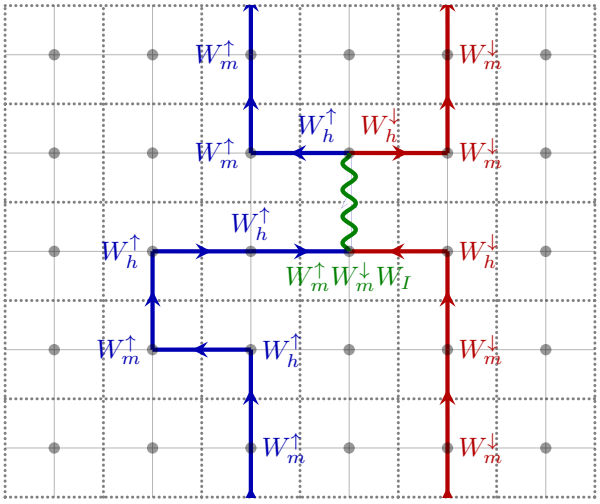

Figure 6.1: An illustration of a worldline configuration $\mathcal{C}$ with $N_\uparrow = 1$ and $N_\downarrow = 1$. The dots represent space-time lattice sites and the bold solid lines show the worldlines of the two particles. The interaction between the particles is shown as a wiggly temporal bond. The Boltzmann weights associated with lattice sites containing particles are also shown. (Figure reproduced from Ref. [74].)

where

$$H^{(1)} = \sum_{i,\sigma} \Big(2dt_\sigma - \mu_\sigma \Big) N_{\sigma,i} + U N_{\uparrow,i} N_{\downarrow,i}, \tag{6.9}$$

$$H^{(2)} = -\sum_{i,\hat{\alpha},\sigma} t_\sigma (c^\dagger_{i,\sigma} c_{i+\hat{\alpha},\sigma} + c^\dagger_{i+\hat{\alpha},\sigma} c_{i,\sigma}). \tag{6.10}$$

Following the steps in the construction described in Chapter 3 and Section 4.4.1, we end up with a rewriting of the partition function as a sum over worldline configurations,

$$Z_\mu = \sum_{\mathcal{C}} \Omega(\mathcal{C}), \tag{6.11}$$

where $\Omega(\mathcal{C})$ is the weight of each worldline configuration $\mathcal{C}$.

We show an illustration of a typical configuration in Fig. 6.1 on a $1+1$ dimensional spacetime lattice. Each configuration consists of closed worldline loops of two types, corresponding to the two species of particles. We represent them as red and blue worldlines. Worldlines of a given type cannot intersect

themselves, since that would violate the hardcore constraint. Therefore, we imagine that worldlines of different colors live on different layers of the lattice. On a given layer, all possible non intersecting (possibly disconnected) closed worldline spacetime loops are allowed.

To compute the weight $\Omega(\mathcal{C})$ of a configuration $\mathcal{C}$, we first define *local* weights $W^{(i,t)}(\mathcal{C})$ at each lattice site (i,t). The weight of the configuration is the product of these local weights at each lattice site,

$$\Omega(\mathcal{C}) = \prod_{i,t} W^{(i,t)}(\mathcal{C}). \tag{6.12}$$

The local weights $W^{(i,t)}$ depend on the worldline configuration at the site (i,t). The allowed configurations at a site for each particle species are shown in Fig. 6.2. If there is no worldline passing through a site, we define the weight of the site

$$W_e^\sigma = 1. \tag{6.13}$$

If a worldline passes through a site, we define the weight of the site to depend only on the outgoing bond, that is, the direction in which the particle leaves that site. If the particle leaves in the temporal direction, we assign a weight

$$W_m^\sigma = \exp\Big(-\varepsilon(2dt_\sigma - \mu_\sigma)\Big). \tag{6.14}$$

If, however, the particles hops to a neighboring spatial site, we assign a weight

$$W_h^\sigma = t_\sigma \varepsilon. \tag{6.15}$$

Finally, we take the interactions into account by looking at the two layers. If two particles hop forward in time at the same site (that is, if there are any overlapping outgoing bonds among the two layers), we multiply the local weight

by

$$W_I = \exp(-\varepsilon U). \tag{6.16}$$

With the above assignments for the local weights, we see that the weight of a full configuration can be written as

$$\Omega(\mathcal{C}) = (W_m^{\uparrow})^{L_T N_{\uparrow}} (W_m^{\downarrow})^{L_T N_{\downarrow}} (W_h^{\downarrow})^{n_h^{\downarrow}} (W_h^{\uparrow})^{n_h^{\uparrow}} (W_I)^{n_I}, \tag{6.17}$$

where L_T is the number of lattice sites in the temporal direction, N_σ is the number of σ-particles in the configuration $\mathcal{C}$, n_h^σ is the number of spatial hops and n_I is the number of interacting temporal bonds.

We note that even though the spacetime worldline formulation allows purely spatial loops (with no temporal hops), such configurations are highly suppressed for small ε and do not contribute in the $\varepsilon \to 0$ limit.

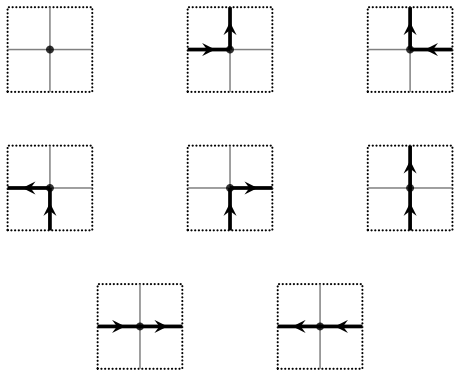

Figure 6.2: The allowed worldline configurations $\mathcal{C}$ on a 1+1 dimensional spacetime lattice site for one particle species. Using the weights defined in Eqs. (6.15) to (6.16), the weights of the configurations from left to right are (top row) $1, W_m, W_m$, (middle row) W_h, W_h, W_m, (bottom row) W_h, W_h. In addition to these weights if both layers have the weight W_m we multiply the product with W_I. (Figure reproduced from Ref. [74].)

6.3.1 Observables

Several interesting observables can easily be expressed in the worldline formulation. In this work, we focus on two main observables. The first is the expectation value of the energy, which can be expressed in the worldline formulation, correct up to $O(\varepsilon)$ as

$$\langle E \rangle = \frac{1}{Z_\mu} \sum_{\mathcal{C}} E(\mathcal{C})\, \Omega(\mathcal{C}) \tag{6.18}$$

where we define the energy of a worldline configuration $E(\mathcal{C})$,

$$E(\mathcal{C}) = U \frac{n_I(\mathcal{C})}{L_T} + \sum_{\sigma} \left[-\frac{n_h^\sigma(\mathcal{C})}{\beta} + 2dt_\sigma N_\sigma(\mathcal{C}) \right]. \tag{6.19}$$

This expression for $E(\mathcal{C})$ can be derived from Eq. (6.17) by noting that $Z = \sum_{\mathcal{C}} \Omega(\mathcal{C})$

$$\langle E \rangle = \frac{1}{Z} \sum_{\mathcal{C}} \frac{\partial \Omega(\mathcal{C})}{\partial \beta} \tag{6.20}$$

and the β derivative of the configuration weight $\Omega(\mathcal{C})$ is itself proportional to the weight,

$$\frac{\partial \Omega(\mathcal{C})}{\partial \beta} = E(\mathcal{C}) \Omega(\mathcal{C}). \tag{6.21}$$

Therefore, we may interpret the proportionality factor $E(\mathcal{C})$ as the energy of a configuration.

We can also easily measure the average particle number $\langle N_\sigma \rangle$ for each species, since each worldline configuration $\mathcal{C}$ has a well-defined particle number $N_\sigma(\mathcal{C})$. The particle number $N_\sigma(\mathcal{C})$ can be measured by considering any time slice and counting the number of worldlines passing through it, with orientation. Thus,

we can write

$$\langle N_\sigma \rangle = \frac{1}{Z_\mu} \sum_{\mathcal{C}} N_\sigma(\mathcal{C})\, \Omega(\mathcal{C}). \tag{6.22}$$

6.4 Worm algorithm

Fortunately, it is well known how to construct worm algorithms to sample worldline configurations of the type shown in Fig. 6.1 [75, 76]. Such an algorithm was also proposed for the eight-vertex model in Ref. [77]. In this work, we use an extension of that algorithm. Let us describe the algorithm in some detail.

For convenience in describing the worm algorithm, we imagine that each particle species lives in a different 'layer.' During a worm update, we select a layer and perform a worm update on that layer, while keeping the other layers fixed. Once the worm update on a given layer is complete, we then move to the next layer and repeat this process until we have updated all the layers. While in this work we consider only two particle species, and hence only two layers, it is very easy to accommodate any number of layers.

We begin a worm update on a given layer by picking a spacetime site at random. At this site, we introduce a particle creation/annihilation event in the lattice. We shall refer to configurations with a single particle/annihilation event as *worm* configurations. We label the particle creation event as the worm head, and the particle annihilation event as the worm tail. Though the worm update begins with the worm head and tail at the same site, we perform local updates to move the worm head around. All the local updates satisfy detailed balance (see Section 3.3). As the worm head moves, it modifies the local configurations. Finally, when the worm head meets the worm tail, the worm "closes" – that is, the worm update for this layer ends. We then repeat this update for the next layer.

To specify the worm algorithm, we must discuss: (i) what the local updates are for the worm head, and (ii) how to choose probabilities for each move such that detailed balance is satisfied. We do this in turn.

6.4.1 Local updates

We discussed the possible local configurations in Fig. 6.2, where we show all possible combinations of incoming and outgoing bonds at each lattice site, on a given layer. However, to discuss local worm updates, we also include the information about the location of the worm head in the diagrams for local configurations. For example, the following figure represents a local configuration where the worm head is about to enter a filled site from the left, and the site already has a spatial incoming bond and outgoing temporal bond:

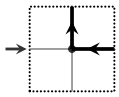

We use this notation in all further discussion of local updates, for example in Figs. 6.3 and 6.4. To implement the worm algorithm, we divide the local updates into two classes:

1. begin-end updates: local updates that begin or end a worm update on a layer; and

2. move updates: local updates that move the worm head, but cannot begin or end a worm update.

When a worm head enters a site, the local site configuration determines the local update that is applied. Within each class above (begin-end or move updates), we determine the collection of local site configurations that can transform into each other within a local update. We call such a collection of local configurations an *update group*.

The detailed balance for an update group is different depending on the number of local configurations within it. We define an n-flip as an update group with n local configurations. We need to work out detailed balance for various n, which we do in Section 6.4.2. But first we must enumerate all the update groups.

Begin-end updates

Let us consider the begin-end updates first. All the update groups for a $1+1$ dimensional lattice are shown in Fig. 6.3. When the worm update begins, we visualize it as a worm head entering the site from the center.

When the worm update begins, there are only two possibilities: either the worm enters on a filled site, or on an empty site. When the worm enters a filled site, it deletes the incoming bond at the site and moves the worm head to the nearest neighbor in the direction of the incoming bond. For example, if the local configuration has an incoming spatial bond, and an outgoing temporal bond, then we perform the following update:

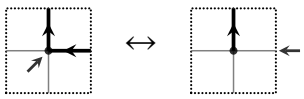

Since all local updates must satisfy detailed balance, we must also allow for the reverse to happen. This occurs when the worm head enters a site which has the worm tail. These two pairs of configurations can therefore transform into each other under local updates. There are other similar 2-flips that can occur, and we enumerate all of them in Fig. 6.3(a).

If, however, the worm update begins on an empty site, then it can create an outgoing bond in any of the $2d$ spatial directions, or an outgoing bond in the *forward* temporal direction. This gives us a $(2d+2)$-flip. In $d=1$ spatial dimensions, we get the 4-flip shown in Fig. 6.3(b).

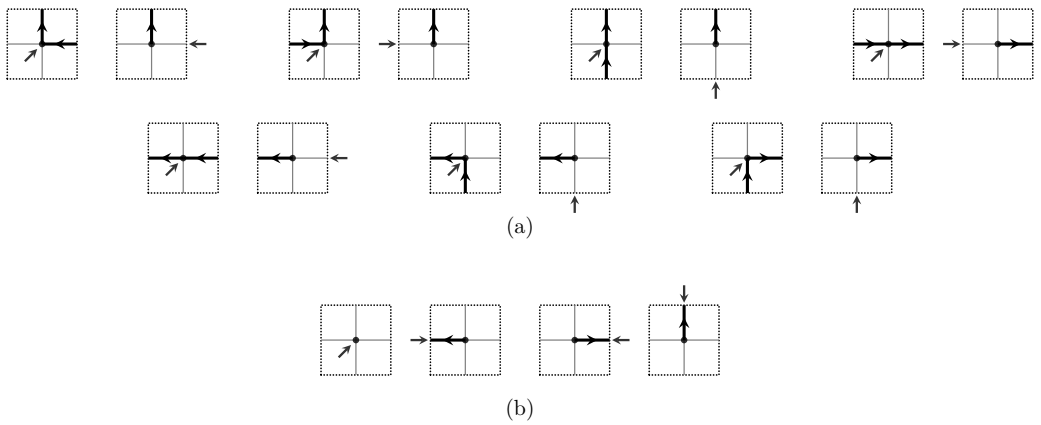

Figure 6.3: The eight update groups corresponding to begin-end n-flips in $1+1$ dimensions, classified by n (how many local configurations can transform into each other), and where the worm update begins: (a) 2-flip, begins on a site with an existing particle, or (b) 4-flip, on an empty site. The small arrow in each local configuration depicts the direction of an incoming worm. The outgoing worm direction can be obtained by reversing this arrow. (Figure reproduced from Ref. [74].)

Move updates

Between the begin-end updates, we use move updates to move the worm head through the spacetime lattice. All the local update groups for move updates in $1+1$ spatial dimensions are shown in Fig. 6.4. We have n-flips with $n = 2$, 3 or 4.

The 2-flips involve the situation where the worm head enters a filled site through an empty bond. In such cases, the worm head creates an incoming bond as it comes in, deletes the existing incoming bond and moves out of the site in the direction of the pre-existing incoming bond. There are several local configurations where this type of an update can happen, and all of them are shown in Fig. 6.4(a) for a $1+1$ dimensional lattice.

Then there are cases when the worm head enters either an empty site, or it enters a filled site by deleting an outgoing bond. These can lead to $(2d+1)$-flips or $(2d+2)$-flips, depending on the direction through which the worm head enters. For example, in $1+1$ dimensions, these correspond to the 3-flips and 4-flips shown in Fig. 6.4(b) and (c), respectively.

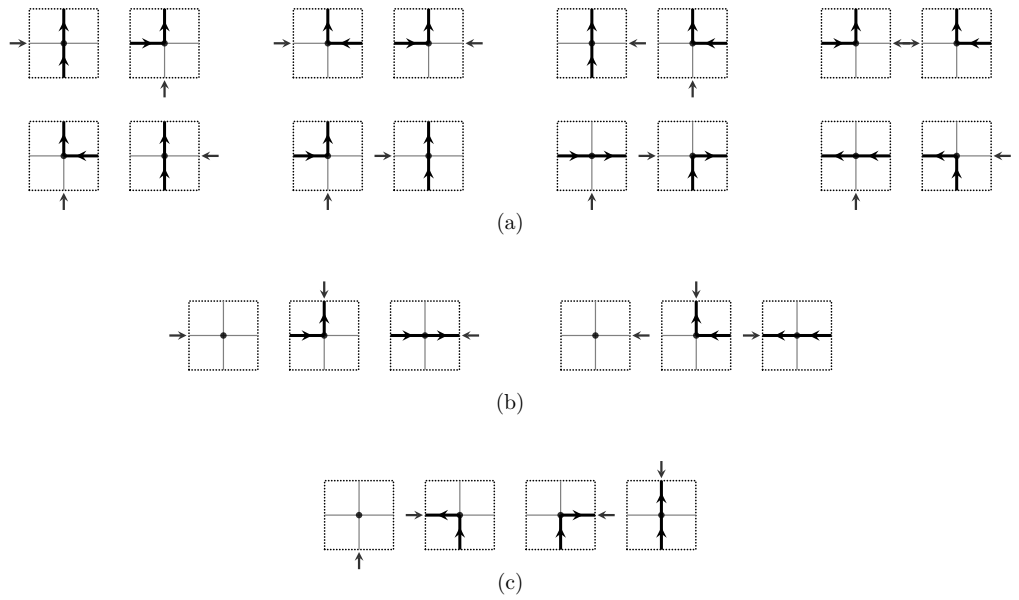

Figure 6.4: Local worm updates in $1+1$ dimensions when (a) the worm enters a site which already contains a particle worldline; (b) the worm enters an empty site along the spatial direction; or (c) the worm enters an empty site along the forward time direction. (Figure reproduced from Ref. [74].)

6.4.2 Detailed balance

As discussed above, a worm algorithm works by moving the worm head around using local updates which must satisfy detailed balance. An n-flip has n local configurations that can transform into each other. Let us denote the local configurations in an n-flip by $C_1, C_2, \ldots, C_n$, with weights $W_1, W_2, \ldots, W_n$, respectively. Let the transition probability to go to C_i from C_j be given by P_{ij}, where P is the $n \times n$ transition matrix. Detailed balance within an n-flip requires

$$P_{ji} W_i = P_{ij} W_j \quad \text{for all} \quad i, j = 1, \ldots, n. \tag{6.23}$$

where no summation over repeated indices is implied.

To have an efficient algorithm which quickly generates uncorrelated configurations, an important heuristic is to minimize "bounces" [78]. A bounce is when during a local update the local configuration does not change. In terms of our picture of a worm entering a site, this would mean that the worm head just

bounces back, and goes back into the previous site.

In our $(d+1)$ dimensional model, we encounter n-flips with $n = 2, (2d+1)$ and $(2d+2)$. For $d = 1$ spatial dimensions, this means we need to work out the detailed balance for $n = 2$, 3 and 4 flips. We do this one by one.

n-flips with $n = 2$

Looking at all the 2-flips shown in Figs. 6.3 and 6.4, we see that the outgoing bond never changes. Since we define the weight of a local configuration to be the weight of the outgoing bond, the local weights W_1 and W_2 are identical. The detailed balance equation,

$$P_{21} W_1 = P_{12} W_2, \tag{6.24}$$

implies $P_{21} = P_{12}$. Therefore, we can completely eliminate bounces by choosing $P_{12} = P_{21} = 1$. The local update in this case simply toggles between the two configurations with probability one. The local update for 2-flips can be represented by the following directed graph and transition matrix:

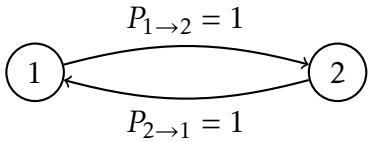

$$\mathbf{P} = \begin{pmatrix} 1 & 0 \\ 0 & 1 \end{pmatrix} \tag{6.25}$$

n-flips with $n = 3$

For update groups with more than two configurations, such as the 3-flips shown in Fig. 6.4(b), we have to work slightly harder to make sure that detailed balance is satisfied and that bounces are minimized. We can show that it is possible to eliminate bounces in our model, at least in the $\varepsilon \to 0$ limit.

Let us assume we have three configurations C_1, C_2, C_3 with weights W_1, W_2, W_3, respectively. Let W_1 be the largest of the weights, without loss of generality. We

consider two cases.

- Case I: $W_1 \leq W_2 + W_3$

  In this case, bounces can be eliminated for or arbitrary temporal spacing ε. To assign the transition probabilities, let $W = W_1 + W_2 + W_3$ be the sum of all the weights, and let

$$\Omega_{ij} = (W_i + W_j) - \frac{1}{2}W. \tag{6.26}$$

  We define the transition probabilities to be

$$P_{ij} = \frac{\Omega_{ij}}{W_j} \qquad \text{for} \quad i \neq j, \quad \text{and} \tag{6.27}$$

$$P_{ij} = 0 \qquad \text{for} \quad i = j. \tag{6.28}$$

  The last equation above implies that bounces will never happen. We can see that the assignments in Eq. (6.28) are well-defined probabilities since they are positive semi-definite $P_{ij} \geq 0$ for all $i, j = 1, 2, 3$, and sum to one: $\sum_j P_{ji} = 1$. We can represent this by the following transition matrix:

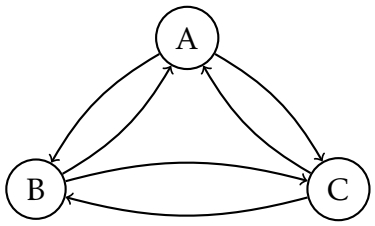

$$\mathbf{P} = \begin{pmatrix} 0 & \frac{\Omega_{12}}{W_1} & \frac{\Omega_{13}}{W_1} \\ \frac{\Omega_{21}}{W_2} & 0 & \frac{\Omega_{23}}{W_2} \\ \frac{\Omega_{31}}{W_3} & \frac{\Omega_{32}}{W_3} & 0 \end{pmatrix} \tag{6.29}$$

- Case II: $W_1 > W_2 + W_3$ In this case, we can not avoid the bounce generally. However, we can choose the transition probabilities such that the bounce

is eliminated in the $\varepsilon \to 0$ limit. We choose the following transition matrix:

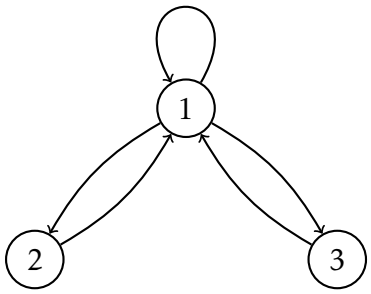

$$\mathbf{P} = \begin{pmatrix} 1 - \frac{W_2+W_3}{W_1} & \frac{W_2}{W_1} & \frac{W_3}{W_1} \\ 1 & 0 & 0 \\ 1 & 0 & 0 \end{pmatrix} \tag{6.30}$$

We can see that the largest weight configuration C_1 can bounce. However, let us consider, for example, one of the 3-flips shown in Fig. 6.4:

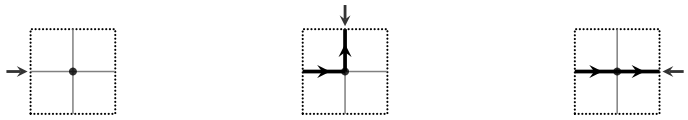

which have weights

$$W_1 = 1, \quad W_2 = e^{-\varepsilon(2dt_\sigma - \mu_\sigma)}, \quad W_3 = t_\sigma \varepsilon. \tag{6.31}$$

In the $\varepsilon \to 0$ limit, $W_1, W_2 \to 1$ and $W_3 \to 0$. This implies that the bounce probability goes to zero. If W_1 is the largest weight,

$$P_{11} = 1 - \frac{W_2 + W_3}{W_1} \to 0. \tag{6.32}$$

Essentially, in the $\varepsilon \to 0$ limit, the 3-flip reduces to a 2-flip, since the configurations with outgoing spatial bonds are extremely unlikely.

n-flips with $n > 3$

In our work, we encounter n-flips with $n > 3$ having the property that the weights of $(n-2)$ configurations are identical. Therefore, we can just generalize the 3-flips to include this case by grouping those $(n-2)$ configurations into a single configuration.

For example, consider the 4-flips shown in Fig. 6.3 or Fig. 6.4. In both cases, the weights of the configurations are

$$W_1 = 1, \quad W_2 = W_m, \quad W_3 = W_4 = W_h, \tag{6.33}$$

where the last two both contain an outgoing spatial bond. Here we only have two configurations with an outgoing spatial bond because we are in $1+1$ dimensions. Generally, for the $d+1$ dimensional system, we will have out $2d$ such configurations with same the weight,

$$W_1 = W_e, \quad W_2 = W_t, \quad W_3 = W_4 = \cdots = W_{2d-2} = W_s. \tag{6.34}$$

We define a configuration X with the weight

$$W_X = W_3 + \cdots + W_{n-2} = (n-2)W_3. \tag{6.35}$$

Now we have three configurations: 1, 2 and X, and we can use the detailed balance described in the previous section for 3-flips.

6.5 Fermions and sign problems

Our model is defined with hard-core bosons. However, if we define our model with fermions instead, the derivation of Section 6.3 will go through identically and again give us a worldline representation with a sum over worldline configurations of the same type. The only difference will come from an additional sign from the permutation of fermionic worldlines. The fermionic partition function is

$$Z^f = \sum_{\mathcal{C}} S(\mathcal{C})\Omega(\mathcal{C}), \tag{6.36}$$

where $S(\mathcal{C})$ is the sign associated with configuration $\mathcal{C}$, and $\Omega(\mathcal{C})$ is the same weight of a configuration of hardcore bosons that we defined earlier. Further, this can be expressed in terms of the bosonic partition function Z as

$$Z^f = \left(\sum_{\mathcal{C}} \Omega(\mathcal{C})\right) \frac{\sum_{\mathcal{C}} S(\mathcal{C})\Omega(\mathcal{C})}{\sum_{\mathcal{C}} \Omega(\mathcal{C})} \tag{6.37}$$

$$= Z\langle S(\mathcal{C})\rangle_{\mathcal{C}} \tag{6.38}$$

where $\langle\cdots\rangle_{\mathcal{C}}$ represents expectation values computed in the worldline representation of Z. Any other observable O in the fermionic theory can also be computed by sampling the bosonic system,

$$\langle O\rangle_f = \frac{\sum_{\mathcal{C}} O(\mathcal{C})S(\mathcal{C})\Omega(\mathcal{C})}{\sum_{\mathcal{C}} S(\mathcal{C})\Omega(\mathcal{C})} \tag{6.39}$$

$$= \frac{\langle O(\mathcal{C})S(\mathcal{C})\rangle_{\mathcal{C}}}{\langle S(\mathcal{C})\rangle_{\mathcal{C}}} \tag{6.40}$$

Even though we can compute the fermionic observables this way in principle, it is a priori not clear whether this will be an efficient way of doing so. For example, let us consider the computation of the ground state energy of the fermonic system E^f. This can be extracted by looking at the average sign

$$\langle S(\mathcal{C})\rangle_{\mathcal{C}} = \frac{Z^f}{Z}. \tag{6.41}$$

In the large β limit, only the respective ground state contributes to each of the partition functions and hence the average sign is

$$\langle S(\mathcal{C})\rangle_{\mathcal{C}} = e^{-\beta(E^f - E_0)} + (\text{higher excited states}). \tag{6.42}$$

Since we can directly measure the average sign $\langle S\rangle$ and the bosonic energy $\langle E\rangle$

in our worldline representation, we can a fermionic energy observable $\langle E^f \rangle$

$$\langle E^f \rangle = \langle E \rangle - \frac{1}{\beta} \ln (\langle S \rangle), \tag{6.43}$$

which gives us the ground state energy of the fermionic system in the $\beta \to \infty$ limit,

$$E^{f,0}_{N_\uparrow, N_\downarrow} = \lim_{\beta \to \infty} \langle E^f \rangle. \tag{6.44}$$

However, note that Eq. (6.42) implies that the sign observable decays exponentially in β as we make β large. Therefore, the fermionic energy observable (6.43) can have a severe SNR problem. We comment on this for this problem for systems in one spatial dimensions.

6.5.1 1+1 dimensional systems

In one spatial dimensions, the worldline approach leads to a solution of the sign problem [71]. This is because, in one spatial dimension with only nearest neighbor hops, the particle worldlines cannot cross each other. So the only fermionic permutations that are allowed are cyclic permutations. An example is shown in Fig. 6.5. For a system with periodic boundary conditions, we can write down the sign of a configuration from a cyclic permutation as

$$S(\mathcal{C}) = (-1)^{\sum_\sigma (N_\sigma(\mathcal{C})-1) N_w^\sigma(\mathcal{C})}, \tag{6.45}$$

where the winding number N_w^σ is the number of times worldlines of σ-type particles wind around the periodic box. We can immediately see that, in particular, if $N_\uparrow$ and $N_\downarrow$ are both odd, then $S(\mathcal{C}) = 1$. Moreover, in a trapping potential or with open boundary conditions, the fermions cannot wind around the box, so N_w^σ just vanishes. Again, the sign problem is solved.

We see that in all these cases, fermions and hardcore bosons are completely equivalent. However, this does not work for systems with spatial dimensions $d > 1$. The fermions have enough room to just wind around each other, and the fermionic sign problem returns.

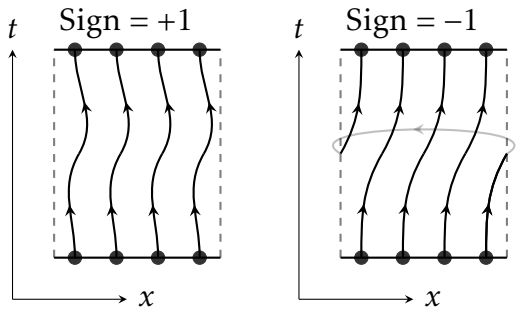

Figure 6.5: An illustration of how the fermionic sign arises in the worldline formulation in one spatial dimensions. The configuration on the left has no permutation of the worldline configurations and hence no sign. In the right figure, one of the particle worldlines wraps around the edge of the periodic box causing all the fermions to shift to the right by one position. This is an odd permutation, which gives a negative sign. (Figure reproduced from Ref. [73].)

6.6 One-dimensional systems

In this section, we use our methods to compute the ground state energies for two species of hardcore bosons in $1+1$ dimensions, for a wide range of interaction strengths and mass-imbalances. As discussed in Section 6.5.1, in 1+1 dimensions, hardcore bosons are exactly equivalent to fermions in many cases of interest. Therefore, all of the results in this section are valid for a system of fermions as well without any changes. In cases where we can check against exact solutions or perturbation theory, we do so and find excellent agreement. However, we find that our method works well even in parameter regimes where other methods fail.

We keep a fixed box size of $L_X = 40$ (lattice units) and use periodic boundary conditions. We will work with only an odd number of particles of each type, in

which case hardcore bosons and fermions are completely equivalent.

We work in sectors of fixed particle number of each type. Let the total number of particles be $N = N_\uparrow + N_\downarrow$, where $N_\uparrow$ and $N_\downarrow$ denote the number of spin-$\uparrow$ and spin-$\downarrow$ particles, respectively. The particle-number density is $n = N/L_X$. We define the average mass m and the mass-imbalance parameter $\overline{m}$ as

$$m = \frac{m_\uparrow + m_\downarrow}{2}, \quad \overline{m} = \frac{m_\uparrow - m_\downarrow}{m_\uparrow + m_\downarrow}, \tag{6.46}$$

respectively. We work in units with average mass $m = 1$ and the lattice spacing $a = 1$. For convenient comparison with the literature, we parameterize the interaction strength by

$$\gamma = \frac{U}{n}. \tag{6.47}$$

where U is the bare coupling used in the lattice model (6.4). We report all energies in units of the corresponding one-dimensional ideal spin- and mass-balanced Fermi-gas ground state energy E_{FG},

$$E_{\mathrm{FG}} = \frac{1}{3} N \epsilon_{\mathrm{F}}, \tag{6.48}$$

where $\epsilon_{\mathrm{F}} = \pi^2 n^2 / 8m$ is the Fermi energy.

Finally, we compute all energies at a fixed inverse temperature of $\beta = 100$, which we find to be large enough for our purposes. However, it is important to understand the dependence of the results on β carefully to perform zero-temperature extrapolations, as is commonly done in the lattice field theory community. However, we do perform extrapolations to continuous time ($\varepsilon \to 0$), since we find that these errors tend to be large otherwise.

6.6.1 Mass-balanced Systems

We begin by considering mass- and spin-balanced systems of $N_\uparrow = N_\downarrow$ fermions (or, equivalently, hardcore bosons), where the particle numbers are taken to be odd,

$$N_\uparrow = N_\downarrow \text{ (odd)}, \quad \text{and} \quad \overline{m} = 0. \tag{6.49}$$

This case is an excellent testing ground for our technique for a wide range of couplings since the model can be exactly solved using the Bethe ansatz. This is especially important for the strong coupling regime. After briefly discussing the exact solution, we do a comparison with our Monte Carlo technique and find excellent agreement.

Exact solution using the Bethe ansatz

The continuum model (6.3) for mass-balanced fermions in $1+1$ dimensions and positive coupling ($g > 0$) was one of the first models to be solved using Bethe ansatz. For this reason, it is also known as the Gaudin-Yang model after the authors of Refs. [79, 80]. The exact solution was also extended to the lattice model (6.4) with $\overline{m} = 0$, which is also called the Hubbard model [81].

For repulsive couplings, we can obtain exact ground state energies by a numerical solution of the Bethe ansatz equations, both for the continuum and lattice models. For attractive couplings $g < 0$, the continuum model is unstable. But the lattice model in a finite box is well-defined. We can compute the ground state energy for the attractive lattice model by performing a particle-hole transformation on the system, as discussed below.

To solve for the ground state using the Bethe ansatz, let us assume that we have $N_\downarrow = M$ spin-down fermions, and $N_\uparrow = N - M$ spin-up fermions with identical masses. We choose the hopping parameters to be $t_\uparrow = t_\downarrow = t$, and we take the

coupling to be repulsive, $U > 0$. Let $P = (p_1, \ldots, p_N)$ and $\Lambda = (\lambda_1, \ldots, \lambda_M)$ be two collections of ascending real numbers, which are to be determined. In this subsection, the index i runs over $\{1, \ldots, N\}$ and the index λ runs over $\{1, \ldots, M\}$. Nested Bethe ansatz yields the following $N + M$ coupled non-linear equations in the $N + M$ variables P, Λ:

$$2\pi I_i = L_X p_i - \sum_{\alpha=1}^{M} \theta(2\sin p_i - 2\lambda_\alpha), \qquad \text{for } i = 1, \ldots, N, \tag{6.50}$$

$$2\pi J_\alpha = \sum_{\beta=1}^{M} \theta(\lambda_\alpha - \lambda_\beta) - \sum_{i=1}^{N} \theta(2\lambda_\alpha - 2\sin p_i), \qquad \text{for } \alpha = 1, \ldots, M, \tag{6.51}$$

where

$$\theta(p) \equiv -2\tan^{-1}\left(\frac{2pt}{U}\right) \in [-\pi, \pi), \tag{6.52}$$

and I_i, J_α are specific integers (or half-odd integers) for N, M even (or odd) that uniquely label the energy eigenstates. Once we choose values for I_i, J_α, we can numerically solve the above equations for p_i, Λ_α. The energy eigenvalue corresponding to this choice of I_i, J_α is then given by

$$E = 2t \sum_{i=1}^{N} (1 - \cos(p_i)). \tag{6.53}$$

The ground state corresponds to the choice

$$I_i = -\frac{1}{2}(N+1) + i \qquad \text{for } i = 1, \ldots, N \text{ , and} \tag{6.54}$$

$$J_\alpha = -\frac{1}{2}(M+1) + \alpha \qquad \text{for } \alpha = 1, \ldots, M. \tag{6.55}$$

Finally, the ground state for the attractive Hubbard model (with $U < 0$) can be

obtained from the solution of the $U > 0$ ground state using the relation,

$$E_0(N_\uparrow, N_\downarrow, U) = E_0(N_\uparrow, L - N_\downarrow, -U) + UN_\uparrow - 2t_\downarrow(L - 2N_\downarrow). \tag{6.56}$$

which can be derived by using a particle-hole transformation on one of the spins.

Results

We show our results for mass-balanced fermions in Fig. 6.6, for $N_\uparrow = N_\downarrow = 5$, over a wide range of repulsive couplings. The plot on the left shows the range of couplings $\gamma \in (0.0, 3.0)$, while the plot on the right shows the larger range $\gamma \in (0.0, 8.0)$.

The exact ground state energy from the Bethe ansatz is shown as a blue dashed line labeled "Bethe ansatz." We also show results from perturbation theory up to second order. For couplings $\gamma \gtrsim 3$ (shown in the plot on the right), the model becomes quite non-perturbative, as the first and second-order corrections must undergo large cancellations to give the correct Bethe ansatz value. The results from our method are labelled "Worm algorithm," and are shown as red dots. We see that our method reproduces the exact Bethe ansatz results for the entire range of couplings. For these results, we found $\beta = 100$ to be sufficient, but did extrapolate to continuous time $\varepsilon \to 0$.

For comparison, we also show the recent CL results from Ref. [32]. We observe that the CL method works quite well in the perturbative regime, but starts to deviate from the exact results when $\gamma \gtrsim 2.5$.

In the left plot of Fig. 6.7, we show a comparison between the worm algorithm and the exact results in both the lattice model and the continuum limit. As can be seen, the worm algorithm results show a slight discrepancy from the lattice Bethe ansatz results. This small discrepancy is due to β being finite. This is shown in the plot on the right, where we pick the point $\gamma = 6.2$, and perform MC calculations at larger and larger β. We mark both the continuum and lattice

results for the $1/(\beta\epsilon_F) \to 0$ limit. As can be seen, the worm algorithm can resolve even the small difference between the lattice and continuum results as we take the $1/(\beta\epsilon_F) \to 0$ limit.

6.6.2 Mass-imbalanced Systems

Now, we move on to more general mass-imbalanced systems (with $\overline{m} \neq 0$), where no exact solution is known. However, as we show in this section, the worm algorithm performs very well even in such cases.

In Fig. 6.8, we show the ground state energy of a system of $N_\uparrow = N_\downarrow = 5$ fermions, with a high mass imbalance of $\overline{m} = 0.8$, as a function of the coupling. We vary the coupling across a wide range, and again compare our results with perturbation theory up to second order, as well as to the CL results of Ref. [32]. The left plot shows a smaller range of couplings $\gamma \in [0, 3.0]$, while the right plot extends it to a bigger range $\gamma \in [0.0, 8.0]$.

Our algorithm shows no inefficiencies even in the mass-imbalanced case, for the entire range of couplings. Although the exact Bethe ansatz solution does not apply here, we do compute the energies from second-order perturbation theory and find good agreement for small values of the coupling. As before, our computations are performed at inverse temperature $\beta = 100$.

Even though both the worm algorithm and second-order perturbation theory agree up to $\gamma \sim 3.0$, we see that the CL results start disagreeing with both methods already beyond $\gamma \gtrsim 2$. In Ref. [32], the authors suggested that the 'flattening' in the curve for the ground-state energy as a function γ seen with the CL method, was a genuine physical effect in the strong coupling regime. However, as we have shown above, the CL method disagrees with the exact Bethe ansatz calculations in the mass-balanced case, and with both the worm algorithm and second-order perturbation theory at high mass imbalances. This strongly indicates that the 'flattening' observed in Ref. [32] is a artifact of the CL method.

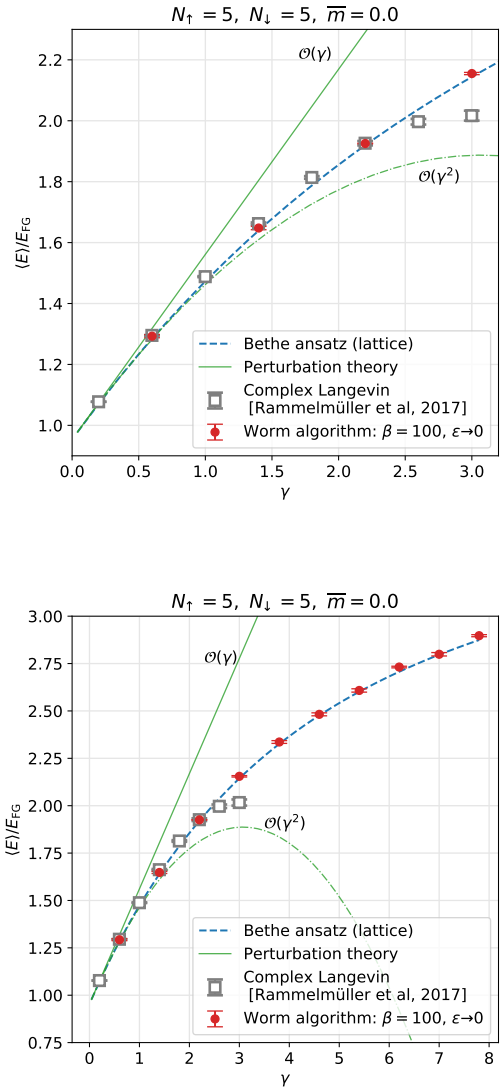

Figure 6.6: Plots of ground state energy as a function of γ in the mass balanced case ($\overline{m} = 0.0$), with $N_\uparrow = N_\downarrow = 5$. The left figure focuses on the perturbative regime while the right figure extends it to the non-perturbative region. The CL results shown are from [32]. Note that they begin to disagree with exact results around $\gamma \gtrsim 2.5$. (Figure reproduced from Ref. [74].)

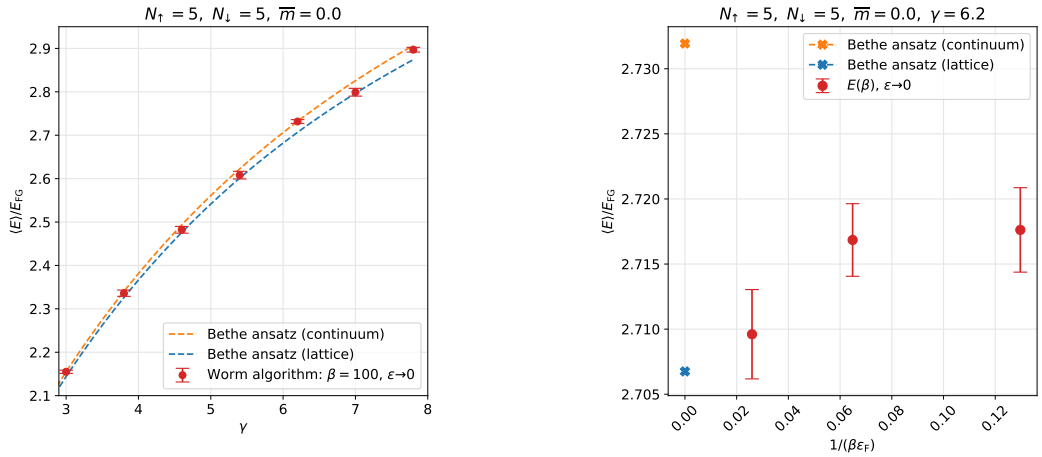

Figure 6.7: The left figure shows a comparison between the worm algorithm results at $L_X = 40$, $\beta = 100$, $\varepsilon \to 0$, $\overline{m} = 0.0$, $N_\uparrow = N_\downarrow = 5$, with the results obtained using the Bethe ansatz on a lattice with $L_X = 40$ and in the continuum. The β dependence of the energies plotted at $\gamma = 6.2$ in the right figure shows that the worm algorithm results are sensitive to the small difference between the lattice and continuum. In the $\beta\epsilon_F \to \infty$ limit, we recover the exact lattice result as expected. (Figure reproduced from Ref. [74].)

Next, we perform a comparison between different methods for a fixed attractive coupling, across a range of mass-imbalances. We show this comparison in Fig. 6.9, for $N_\uparrow = N_\downarrow = 3$ fermions. The results from imaginary-mass Hybrid Monte Carlo (IHMC) and CL methods shown are from Ref. [32]. We see that IHMC has larger errors for higher $\overline{m}$, while the worm algorithm has consistently small error bars in the entire range of $\overline{m}$. The CL results are unpublished data from the authors of Ref. [32]. Unlike the repulsive case, these results are well in agreement with the worm algorithm. At $\overline{m} = 0$ we also show the exact result from the Bethe ansatz. Although our results are clearly in disagreement with the Bethe ansatz at $\overline{m} = 0$, this discrepancy is entirely within the $O(1/\beta)$ corrections expected from a finite temperature computation.

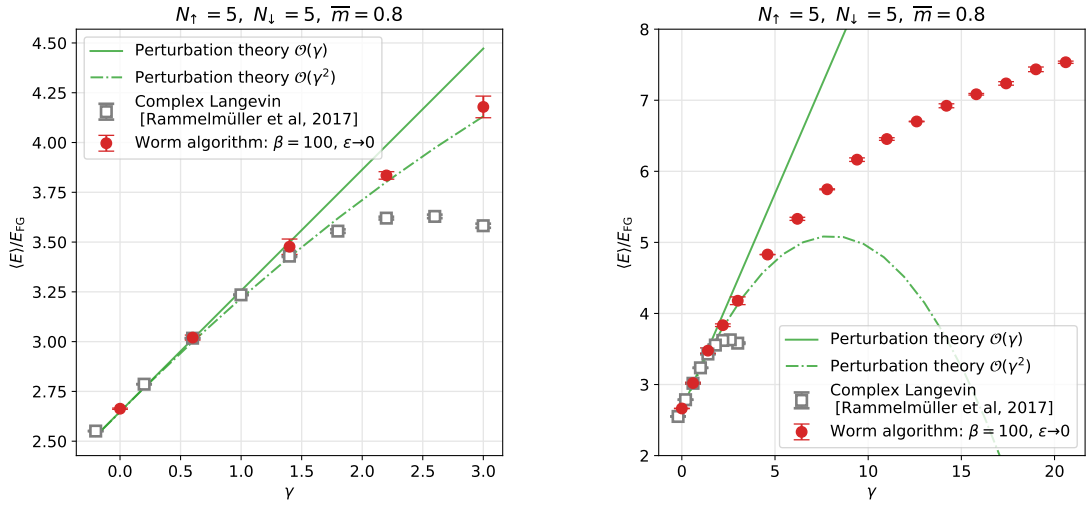

Figure 6.8: Plots of ground state energy as a function of γ in the high mass imbalanced case ($\overline{m} = 0.8$), with $N_\uparrow = N_\downarrow = 5$. The left figure focuses on the perturbative regime while the right figure extends it to the non-perturbative region. The CL results shown are from [32] and begin to disagree with the worm algorithm around $\gamma \gtrsim 2$, even in the regime where second-order perturbation theory works well. (Figure reproduced from Ref. [74].)

6.7 Conclusions

In this work, we developed an efficient worldline approach to study few-body physics of two species of hard-core bosons in an arbitrary dimensions. In the worldline representation, the fermionic sign arises from permutations of worldlines. In one spatial dimensions with nearest neighbor interactions, this leads to a solution of the sign problem in cases where fermions can not wind around the system. We compared our results across a range of other methods. We noted that the recent CL results from Ref. [32] seem to be converging to the wrong results for stronger repulsive couplings, as suspected by the authors. Since exact results from Bethe ansatz are available for the mass-balanced case, we were able to confirm this, and validate the worm algorithm results. While our technique works for hardcore bosons in any dimensions, it would be interesting to systematically explore the severity of the fermionic sign problem in higher

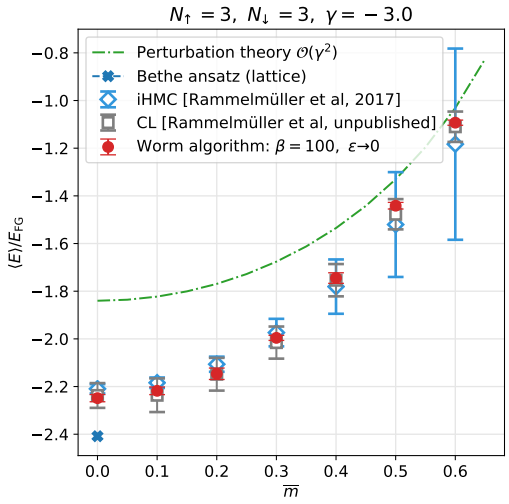

Figure 6.9: Energy as a function of mass-imbalance $\overline{m}$. Note that the lattice model is invariant under $\overline{m} \to -\overline{m}$, which implies that the curve is quadratic in $\overline{m}$ for small values of $\overline{m}$. We show our data using the worm algorithm along with the iHMC results of Ref. [32], unpublished CL data given to us by the authors of Ref. [32], and second order perturbation theory. The apparent discrepancy at $\overline{m} = 0$ between our results and the results from the Bethe ansatz is completely due to finite β. (Figure reproduced from Ref. [74].)

dimensions in a future publication.

Chapter 7

Conclusions

The goal of this thesis was to study quantum field theories (QFTs) using the idea of qubit regularization. The essence of this idea is to construct quantum lattice Hamiltonians with a finite dimensional local Hilbert space such that the universal physics of a given QFT emerges close to a quantum critical point, as dictated by the ideas of Wilson's renormalization group (RG).

A major motivation for considering such a regularization of QFTs comes from the excitement in the community regarding the prospect of quantum simulation of QFTs. This has led to a search for new formulations of lattice QFTs which might be better suited for implementation on quantum computers. Many proposals in the literature start with a conventional lattice regularization, which might have an infinite dimensional local Hilbert space, and then truncate it to a finite dimensional subspace, with the aim of systematically restoring the local Hilbert space at the end. In contrast to such proposals, in a qubit regularization we do not explicitly restore the local Hilbert space. Rather, the existence of a quantum critical point in the right universality class ensures that the continuum QFT emerges. In a sense, we let RG construct the infinite-dimensional Hilbert space of the continuum QFT for us.

As an example of an important relativistic QFT, we constructed a qubit model for the $O(N)$ nonlinear sigma model (NLSM) in $D \geq 3$ spacetime dimensions. Using efficient Monte Carlo (MC) algorithms we established the critical scaling behavior of this model, and computed a few critical exponents. Upon comparison with existing results in the literature for the Wilson-Fisher (WF) fixed point, we found excellent agreement. Therefore, this model lies in the expected $O(N)$

WF universality class for $N = 2, 4, 6, 8$ and can be used to study the $O(N)$ WF continuum field theory.

Having established a qubit regularization of the $O(N)$ NLSM, we could now in principle, explore quantum algorithms for simulations on digital quantum computers. This direction is actively being pursued, such as Ref. [82].

Qubit regularizations are similar in spirit to the idea of D-theory [13, 15, 83], which also uses quantum spin systems to construct continuum QFTs. In particular, D-theory achieves a continuum limit of asymptotically free theories by dimensional reduction. For example, we could use D-theory to construct a regularization of the *two-dimensional* $O(3)$ NLSM, something that we did not consider in this work. In our qubit regularization approach, such dimensional reduction might be unnecessary provided we can find the right critical point. This possibility is very exciting, and certainly worth pursuing in a future publication.

Another major motivation for considering qubit models is that they can be sometimes be used to circumvent the signal-to-noise ratio (SNR) problem present in conventional approaches. Therefore, they are relevant purely from a classical lattice MC perspective as well. In this thesis, we demonstrated this by studying sectors of large global charge of the $O(N)$ NLSM, which suffer from a sign problem in the traditional model. Motivated by recent work using the "large-charge" limit to study $O(N)$ WF conformal field theory (CFT), we computed the conformal dimensions of leading large-charge operators. This let us explicitly compute some low-energy constants (LECs) in the effective field theory (EFT) description in the large-charge limit. In particular, we were able to numerically test recent predictions for these LECs from a large-charge and large-N limit, and found good agreement. It would be exciting to extend this work for several other quantities that can be computed from the large-charge approach, especially in subleading sectors where there are some puzzles.

Finally, we also demonstrated our methods in the case of a non-relativistic

quantum mechanical system, where we studied the few-body physics of a system of strongly interacting fermions in one spatial dimension. Such systems appear ubiquitously across physics, and it is important to develop techniques that could be extended to higher dimensions and larger particle numbers. We demonstrated that a worm algorithm can be construced which works beautifully in one dimension, and even uncovered some limitations of recently proposed Complex Langevin methods for this system. We believe that it should be possible to extend this approach to higher dimensions and tame the fermionic sign problem using ideas of exponential error reduction and fermion bags, at least in the few-body sector.

Qubit regularizations might provide an alternative suite of methods to study QFTs. If quantum computers fulfill their promise, such ideas are likely to become even more important. In any case, this program has yielded new results already. Several other exciting threads are being pursued and it will be interesting to see their resolution.

Bibliography

[1] Michael E. Peskin and Daniel V. Schroeder. "An Introduction to Quantum Field Theory" (1995).

[2] R. P. Feynman. "Space-Time Approach to Quantum Electrodynamics." *Physical Review* 76.6 (Sept. 1949), pp. 769–789. DOI: 10.1103/PhysRev.76.769.

[3] Kenneth G. Wilson. "Confinement of Quarks." *Physical Review D* 10.8 (Oct. 1974), pp. 2445–2459. DOI: 10.1103/PhysRevD.10.2445.

[4] Kenneth G. Wilson. "The renormalization group and critical phenomena." *Reviews of Modern Physics* 55.3 (July 1983), pp. 583–600. DOI: 10.1103/RevModPhys.55.583.

[5] K. G. Wilson and John B. Kogut. "The Renormalization Group and the Epsilon Expansion." *Phys.Rept.* 12 (1974), pp. 75–199. DOI: 10.1016/0370-1573(74)90023-4.

[6] Ulrich Schollwöck. "The Density-Matrix Renormalization Group in the Age of Matrix Product States." en. *Annals of Physics*. January 2011 Special Issue 326.1 (Jan. 2011), pp. 96–192. DOI: 10.1016/j.aop.2010.09.012.

[7] Fabio Franchini. "An Introduction to Integrable Techniques for One-Dimensional Quantum Systems." 940 (2017). DOI: 10.1007/978-3-319-48487-7. arXiv: 1609.02100.

[8] Frank Göhmann. "Statistical Mechanics of Integrable Quantum Spin Systems" (June 2020). arXiv: 1909.09967.

[9] Rodney J. Baxter. *Exactly Solved Models in Statistical Mechanics*. 1982. DOI: 10.1142/9789814415255˙0002.

[10] John Preskill. "Simulating Quantum Field Theory with a Quantum Computer" (Nov. 25, 2018). arXiv: 1811.10085.

[11] M. C. Bañuls et al. "Simulating Lattice Gauge Theories within Quantum Technologies" (Oct. 31, 2019). arXiv: 1911.00003.

[12] Yuri Alexeev et al. "Quantum Computer Systems for Scientific Discovery" (Feb. 4, 2020). arXiv: 1912.07577.

[13] U. -J. Wiese. "Quantum Spins and Quantum Links: The D-Theory Approach to Field Theory." en. *Nuclear Physics B - Proceedings Supplements* 73.1 (Mar. 1999), pp. 146–158. DOI: 10.1016/S0920-5632(99)85014-2.

[14] R. Brower, S. Chandrasekharan, and U. J. Wiese. "QCD as a quantum link model." *Phys.Rev.* D60 (1999), p. 094502. DOI: 10.1103/PhysRevD.60.094502.

[15] R. Brower et al. "D-Theory: Field Quantization by Dimensional Reduction of Discrete Variables." en. *Nuclear Physics B* 693.1 (Aug. 2004), pp. 149–175. DOI: 10.1016/j.nuclphysb.2004.06.007.

[16] Wynne Evans et al. "SU(3) Quantum Spin Ladders as a Regularization of the CP(2) Model at Non-Zero Density: From Classical to Quantum Simulation." *Annals of Physics* 398 (Nov. 2018), pp. 94–122. DOI: 10.1016/j.aop.2018.09.002. arXiv: 1803.04767.

[17] B. B. Beard et al. "Efficient Cluster Algorithm for CP(N-1) Models." *Computer Physics Communications* 175.10 (Nov. 2006), pp. 629–634. DOI: 10.1016/j.cpc.2006.06.007. arXiv: hep-lat/0602018.

[18] Massimo Campostrini et al. "The Critical exponents of the superfluid transition in He-4." *Phys.Rev.* B74 (2006), p. 144506. DOI: 10.1103/PhysRevB.74.144506.

[19] Robert D. Pisarski and Frank Wilczek. "Remarks on the Chiral Phase Transition in Chromodynamics." *Physical Review D* 29.2 (Jan. 15, 1984), pp. 338–341. DOI: 10.1103/PhysRevD.29.338.

[20] Krishna Rajagopal. "The Chiral Phase Transition in QCD: Critical Phenomena and Long Wavelength Pion Oscillations." *Quark-Gluon Plasma 2*. WORLD SCIENTIFIC, Nov. 1995, pp. 484–554. DOI: 10.1142/9789812830661_0009.

[21] Frank Wilczek. "QCD In Extreme Conditions." *arXiv:hep-ph/0003183* (Mar. 2000). arXiv: hep-ph/0003183.

[22] Krishna Rajagopal and Frank Wilczek. "Static and Dynamic Critical Phenomena at a Second Order QCD Phase Transition." en. *Nuclear Physics B* 399.2 (July 1993), pp. 395–425. DOI: 10.1016/0550-3213(93)90502-G.

[23] Dirk H. Rischke. "The Quark–Gluon Plasma in Equilibrium." en. *Progress in Particle and Nuclear Physics* 52.1 (Mar. 2004), pp. 197–296. DOI: 10.1016/j.ppnp.2003.09.002.

[24] Alexander B Zamolodchikov and Alexey B Zamolodchikov. "Factorized S-Matrices in Two Dimensions as the Exact Solutions of Certain Relativistic Quantum Field Theory Models." *Annals of Physics* 120.2 (Aug. 1, 1979), pp. 253–291. DOI: 10.1016/0003-4916(79)90391-9.

[25] Simeon Hellerman et al. "On the CFT operator spectrum at large global charge." *Journal of High Energy Physics* 2015.12 (Dec. 2015), pp. 1–34. DOI: 10.1007/JHEP12(2015)071.

[26] Luis Alvarez-Gaume et al. "Compensating strong coupling with large charge." *Journal of High Energy Physics* 2017.4 (Apr. 2017), p. 59. DOI: 10.1007/JHEP04(2017)059.

[27] Debasish Banerjee, Shailesh Chandrasekharan, and Domenico Orlando. "Conformal Dimensions via Large Charge Expansion." *Physical Review Letters* 120.6 (Feb. 2018), p. 061603. DOI: 10.1103/PhysRevLett.120.061603.

[28] Debasish Banerjee et al. "Conformal dimensions in the large charge sectors at the O(4) Wilson-Fisher fixed point." *Phys. Rev. Lett.* 123.5 (2019), p. 051603. DOI: 10.1103/PhysRevLett.123.051603.

[29] Hersh Singh. "Qubit $O(N)$ nonlinear sigma models" (2019). arXiv: 1911.12353.

[30] Hersh Singh. "$O(N)$ qubit models in the large-charge sector." 2020, in preparation.

[31] Luis Alvarez-Gaume, Domenico Orlando, and Susanne Reffert. "Large charge at large N" (2019). arXiv: 1909.02571.

[32] Lukas Rammelmüller et al. "Surmounting the sign problem in non-relativistic calculations: a case study with mass-imbalanced fermions." *Physical Review D* 96.9 (Nov. 2017). DOI: 10.1103/PhysRevD.96.094506.

[33] Ramamurti Shankar. *Quantum Field Theory and Condensed Matter*. Cambridge University Press, Aug. 2017.

[34] John Cardy. *Scaling and renormalization in statistical physics*. Vol. 5. Cambridge university press, 1996.

[35] Jean Zinn-Justin. *Quantum field theory and critical phenomena*. Clarendon Press, 1996.

[36] Zohar Komargodski. "Renormalization Group Flows and Anomalies." *Les Houches Lect.Notes* 97 (2015), pp. 255–271. DOI: 10.1093/acprof:oso/9780198727965.003.0011.

[37] Joseph Polchinski. "Scale and Conformal Invariance in Quantum Field Theory." *Nucl.Phys.* B303 (1988), pp. 226–236. DOI: 10.1016/0550-3213(88)90179-4.

[38] A. B. Zamolodchikov. "Irreversibility of the Flux of the Renormalization Group in a 2D Field Theory." *JETP Lett.* 43 (1986), pp. 730–732.

[39] Yu Nakayama. "Scale Invariance vs Conformal Invariance." *Phys.Rept.* 569 (Mar. 28, 2015), pp. 1–93. DOI: 10.1016/j.physrep.2014.12.003.

[40] Subir Sachdev. *Quantum Phase Transitions*. Cambridge University Press, 2000. DOI: 10.1017/CBO9780511622540.

[41] Debasish Banerjee and Shailesh Chandrasekharan. "Finite size effects in the presence of a chemical potential: A study in the classical nonlinear O(2) sigma-model." *Phys.Rev.* D81 (2010), p. 125007. DOI: 10.1103/PhysRevD.81.125007.

[42] Nikolay Prokof'ev and Boris Svistunov. "Worm Algorithms for Classical Statistical Models." *Phys.Rev.Lett.* 87 (2001), p. 160601. DOI: 10.1103/PhysRevLett.87.160601.

[43] N. Prokof'ev and B. Svistunov. "Worm Algorithm for Problems of Quantum and Classical Statistics" (May 18, 2010). arXiv: 0910.1393 [cond-mat, physics:hep-lat].

[44] James Gubernatis, Naoki Kawashima, and Philipp Werner. *Quantum Monte Carlo Methods: Algorithms for Lattice Models*. Cambridge: Cambridge University Press, 2016. DOI: 10.1017/CBO9780511902581.

[45] Hersh Singh and Shailesh Chandrasekharan. "A Qubit Regularization of the $O(3)$ Sigma Model." *Phys.Rev.* D100 (Sept. 2019), p. 054505. DOI: 10.1103/PhysRevD.100.054505.

[46] Andrea Pelissetto and Ettore Vicari. "Critical Phenomena and Renormalization Group Theory." *Phys.Rept.* 368 (2002), pp. 549–727. DOI: 10.1016/S0370-1573(02)00219-3.

[47] Kenneth G. Wilson and Michael E. Fisher. "Critical Exponents in 3.99 Dimensions." *Physical Review Letters* 28.4 (Jan. 1972), pp. 240–243. DOI: 10.1103/PhysRevLett.28.240.

[48] Piers Coleman. *Introduction to Many-Body Physics*. Cambridge: Cambridge University Press, 2015. DOI: 10.1017/CBO9781139020916.

[49] Moshe Moshe and Jean Zinn-Justin. "Quantum Field Theory in the Large N Limit: A Review." *Phys.Rept.* 385 (2003), pp. 69–228. DOI: 10.1016/S0370-1573(03)00263-1.

[50] S. A. Antonenko and A. I. Sokolov. "Critical Exponents for a Three-Dimensional O(n)-Symmetric Model with N>3." *Physical Review E* 51.3 (Mar. 1995), pp. 1894–1898. DOI: 10.1103/PhysRevE.51.1894.

[51] Martin Hasenbusch and Ettore Vicari. "Anisotropic perturbations in three-dimensional O(N)-symmetric vector models." *Physical Review B* 84.12 (Sept. 2011). arXiv: 1108.0491, p. 125136. DOI: 10.1103/PhysRevB.84.125136.

[52] Filip Kos et al. "Precision Islands in the Ising and $O(N)$ Models." *Journal of High Energy Physics* 2016.8 (Aug. 2016). DOI: 10.1007/JHEP08(2016)036. arXiv: 1603.04436.

[53] Youjin Deng. "Bulk and Surface Phase Transitions in the Three-Dimensional $O(4)$ Spin Model." *Physical Review E* 73.5 (May 2006), p. 056116. DOI: 10.1103/PhysRevE.73.056116.

[54] S. Holtmann and T. Schulze. "Critical Behavior and Scaling Functions of the Three-Dimensional O(6) Model." *Physical Review E* 68.3 (Sept. 2003), p. 036111. DOI: 10.1103/PhysRevE.68.036111.

[55] Agostino Butti and Francesco Parisen Toldin. "The Critical Equation of State of the Three-Dimensional O(N) Universality Class: N>4." en. *Nuclear Physics B* 704.3 (Jan. 2005), pp. 527–551. DOI: 10.1016/j.nuclphysb.2004.10.021.

[56] Paulo F. Bedaque and Ubirajara van Kolck. "Effective field theory for few nucleon systems." *Ann.Rev.Nucl.Part.Sci.* 52 (2002), pp. 339–396. DOI: 10.1146/annurev.nucl.52.050102.090637.

[57] Eric Braaten, Abhishek Mohapatra, and Hong Zhang. "Nonrelativistic Effective Field Theory for Axions." *Phys.Rev.* D94.7 (Oct. 13, 2016), p. 076004. DOI: 10.1103/PhysRevD.94.076004.

[58] Ranjan Laha and Eric Braaten. "Direct detection of dark matter in universal bound states." *Phys.Rev.* D89 (May 2014), p. 103510. DOI: 10.1103/PhysRevD.89.103510.

[59] Eric Braaten and H.-W. Hammer. "Universal Two-body Physics in Dark Matter near an S-wave Resonance." *Phys.Rev.* D88 (Sept. 2013), p. 063511. DOI: 10.1103/PhysRevD.88.063511.

[60] Wilhelm Zwerger. *The BCS-BEC Crossover and the Unitary Fermi Gas*. Springer Science & Business Media, Oct. 22, 2011. 543 pp. Google Books: VjdUd5JbRooC.

[61] Eduardo C. Marino. *Quantum Field Theory Approach to Condensed Matter Physics*. Cambridge University Press, 2017. DOI: 10.1017/9781139696548.

[62] B. L. Altshuler and A. G. Aronov. "Electron–Electron Interaction In Disordered Conductors." en. *Modern Problems in Condensed Matter Sciences*. Ed. by A. L. Efros and M. Pollak. Vol. 10. Electron–Electron Interactions in Disordered Systems. Elsevier, Jan. 1985, pp. 1–153. DOI: 10.1016/B978-0-444-86916-6.50007-7.

[63] A. Bansal et al. "Pion-Less Effective Field Theory for Atomic Nuclei and Lattice Nuclei." *Phys.Rev.* C98.5 (Nov. 1, 2018), p. 054301. DOI: 10.1103/PhysRevC.98.054301.

[64] L. Contessi et al. "Ground-State Properties of ${\hat{4}}$He and ${\hat{16}}$O Extrapolated from Lattice QCD with Pionless EFT." *Phys.Lett.* B772 (Sept. 10, 2017), pp. 839–848. DOI: 10.1016/j.physletb.2017.07.048.

[65] Dean Lee. "Lattice simulations for few- and many-body systems." *Prog. Part. Nucl. Phys.* 63 (2009), pp. 117–154. DOI: 10.1016/j.ppnp.2008.12.001. arXiv: 0804.3501.

[66] Joaquin E. Drut and Amy N. Nicholson. "Lattice methods for strongly interacting many-body systems." *J. Phys.* G40 (2013), p. 043101. DOI: 10.1088/0954-3899/40/4/043101. arXiv: 1208.6556.

[67] J. Carlson et al. "Quantum Monte Carlo methods for nuclear physics." *Rev. Mod. Phys.* 87 (2015), p. 1067. DOI: 10.1103/RevModPhys.87.1067. arXiv: 1412.3081 [nucl-th].

[68] Dean Lee. "Lattice Methods and the Nuclear Few- and Many-Body Problem." *Lect.Notes Phys.* 936 (2017), pp. 237–261. DOI: 10.1007/978-3-319-53336-0˙6.

[69] Amy N. Nicholson. "Lattice Methods and Effective Field Theory." *Lect.Notes Phys.* 936 (2017), pp. 155–235. DOI: 10.1007/978-3-319-53336-0˙5.

[70] Xi-Wen Guan, Murray T. Batchelor, and Chaohong Lee. "Fermi Gases in One Dimension: From Bethe Ansatz to Experiments." *Reviews of Modern Physics* 85.4 (Nov. 27, 2013), pp. 1633–1691. DOI: 10.1103/RevModPhys.85.1633. arXiv: 1301.6446.

[71] U. J. Wiese. "Bosonization and Cluster Updating of Lattice Fermions." *Phys.Lett.* B311 (1993), pp. 235–240. DOI: 10.1016/0370-2693(93)90561-U.

[72] H. G. Evertz. "The Loop Algorithm." *Adv.Phys.* 52 (2003), p. 1. DOI: 10.1080/0001873021000049195.

[73] Hersh Singh. "Worldline approach to few-body physics on the lattice." *36th International Symposium on Lattice Field Theory (Lattice 2018) East Lansing, MI, United States, July 22-28, 2018*. 2018. arXiv: 1812.02364 [hep-lat].

[74] Hersh Singh and Shailesh Chandrasekharan. "Few-Body Physics on a Space-Time Lattice in the Worldline Approach." *Physical Review D* 99.7 (Apr. 2019), p. 074511. DOI: 10.1103/PhysRevD.99.074511. arXiv: 1812.05080.

[75] David H. Adams and Shailesh Chandrasekharan. "Chiral limit of strongly coupled lattice gauge theories." *Nucl. Phys.* B662 (2003), pp. 220–246. DOI: 10.1016/S0550-3213(03)00350-X. arXiv: hep-lat/0303003 [hep-lat].

[76] Shailesh Chandrasekharan and Fu-Jiun Jiang. "Phase-diagram of two-color lattice QCD in the chiral limit." *Phys. Rev.* D74 (2006), p. 014506. DOI: 10.1103/PhysRevD.74.014506. arXiv: hep-lat/0602031.

[77] Urs Wenger. "Efficient simulation of relativistic fermions via vertex models." *Phys. Rev.* D80 (2009), p. 071503. DOI: 10.1103/PhysRevD.80.071503. arXiv: 0812.3565 [hep-lat].

[78] Olav F. Syljuåsen and Anders W. Sandvik. "Quantum Monte Carlo with directed loops." *Phys. Rev. E* 66 (4 Oct. 2002), p. 046701. DOI: 10.1103/PhysRevE.66.046701.

[79] Chen-Ning Yang. "Some Exact Results for the Many Body Problems in One Dimension with Repulsive Delta Function Interaction." *Phys.Rev.Lett.* 19 (1967), pp. 1312–1314. DOI: 10.1103/PhysRevLett.19.1312.

[80] M. Gaudin. "Un systeme a une dimension de fermions en interaction." *Physics Letters A* 24.1 (Jan. 1967), pp. 55–56. DOI: 10.1016/0375-9601(67)90193-4.

[81] Elliott H. Lieb and F. Y. Wu. "Absence of Mott transition in an exact solution of the short-range, one-band model in one dimension." *Phys.Rev.Lett.* 20 (1968), pp. 1445–1448. DOI: 10.1103/PhysRevLett.21.192.2.

[82] Alexander J. Buser et al. "Quantum Simulation of the Qubit-Regularized O(3)-Sigma Model." *arXiv:2006.15746 [hep-lat, physics:quant-ph]* (June 2020). arXiv: 2006.15746 [hep-lat, physics:quant-ph].

[83] S. Chandrasekharan and U. J. Wiese. "Quantum link models: A Discrete approach to gauge theories." *Nucl.Phys.* B492 (1997), pp. 455–474. DOI: 10.1016/S0550-3213(97)00006-0.